Parsec-Scale Nuclear Structure of NGC 3079 based on VLBI Observations

by

Satoko SATOH

Doctor of Science

Department of Astronomical Science

School of Mathematical and Physical Science

The Graduate University for Advanced Studies

1998 (School Year)

Acknowledgments

First of all, I wish to acknowledge to S. Enome and M. Inoue, my supervisors in National Astronomical Observatory, for guidance throughout my doctoral course and valuable comments and suggestions on this work. I express my appreciation to N. Nakai, K. M. Shibata, S. Kameno, V. Migenes and P. J. Diamond for helpful discussions and continuous encouragements. Without their adequate advices, this study would have never been accomplished.

I am also grateful to A. S. Trotter for informing me of his unpublished results on this work. I wish to my express my heartfelt thanks to Y. Taniguchi for reading the manuscript and making a number of helpful suggestions. I really thank J. R. Herrnstein and V. Dhawan for their helps in the VLBA observations as the technical contact persons. I would like to thank Y. Terashima for providing me a lot of knowledge about X-ray observations. I greatly appreciate P. G. Edwards's careful reading the entire text in the paper and correcting my English. I thank all who have given me their assistance and encouragement.

The National Radio Astronomy Observatory is a facility of the National Science Foundation operated under cooperative agreement by Associated Universities, Inc. This research was supported by a Grant-in-Aid for JSPS Fellows by the Ministry of Education, Science, Sports and Culture.

Contents

List of Figures

List of Tables

Chapter 1

Introduction

1.1 H_2O Megamasers

The first extragalactic H_2O maser was discovered by Churchwell et al. (1977) in M33. They made a search for H_2O using the 100-m telescope at Effelsberg towards 16 selected H II regions in M33, and maser emission was detected towards one H II region, IC133. After this discovery, dos Santos and Lèpine (1979) found H_2O maser emission from the active galactic nucleus (AGN) of NGC 4945. The luminosity of the maser from this nucleus is about 100 times more powerful than that of typical H_2O maser sources in the Galaxy. Such emission has been detected from about 20 galaxies so far. These maser emissions appear to be associated exclusively with AGN. These characteristics justified their classification as 'megamasers'.

High resolution images of megamasers allow us to get vital insights about the nuclear regions. A few known megamasers have been imaged with Very Long Baseline Interferometry (VLBI), which has provided glimpses of the parsec-scale region in AGN. Such views are not available with any other methods.

To illustrate what has been found in H_2O megamasers and what are the keys to understand the physical situation of AGN from VLBI observations, we show here a summary on NGC 4258. NGC 4258 is an H_2O megamaser, with peak flux of 3 Jy around the systemic velocity of the galaxy (Claussen et al. 1984; Claussen and Lo 1986). Its nuclear activity is classified to be a Seyfert 1.9 or LINER (Heckman 1980; Stauffer 1982; Filippenko and Sargent 1985; Makishima et al. 1994).

Nakai et al. (1993) detected high-velocity maser emissions offset by ±1000 km s^{-1} in velocity from the motion of the nucleus itself with the 45-m telescope at the Nobeyama Radio Observatory. Their velocities were much higher than the typical velocity of galactic masers and suggested rapid motion near the nucleus. Watson and Wallin (1994) proposed that the maser emissions (i.e., the systemic-velocity maser emission and the high-velocity maser emission) could come from an edge-on Keplerian orbit with radius of ~0.1pc.

After the discovery of the high-velocity masers (Nakai et al. 1993), high resolution observations with the VLBA (Very Long Baseline Array, NRAO) were conducted , and an edge-on, thin Keplerian disk was found (Miyoshi et al. 1995). Both blue- and red-shifted high velocity masers were well explained by a simple rotating system, located at tangential parts of the orbits where emissions are effectively amplified by long gain paths. On the other hand, the systemic masers were explained due to amplification of background continuum radiation which is supposed to exist at the center of the rotating system. Herrnstein et al. (1997) also detected the continuum emission located at the central area of the masering disk although the background continuum structure of the systemic-velocity maser is not clear.

Another important result which confirms the Keplerian disk is the time-variation of velocity shift of the H_2O maser emission obtained from monitoring programs by a single-dish telescope. The observations over several years revealed that the radial velocity of the systemic-velocity features drift systematically, while the high-velocity masers do not show significant velocity variation (Haschick et al. 1994; Greenhill et al. 1995; Nakai et al. 1995). The velocity drift of the systemic-velocity features of the maser emission was interpreted as the centripetal acceleration of a rotating Keplerian edge-on disk, $\dot{v} = v^2/r$. The continuous velocity drift of the systemic-velocity features and the constant velocities of the high-velocity features are consistent with a model of a rotating disk around the nucleus. Taking the velocity drift of the systemic-velocity features as the centripetal acceleration, the Keplerian curve of the maser feature in position-velocity (P-V) diagram indicated a mass of the inner central engine of 3.6×10^7 $M_\odot$. The derived central mass density is at least 4×10^9 $M_\odot$ pc^{-3}.

The information of the orbit velocity and the radius from the VLBI observations, and the centripetal acceleration from the monitoring studies of NGC 4258 offered a new method of direct measurement of galaxy distances using only Newton's law of motion (Nakai 1996). This method was applied to NGC 4258 to determine a distance of 6.57±0.32 Mpc with the accuracy of 5 %.

Thus, the high-velocity maser features, the velocity gradient, and the drifting maser features around the systemic velocity are keys to recognizing the existence of an edge-on Keplerian rotation disk and to determining its rotating plane in other megamasers. Using these keys, interpretations of maser emission of the nucleus have been tried in several other megamasers. However, no clear Keplerian rotation disk has been found yet in other megamasers, as discussed below.

In NGC 1068, a typical Seyfert 2 galaxy, H_2O maser emission is detected over a velocity range from 800 to 1460 km s^{-1}, including the systemic velocity of the galaxy of 1123 km s^{-1} (Claussen et al. 1984; Claussen and Lo 1986). Monitoring has shown that the velocities of the strongest maser features at velocity of 1388–1446 km s^{-1}, redshifted from the systemic velocity of the galaxy, were constant and showed no significant drift. High resolution images of H_2O maser emission with the VLA have revealed that the H_2O maser emission is associated with two continuum components (C and S1) in the nucleus of NGC 1068 (Gallimore et al. 1996), and the P-V diagram obtained from the VLBA observations has been fitted to an edge-on thin disk with an inner radius of 0.65 pc and an outer radius of 1.1 pc. The position angle of the disk rotation axis, $\sim 45°$, differs from that of the radio jet axis seen on scale of 10 pc, by 30–40° (i.e., the disk is not perpendicular to the jet). The enclosed mass is about 1.5×10^7 $M_\odot$, however, the rotation curve falls more gradually than $v \propto r^{-\frac{1}{2}}$, or is "sub-Keplerian".

The same P-V diagram analysis as NGC 4258 and NGC 1068 has been applied to the H_2O maser in NGC 4945, the first discovered H_2O megamaser (dos Santos and Lépine 1979; Batchelor et al. 1982). Greenhill et al. (1997a) observed the maser with the VLBA. Because of its low declination of $-49°$, only the four southernmost antennas of the VLBA could be used. The maser emission is distributed roughly linearly over $\sim$ 0.7 pc at P.A. $\sim$45°. The fitting to an edge-on disk indicates a binding mass of $\sim 1 \times 10^6$ $M_\odot$ within a volume of radius of 0.3 pc, although the P-V structure does not show clear evidence of systematic rotation. Further, no velocity drift of maser features has been found yet in NGC 4945. This galaxy is classified as a type 2 Seyfert or LINER (Moorwood and Glass 1984; Whiteoak and Gardner 1979; Iwasawa et al. 1993).

The velocity drift of maser features has been reported also in two megamasers in addition to NGC 4258: one is NGC 3079 (see next section), and the other is NGC 2639. NGC 2639 has H_2O maser emission close to the systemic velocity of the galaxy (Braatz et al. 1994), and it is similar in character to NGC 4258. Although a VLBA map of maser emission of NGC 2639 has not been shown yet, an increasing velocity drift of the maser emission has been reported (Wilson et al. 1995). This is the second example of maser features with velocity drift around the systemic velocity of the host galaxy. NGC 2639 is generally considered as a LINER (Keel 1984; Filippenko and Sargent 1985; Ho et al. 1993).

NGC 1052, however, has different profile of H_2O maser emission from those found in other active nuclei. The H_2O maser emission of NGC 1052 was discovered by single-dish surveys for megamasers of over 350 AGNs (Braatz et al. 1994, 1996b, 1997). Its emission profile is broad and relatively smooth (i.e., they are not resolved into narrow spectral components). Claussen et al. (1998) show that the masers of NGC 1052 are unlikely to be around a massive nucleus. NGC 1052 has a some nuclear activity and is classified as a LINER.

Thus, some megamasers are indicative the presence of nuclear disks or tori viewed close to edge-on. However, only NGC 4258 has all the factors, namely the high-velocity maser feature, the velocity gradient of Keplerian rotation and velocity drift, which identify an edge-on Keplerian rotation disk in listed table 1.1. The structure of megamaser emission generally does not seem to be as simple as NGC 4258.

Many searches of powerful extragalactic H_2O maser sources have been made and new detections of H_2O maser emission in AGNs have been reported (Braatz et al. 1994, 1996a, 1996b, 1997; Koekemoer et al. 1995; Hagiwara et al. 1997; Greenhill et al. 1997b). The survey of 354 AGNs for H_2O megamaser emission by Braatz et al. (1997) has shown that detection rate of Seyfert 1, Seyfert 2 and LINER is 0/83, 10/163 and 5/69, respectively. The maser-detected galaxies are generally classified to be LINERs or type 2 Seyferts. No H_2O megamaser emission has been found in Seyfert 1 nuclei, while it is found in Seyfert 2's and LINERs with similar detection rates. To explain why no maser emission was detected from Seyfert 1 galaxies, one possible explanation is presented by Braatz et al. (1997). All AGNs can possess molecular gas tori with H_2O maser emission and we can observe the radiation viewed almost edge-on. This is reminiscent of the unification scheme in Seyfert AGN with obscuring tori (e.g. Antonucci 1993; Mushotzky et al. 1993).

The hypothesis has been supported in some megamasers by observations at other frequency bands. Gallimore et al. (1997) observed NGC 1068 with the VLBA and detected continuum structure elongated 1.4 pc with P.A. $\sim 106°$, suggesting an obscuring disk around the nucleus. The disk is viewed nearly edge-on, and is perpendicular to the radio jet. Gallimore et al. (1997) suggested that H_2O maser emission is associated with the inner edge of the torus. Wilson et al. (1998) claim that it is likely that NGC 2639 has an obscuring torus of ionized gas from VLBI continuum observations. X-ray observations revealed that there is a trend for H_2O megamasers to be associated with galaxies exhibiting high X-ray absorbing columns, some of which show column densities of $> 10^{24}$ atoms cm^{-2} (e.g. Braatz et al. 1997; Terashima 1998). These results suggest a nearly edge-on geometry to the disks or tori, as is the case for Seyfert 2 galaxies. Thus, observations of megamasers with high resolution can provide a strong probe of the unified model of Seyfert galaxies.

1.2 An Overview of NGC 3079

1.2.1 Large Scale

NGC 3079 is an edge-on spiral galaxy, and classified SB(s)c (de Vaucouleurs et al. 1991). The major axis of the galaxy has a position angle of 164°, and the disk is inclined 83° from the plane of the sky (Roberts 1968). The redshift of the galaxy, obtained from spectroscopic observations at Lick, corresponds to a velocity of 1171 km s^{-1} in the optical definition: $v = (\Delta\lambda/\lambda_0)c$ (Humason et al. 1956), which gives a Hubble distance ($H_0 = 75$ km s^{-1} Mpc^{-1}) of 15.6 Mpc. However, observations of H I emission along the galactic plane over 50 kpc estimate the

Table 1.1: H_2O masers structure of megamasers

Source	Type	Velocity trend ?	Keplerian rotation ?	Perpendicular to jet?	Velocity drift ?
NGC 4258	S1.9, L	Y	Y	Y	Y
NGC 1068	S2	Y	Y	N	N
NGC 4945	S2, L	Y	N		N
NGC 2639	L				Y
NGC 1052	L	Y	N	N	

S=Seyfert; L=LINER

systemic velocity of the galaxy (V_{sys}) to be 1116.7±0.5 km s^{-1} (Irwin and Seaquist 1991). CO observations reveal a rotating molecular disk of a few kiloparsec-scale with a systemic velocity of 1150±10 km s^{-1} (Irwin and Sofue 1992).

Radio continuum images display a unique and complex morphology: Aperture synthesis measurements by de Bruyn (1977) have shown a cross-like emission elongated more than 2 kpc along the minor axis of the galaxy at 1.4 and 5 GHz. Images at 2 and 8 GHz were described by Seaquist et al. (1978). Hummel et al. (1983) have shown an anomalous component of the radio continuum emission. The component is elongated along a line crossing the nucleus, at the position angle of 65°. A detailed study of this radio feature was made by Duric et al. (1983), who observed it with the VLA at 1.4 and 5 GHz. The extensions of emission along the minor axis were resolved at 5 GHz into lobes and curving bridges. In particular, they identified a highly polarized, ring-shaped lobe extending ~15 arcsec east of the central source. There is no stellar counterpart to the radio emission. A narrowband Hα+[N II] image revealed an apparent "loop" structure corresponding to the radio lobes along the minor axis (Ford et al. 1986).

Furthermore, Duric and Seaquist (1988) modeled the minor axis structures as the consequences of a wind from the nucleus, focused into a bipolar outflow by a dense circumnuclear medium. Spectroscopic studies by Heckman et al. (1990) support a "galactic superwind" model for NGC 3079. Their Hα and [N II] lines display velocities with a range of 1600 km s^{-1}, which is regarded as being due to a strong outflow. Velleux et al. (1994) detected extremely violent gas motions ranging over 2000 km s^{-1}. Filippenko and Sargent (1992) concluded that activity of the nuclear region powers thesuperwind. Near infrared and optical studies support the model, a superwind is produced not by starbursts, but by an active nucleus (Hawarden et al. 1995).

In NGC 3079, CO emission is concentrated in the center. CO maps reveal a bright molecular disk centered on the nucleus and extending along the major axis of the galaxy with P.A. ~165° (Young et al. 1988; Irwin and Sofue 1992; Sofue and Irwin 1992; Tacconi et al. 1996; Braine et al. 1997). Irwin and Sofue (1992) detected a tilted component of CO gas that is extended along the direction of P.A.$= -55°$.

X-ray emission was detected by the Einstein observatory with a luminosity of 2.1×10^{40} erg s^{-1} in the 0.5–3 KeV range (Fabbiano et al. 1982, 1992). *ROSAT* PSPC (the Position Sensitive Proportional Counter) images revealed extended diffuse emission along the minor axis, in the same direction as the Hα feature, the radio jet, and radio lobes (Read et al. 1997). The X-ray source was resolved into three components; emissions from the super-bubble, the disk of the galaxy, and the halo, from a *ROSAT* HRI (High-Resolution Imager) observation (Pietsch et al. 1998). Fitting of the *ROSAT* PSPC and *ASCA* intensities indicated that at least two emission components comprise the X-ray spectrum (Dahlem et al. 1998).

1.2.2 Small Scale

NGC 3079 has also very luminous H_2O maser emission from its nucleus. It is the second most luminous known H_2O megamaser source, with an isotropic luminosity of $\sim 520\ L_\odot$ (Henkel et al. 1984, Haschick and Baan 1985). The main features of the emission cover the velocity range of 930–1070 km s^{-1} in $V_{\rm LSR}$, blue-shifted from the systemic velocity of the galaxy (Henkel et al. 1984, Haschick and Baan 1985). There is some time-variability of flux density, for example, the flux density of the strongest maser feature has varied around 5 Jy (Henkel et al. 1984, Haschick and Baan 1985). However, maser emission has persisted at roughly the same velocity, i.e., no clear velocity drift is found (Nakai et al.1995, Baan and Haschick 1996). Recently, two faint maser features with velocities at 1190 km s^{-1} (Nakai et al. 1995) and at 1123 km s^{-1} (Trotter et al. 1998; hereafter T98) were detected. The maser feature at 1190 km s^{-1} shows an increasing velocity drift of 3.7±0.6 km s^{-1} yr^{-1} (Nakai, private communication).

H_2O maser emission has been observed with the VLA and with VLBI (Haschick et al. 1990; Greenhill 1992; T98). H_2O maser emission arises in compact clumps with a scale of 0.01 pc. It had been suggested that the maser emission is amplified the background continuum emission. T98 have imaged the H_2O maser emission and showed that the distribution of the clumps is extended over ~2 pc along an axis (P.A.~ −10°) which is approximately aligned with the major axis of the galactic disk. The drifting feature at 1190 km s^{-1} exists ~1 pc south from main maser clumps. Although the systematic velocity trend could not be seen clearly, fitting an edge-on rotating disk along the galactic disk gave a binding mass of $\sim10^6$ $M_\odot$ (T98).

Radio continuum observations at 5 GHz in the parsec-scale region of NGC 3079 were made with the US-VLBI Network in 1986 by Irwin and Seaquist (1988; hereafter IS88). IS88 found that NGC 3079 has three aligned continuum components: two stronger components (A and B) with separation of 1.5 pc and one fainter component (C) between them. IS88 suggested that the jet generated the anomalous radio lobes of kiloparsec scale. However, the direction of the nuclear jet has P.A. ~ 123°, which shows a misalignment of ~60° with the direction of the kiloparsec-scale radio lobes. Continuum observations at 5, 8, and 22 GHz with VLBI were performed by T98 (5 and 8 GHz in 1992, 22 GHz in 1995). T98 detected both continuum component A and B at all measured frequencies. Two 5-GHz maps of IS88 and T98 reveal the relative motion of 200μas yr^{-1} (0.06c) between A and B. Although T98 did not detect the component C, they reported a detection of a new continuum component (labeled D), located ~ 4 pc southeast of B. However, the component D was not found at any other frequencies (T98). In their image at 8 GHz, component A clearly shows substructure. T98 imaged the 22 GHz continuum components using phase-referencing to the brightest maser feature. The continuum emission at 22 GHz was dominated by a compact source which has no positional coincidence with the maser features. The faint component C was marginally detected in the 22 GHz image. T98 analyzed the structure in the parsec-scale region of NGC 3079 and concluded that the both components A and B are radio lobes and the central engine should be located their midpoint, at the intersection of the two axis, the direction of the maser alignment and the jet direction.

H I and OH absorption was also detected in the nuclear region of the galaxy (Haschick and Baan 1985, Irwin and Seaquist 1991). Interferometric observations have shown that H I absorption towards the nucleus has a few velocity components around V_{sys}, suggesting an outflow or a rapid rotation in the nuclear region (Gallimore et al. 1994, Pedlar et al. 1996). Baan and Irwin (1995) showed similar doubly peaked H I and OH absorption profiles with the VLA. Interferometric experiments reveal that the velocity structure of H I absorption in the few-hundred-parsec-scale region is dominated by the galactic rotation (Irwin and Seaquist 1991; Pedlar et al. 1996). A VLBI study of H I absorption reveals that a velocity gradient which seems opposite to the galactic rotation was found in the parsec-scale region of NGC 3079 (Satoh et al. 1998).

Thus, many observations of the nucleus in NGC 3079 have been made. However, little is known about the general view of the parsec-scale structure or the relation among the continuum components, H_2O maser emission and H I and OH absorption.

In this thesis, high resolution and multi-frequency monitoring program of NGC 3079 are reported. The outline of the thesis is as follows: Chapter 2 summarizes the observational strategy and reduction of this research, followed by the results of the multi-frequency continuum observations in Chapter 3. We present images and spectra of continuum structure of the nucleus here. Chapter 4 describes a monitoring program of H_2O maser and continuum emission at 22 GHz. The spectral profile and distribution for each epoch and the relation between H_2O maser and continuum components is shown. In Chapter 5, we report detections of H I and OH absorption and images of H I absorption. Chapter 6 discusses the structure of kinematics of the nuclear region to explain all results of the experiments. Conclusions are presented in the final chapter.

Chapter 2

Observations with Very Long Baseline Interferometry

2.1 Strategy of the Observations

The aims of the experiment are to observe (1) the simultaneous multi-frequency continuum emission to provide the continuum spectra in the nuclear region, (2) time-variabilities of nuclear structure and H_2O maser emission though the monitoring program and (3) the sensitive H I and OH absorption features to detect motions of gas close to the nucleus, in the parsec-scale nuclear region of NGC 3079. The observation frequencies are 1.4, 1.6, 8.4, 15 and 22 GHz. From all frequencies, we observed continuum emission. In addition, observations at 1.4, 1.6 and 22 GHz provided us absorption features of neutral hydrogen 21-cm line, absorption features of hydroxyl 18-cm line and H_2O maser emission associated with the 1.3-cm $6_{16} - 5_{23}$ transition, respectively. The VLBA allows us to investigate the region with parsec resolution, and to switch frequency quickly. In order to detect weak H_2O maser emission with a correlated flux density of about 5 Jy (Haschick et al.1990), and to detect the faint continuum component, we used the ten antennas of the VLBA and three large telescopes as mentioned in the next section.

2.2 A Global VLBI Network

The observations of this research were made using a global VLBI network. Thirteen stations in total were used; the Very Long Baseline Array (VLBA), the Very Large Array (VLA), the

Green Bank (GB) 43-m telescope and the Effelsberg (EB) 100-m telescope. The VLBA consists of ten antennas. The most eastern antenna is located on St. Croix in the US Virgin Islands and most western is on Mauna Kea in Hawaii, resulting in a longest baseline of about 8000 km (e.g., Kellermann and Thompson 1985, Napier et al. 1994). The VLA is a 27-element array having a Y-shaped configuration and is located in New Mexico (e.g. Napier, Thompson and Ekers 1983). In this experiment, the VLA was used as a phased array, i.e., the data were recorded after summing the sampled and delayed IF signals from the working VLA antennas. GB is located at West Virginia in the USA. VLBA, VLA and GB are operated by the National Radio Astronomy Observatory (NRAO) in US. GB has been also used as an element of the US VLBI Network during the 1970s and 1980s. EB is the largest steerable radio telescope in the world, and is operated by the Max-Planck-Institut für Radioastronomie (MPIfR). The telescope is located near Bonn, Germany. It can be also used as a VLBI station and a member of the European VLBI Network. GB and EB have VLBA format recording terminals. The telescopes used for this research are listed in table 2.1.

2.3 Observation and Data Processing

We conducted four VLBI observations of the nucleus of NGC 3079, over 18 months. At the first epoch, we observed at 1.4, 8.4, 15 and 22 GHz on October 20, 1996. The total observational time was 12 hours, and the data of all frequencies were taken using frequency switching. The integrated on-source time is about 3, 2, 1.4 and 5 hours at 1.4, 8.4, 15 and 22 GHz, respectively. All of VLBA antennas, the VLA and EB were used at all frequencies, except at 1.4 GHz in the first epoch the antennas at St. Croix (SC) and Mauna Kea (MK) were not used because of the low sensitivity of visibilities in SC and also MK. The second and third epoch observations were carried out on March 7 and October 2, 1997, respectively. We obtained the images of both H_2O maser and continuum emission and spectrum profile of H_2O maser from the two epochs. At the second epoch, observations were made with all 10 antennas in the VLBA, the phased VLA, GB and EB. At the third epoch, however, GB did not join the observation, but the other 12 antennas were available. The on-source time was 4 and 5 hours for the second and third epochs.

In the fourth epoch, we made observations of H I and OH absorptions on April 9, 1988 over 12 hours. To observe both H I and OH simultaneously, we divided four IFs to two groups of all antennas except GB; one group was for H I and the other was for OH. GB was used only for H I observation. The *u*-*v* coverages of each observation are given in figure 2.4. For all experiments, the continuum sources 4C39.25 and 0917+624 were observed to remove the residual delays and fringe rates. 3C345 was observed as a bandpass calibrator. The data of the thirteen antennas were recorded with left circular polarization using VLBA format with 2-bit sampling except for the data of the first epoch which were 1-bit sampled. The recorded data were processed on the VLBA correlator in Socorro, New Mexico. The spectral resolution is 256 points for each of four 8-MHz IF. The integration time of correlation is 3 seconds.

2.4 Data Reduction

After the correlation, the data proccesing, including calibration and imaging, were done using the NRAO Astronomical Image Processing System (AIPS). Data reduction followed standard continuum VLBI imaging techniques (e.g. Zensus, Diamond and Napier 1995). The residual delays and fringe rates were estimated from observations of the continuum sources 4C39.25 and 0917+624. The bandpass responses were calibrated with observations of 3C345. Standard a priori gain calibration was performed using the measured gains and system temperatures of each antenna.

Continuum observations were averaged into each single frequency band after residual delay, rate, phase and amplitude corrections. At 1.4 and 22 GHz, however, averaging was made over those channels containing no spectral line absorption or emission. The hybrid imaging process, which involved iterative imaging with CLEAN and self-calibration, was done at all frequency bands except that at 22 GHz. At 22 GHz, the solutions of fringe rate calibration and self-calibration obtained from the strongest maser feature at 956 km s^{-1} were applied to the continuum observation. This method is known as the "phase-referencing technique", and makes it possible to determine the relative positions of the continuum emission and the strongest maser feature. The phase-referencing technique was also applied to all spectral channels of 22 GHz using the same strongest maser feature to determine the distribution of all H_2O masers referred to the strongest maser. For the absorption observations, self-calibration was done using the averaged line-free continuum channels after correcting for the residual delays and rates. We applied the result of self-calibration to the spectral line channels. The spectral data were then analyzed by tapering the visibility (we obtained useful data from the baselines between VLA and FD, GB, KP, LA, OV, PT) for 1.4 GHz, and by averaging in frequency. All channel maps and line-free continuum image were CLEANed with a restoring beam of 15×11 mas^2. After that, continuum-subtracted maps were made by intensity-subtracting each channel images from the line-free continuum image. The continuum-subtracted images formed a cube with eight velocity channels. All CLEAN maps were made using NATURAL weighting. The beam sizes and the image rms noise (σ) for each epoch are listed in table 2.2. The distance to NGC 3079 is 15.6 Mpc, hence 1 mas corresponds to 0.076 pc in the galaxy.

Figure 2.1: The u-v coverage of the each observations.

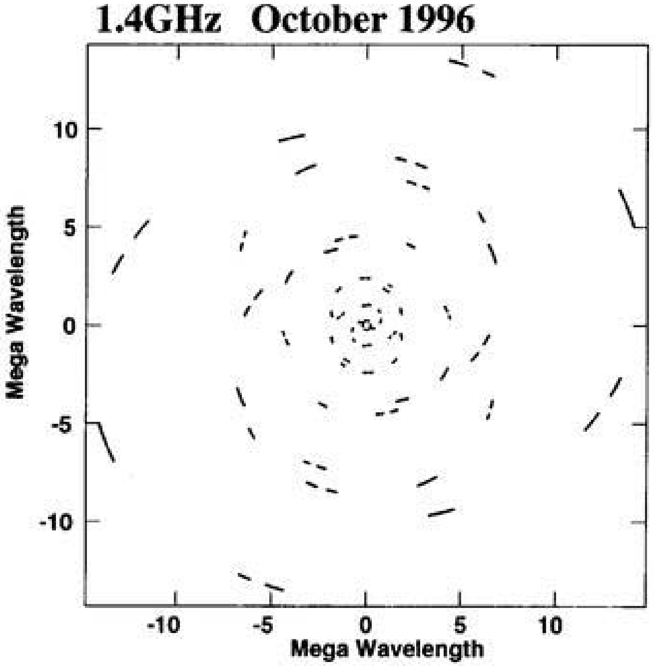
1.4GHz October 1996

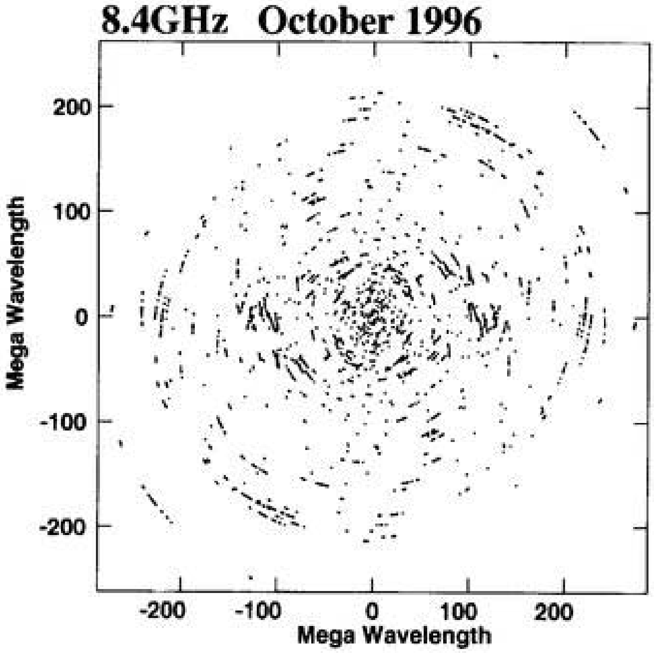
8.4GHz October 1996

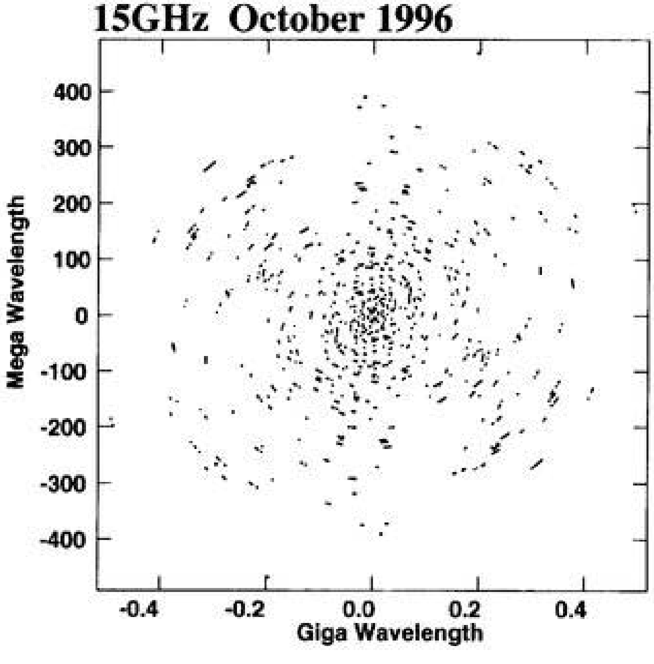
15GHz October 1996

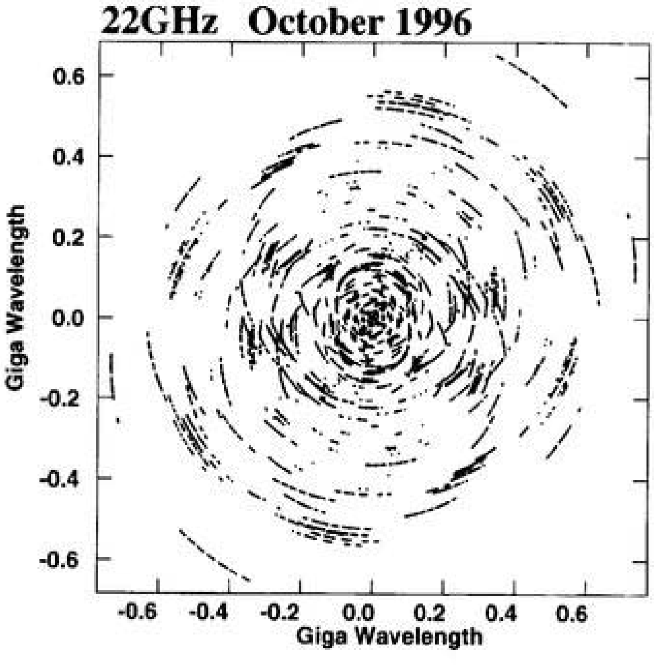
22GHz October 1996

22GHz   March 1997

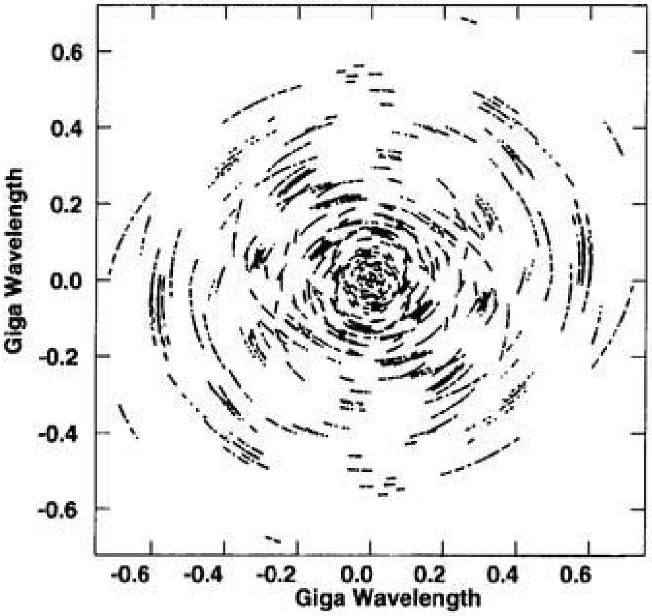

22GHz   October 1997

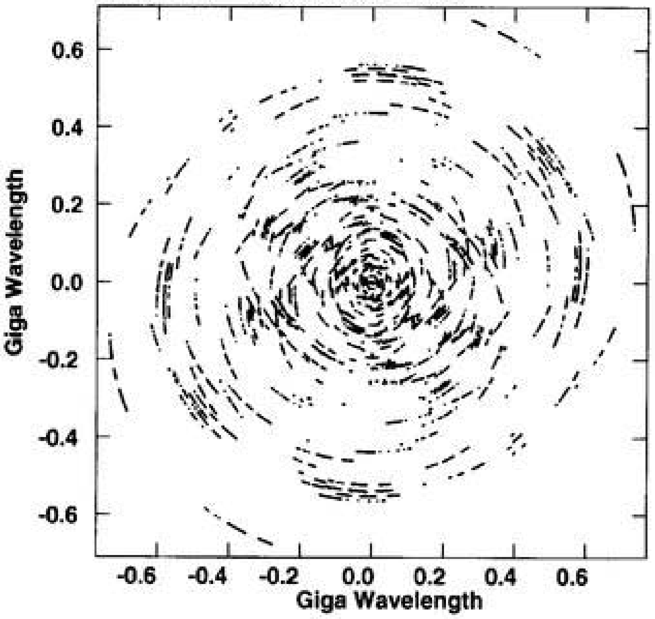

1.4GHz   April 1998

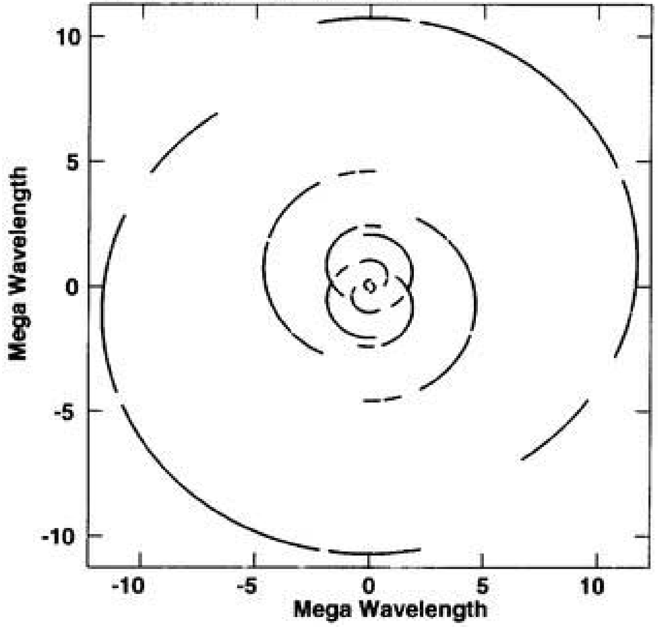

Table 2.1: Telescopes for these experiments

Observatory	Location	Code	Antenna Diameter [m]
NRAO VLBA	St. Croix VI, USA	SC	25
	Hancock NH, USA	HN	25
	N.Liberty IA, USA	NL	25
	Fort Davis TX, USA	FD	25
	Los Alamos NM, USA	LA	25
	Pie Town NM, USA	PT	25
	Kitt Peak AZ, USA	KP	25
	Owens Valley CA, USA	OV	25
	Brewster WA, USA	BR	25
	Mauna Kea HI, USA	MK	25
NRAO VLA	Socorro NM, USA	Y	25 m ×27
NRAO	Green Bank WV, USA	GB	43
MPIfR	Effelsberg, Germany	EB	100

Table 2.2: Beam dimension and rms noise of Global VLBA images

Frequency [GHz]	Major [mas]	Minor [mas]	P.A [°]	Rms noise [mJy beam^{-1}]	Antennas
			1996 October 20		
1.4	14.7	12.8	8	0.43	BR, FD, NL, KP, LA, PT, Y
8.4	1.3	0.91	173	0.23	All of VLBA, Y
15	0.66	0.57	178	0.30	All of VLBA, Y
22*	0.41	0.30	162	0.54	All of VLBA, Y, EB
22†	0.41	0.30	162	6.63	All of VLBA, Y, EB
			1997 March 7		
22*	0.56	0.49	-4	0.24	All of VLBA, Y, GB, EB
22†	0.56	0.49	-4	5.80	All of VLBA, Y, GB, EB
			1997 October 2		
22*	0.41	0.30	162	0.49	All of VLBA, Y, EB
22†	0.41	0.30	162	7.87	All of VLBA, Y, EB
			1998 April 9		
1.4 &	14.9	10.6	-28	0.69	FD, KP, LA, OV, PT, Y, GB

$*$ Continuum

† Spectral line

Chapter 3

Continuum Structure

3.1 Images

The continuum images are described in this chapter. The radio continuum images of the nuclear region for each frequency are shown in figures 3.2(a)–(d). The origin of each image is the phase-center for that frequency, therefore the origins are not coincident with each other. These images were obtained from the first epoch observation. The rms noise (1σ) for each image is 0.43, 0.22, 0.30 and 0.54 mJy beam^{-1}, at 1.4, 8.4, 15 and 22 GHz, respectively. VLBA observations reveal several continuum components at 1.4 and 8.4 GHz, while only a single Gaussian component with deconvolved size of less than 0.45 mas is detected at 15 and 22 GHz. Although we applied a Gaussian taper to the (u, v) plane visibilities at 15 and 22 GHz to get a wider synthesized beam size of 3×3 mas^2, neither image showed clear evidence for other components. At 8.4 GHz, our continuum image revealed three areas of emission: one compact core with extended components (< 1.1 mas) in the northwest, another compact component with an extended structure with a hot spot in the southeast, and a weaker extended structure with substructure between the two main components. Because we identify the same components as the previous observation (IS88), we use hereafter the same nomenclature for these components as used in IS88; component A being the southeast one, B the northwest, and C the fainter one between A and B. Component C shows three peaks within its extended structure, the western-most peak being the strongest.

Relative to component B, the separations of A and C are 25.7±0.2 and 15.6±0.8 mas, respectively. The spatial separation between A and B is 2.8 mas greater than that determined by T98 at 8.4 GHz twenty two months earlier, which results in a subluminal motion with a apparent velocity of 0.16±0.02c (figure 3.2). At 1.4 GHz, on the other hand, only two components are seen because the resolution is too low to resolve components A and C.

We did not detect component D seen by T98 at any frequency. The parameters of the individual components are shown in Table 3.1. These were obtained from elliptical Gaussian model fitting. Components A and C at 8.4 GHz have extended structure with substructure, and the brightest peaks were fitted with Gaussian models.

The first epoch image at 22 GHz shows only one Gaussian component 6.7 mas west from the strongest maser feature, a phase reference (figure 3.2), and no other component is visible above 1.5 mJy beam^{-1} (3σ) level. At the second and third epochs, we obtained higher sensitivities of σ = 0.24 and 0.49 mJy^{-1} and detected two separated components along the southeast-northwest axis. One is the component B we detected at the first epoch. The component A is faint and located 16 mas south from the phase reference feature. Figure 3.2 shows the images of the second and third epochs. Component C was not visible at the 3σ level for each image.

A significant movement is seen at 22 GHz, from 1995 (T98) to 1997 (our works) as shown at 8.4 GHz. At the second epoch, the spatial separation between A and B is 25.99±0.02 mas, with an apparent velocity of 0.21±0.03c from January in 1995 to March in 1997. Between the second and third epochs, the separation becomes 0.3 mas greater in 7 months and the resulting apparent velocity is 0.14±0.02c. The variation of structure is also detected for these three observations at 22 GHz. The component B at the first epoch has an unresolved structure and it agree well with the image in 1995 by T98. The maps of the second and third epoch, however, show the strong compact component with extended structure to east. Component A was getting fainter.

Continuum B is unresolved ($<$ 0.7 mas=0.05 pc), while A and C are extended and have substructures. The flux density of B is in the range of 10–12 mJy at 22 GHz, so the brightness temperature is estimated to be $>10^8$K. The high brightness temperature of B is likely to have a non-thermal origin.

3.2 Spectra

Figure 3.2 shows simultaneous continuum spectra for the component B and the combined component A+C at all frequencies between 1.4 and 22 GHz as determined from the first epoch observation. The flux densities of the components at 8.4, 15 and 22 GHz were derived by convolution with a beam size of 14.7×12.8 mas^2 as used at 1.4 GHz. As seen in figure 3.2, the single component detected at 15 GHz is easily identified as component B. The combined spectrum of components A and C is steep ($\alpha = -0.36 \pm 0.35$; $S \propto \nu^{\alpha}$) between 1.4 and 8.4 GHz. For the second and third epochs, the flux density of A is estimated to be 3.3±0.4 and 4.2±0.9 mJy, respectively. These values are consistent with the steep spectrum of A for first epoch. For component B, on the other hand, we find a positive spectral index of $\alpha = +0.85 \pm 0.18$ between frequencies at 1.4 and 8.4 GHz, and $\alpha = -0.83 \pm 0.21$ and -1.8 ± 0.2 between 8.4 and 15 GHz, and between 15 and 22 GHz, respectively.

The shape of the spectrum of A is different from the spectra, determined in T98, which showed convex spectra with a peak frequency between 8.4 and 22 GHz and is quite similar to that of B.

Table 3.1: Parameters of continuum components for three epochs

ν [GHz] (1)	Component (2)	S_ν [mJy] (3)	Major [mas] (4)	Minor [mas] (5)	P.A [°] (6)	R [mas] (7)	θ [°] (8)
1996 October 20							
1.4 …	B	5.7±1.7	25.8±5.7	14.1±3.8	3±21	…	…
	A+C	5.9±1.7	20.6±4.2	20.0±4.1	46±90	25.6±5.3	134±12
8.4 …	B	6.7±0.5	1.19±0.05	1.03±0.04	17±11	…	…
		7.0±0.9	2.80±0.29	1.22±0.13	132±5	0.4±0.1	223±3
		2.3±0.5	1.54±0.23	1.02±0.15	160±14	1.3±0.1	55±4
	A*	1.9±0.6	1.4±0.3	1.3±0.3	33±80	25.5±0.2	127±1
	C*	2.1±0.9	2.6±0.9	1.3±0.5	159±18	15.6±0.8	125±3
15 …	B	24.4±0.6	0.71±0.01	0.63±0.01	105±5	…	…
22 …	B	12.1±0.7	0.47±0.01	0.33±0.01	93±3	…	…
1997 March 7							
22 …	B	8.5±0.5	0.73±0.03	0.52±0.02	31±4	…	…
		4.4±0.7	0.98±0.11	0.61±0.07	170±9	0.73±0.02	110.5±3.7
	A	3.3±0.4	1.16±0.15	0.33±0.04	156±3	25.99±0.02	127.3±0.1
1997 October 2							
22 …	B	9.5±0.7	0.79±0.04	0.36±0.02	61±2	…	…
		6.2±1.0	0.89±0.10	0.53±0.06	137±9	0.38±0.05	180.0±6.1
	A	4.2±0.9	1.14±0.16	0.33±0.04	156±4	26.33±0.05	126.6±0.1

Col.(1) observed frequency; Col.(2) name of continuum component; Col.(3) flux density of each component; Cols.(4)–(6) parameters of Gaussian model: major and minor axes of each component (FWHM) and the position angle of the major axis, respectively; Col.(7) spatial separation of each component from component B; Col.(8) position angle of each component with respect to component B.

$*$ Brightest peak

Figure 3.1: The continuum images at 1.4, 8.4, 15 and 22 GHz of the nucleus of NGC 3079 made from the data taken on October 20 in 1996. The labels A, B and C are the same nomenclature as the 5 GHz VLBI map of IS88. The HPBW of the synthesized beams are shown at lower right. (a) CLEAN image at 1.4 GHz. The contour levels are (-3, 3, 4, 5, 6, 7)×0.43 mJy beam^{-1}. (b) CLEAN image at 8.4 GHz. The contour levels are (-3, 3, 4, 5, 6, 8, 12, 17, 22, 27, 32, 37)×0.22 mJy beam^{-1}. (c) CLEAN image at 15 GHz. The contour levels are (-3, 3, 13, 23, 33, 43, 53, 63)×0.30 mJy beam^{-1}. (d) CLEAN image at 22 GHz. The contour levels are (-5, 5, 10, 15, 20, 25, 30, 35)×0.54 mJy beam^{-1}.

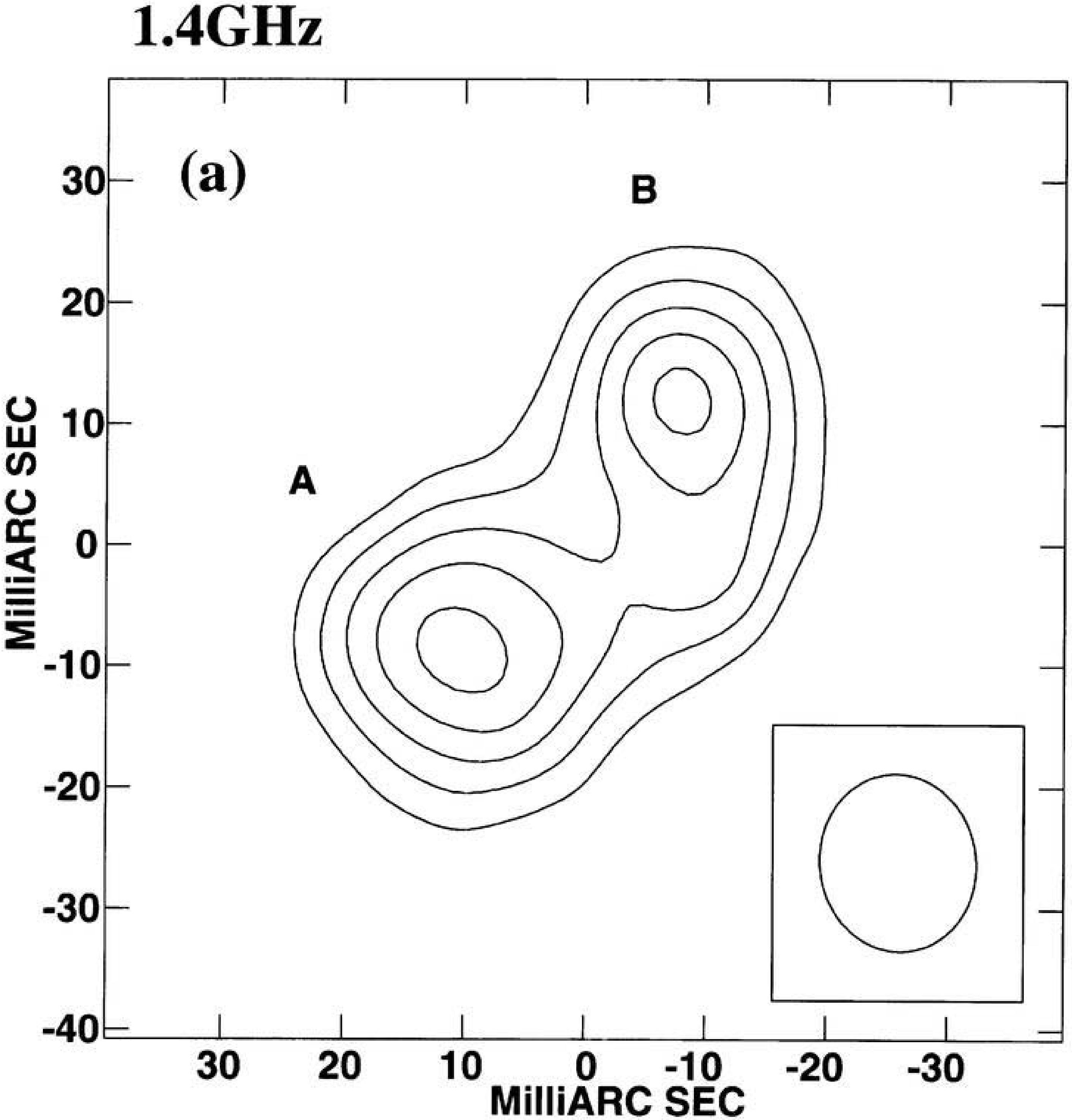
1.4GHz
(a)
B
A
MilliARC SEC
30
20
10
0
-10
-20
-30
-40
30
20
10
0
-10
-20
-30
MilliARC SEC

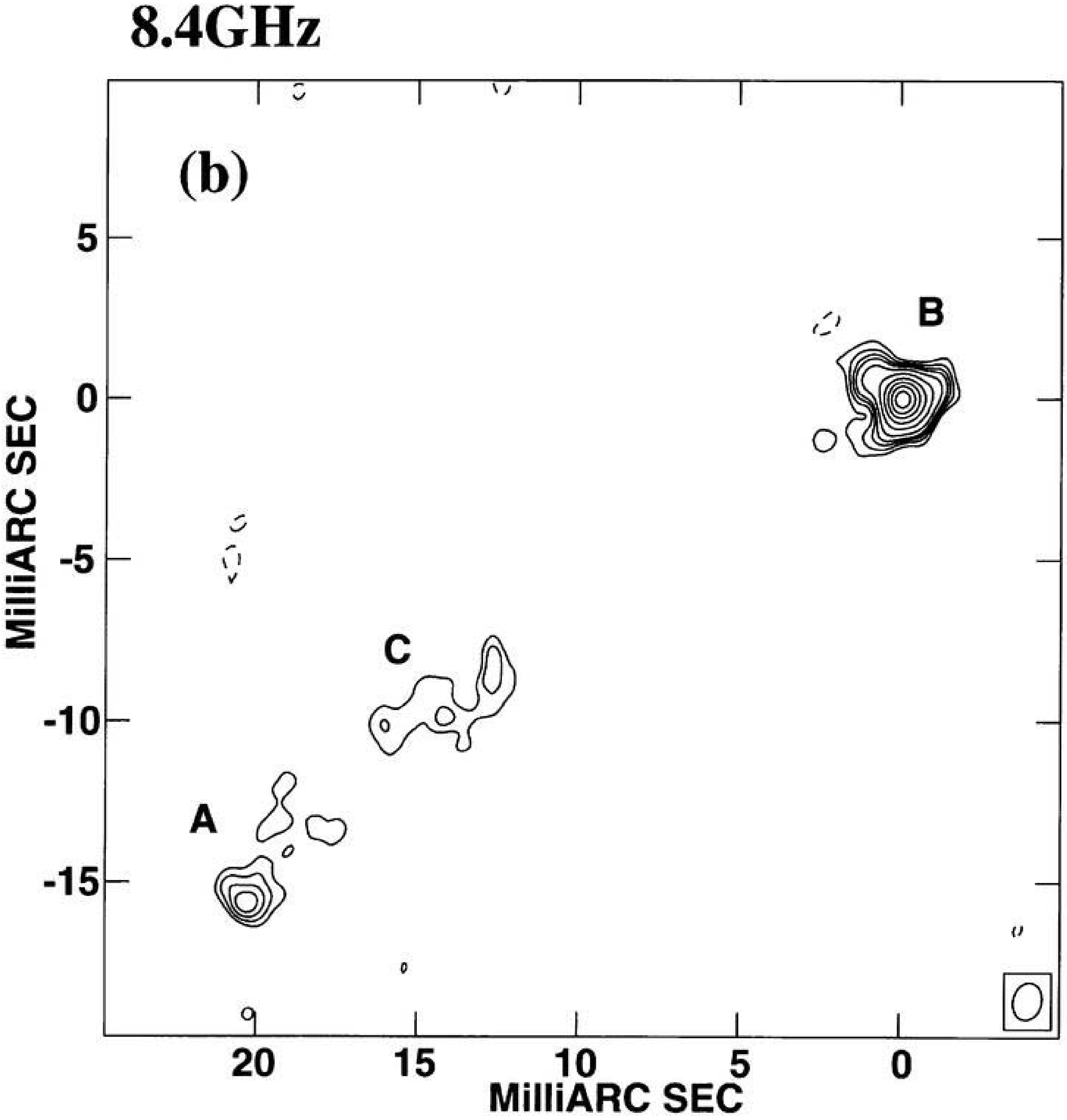
8.4GHz
(b)
B
C
A
MilliARC SEC
5
0
-5
-10
-15
20
15
10
5
0
MilliARC SEC

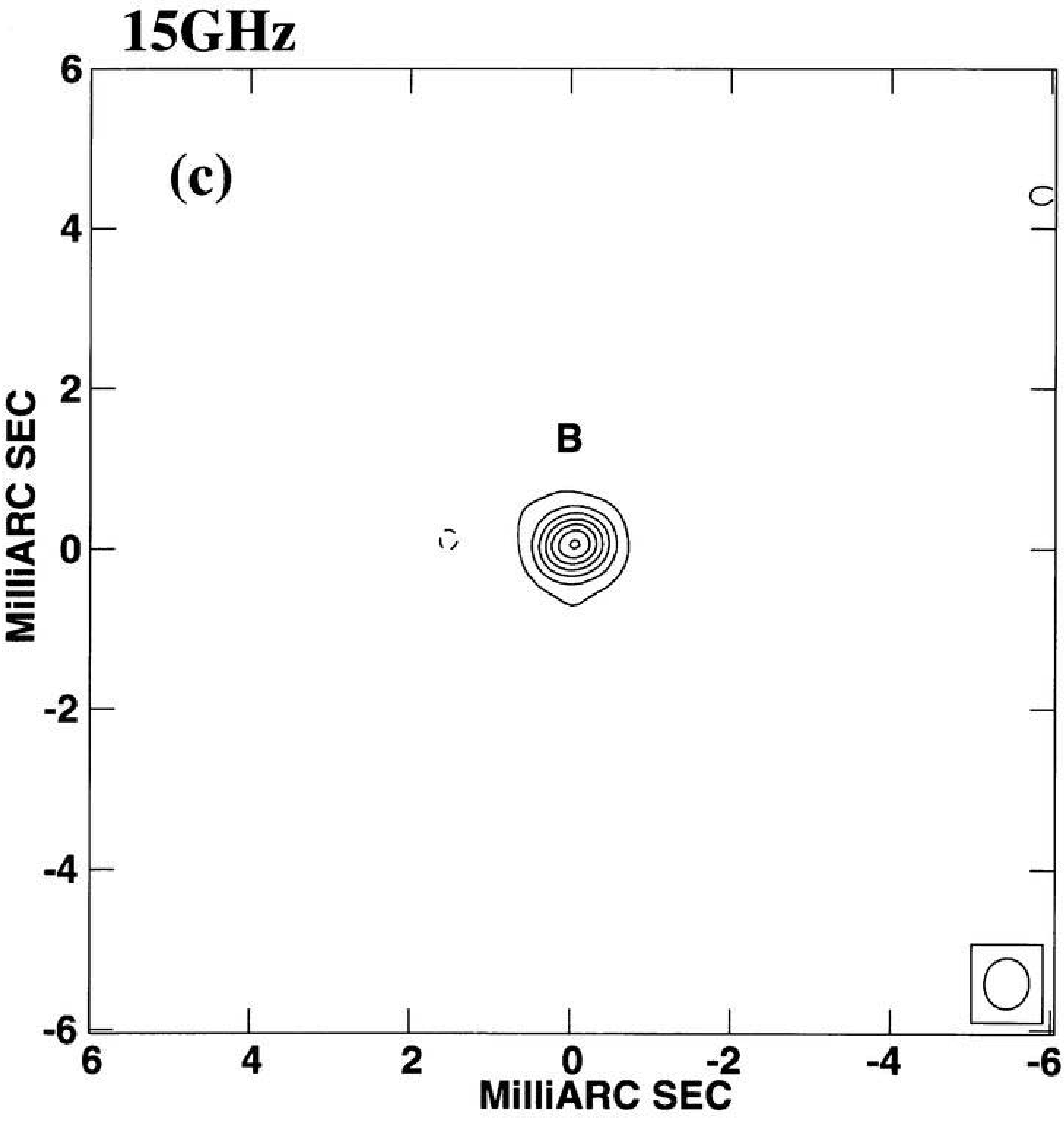
15GHz
(c)
B
6
4
2
0
-2
-4
-6
MilliARC SEC
6
4
2
0
-2
-4
-6
MilliARC SEC

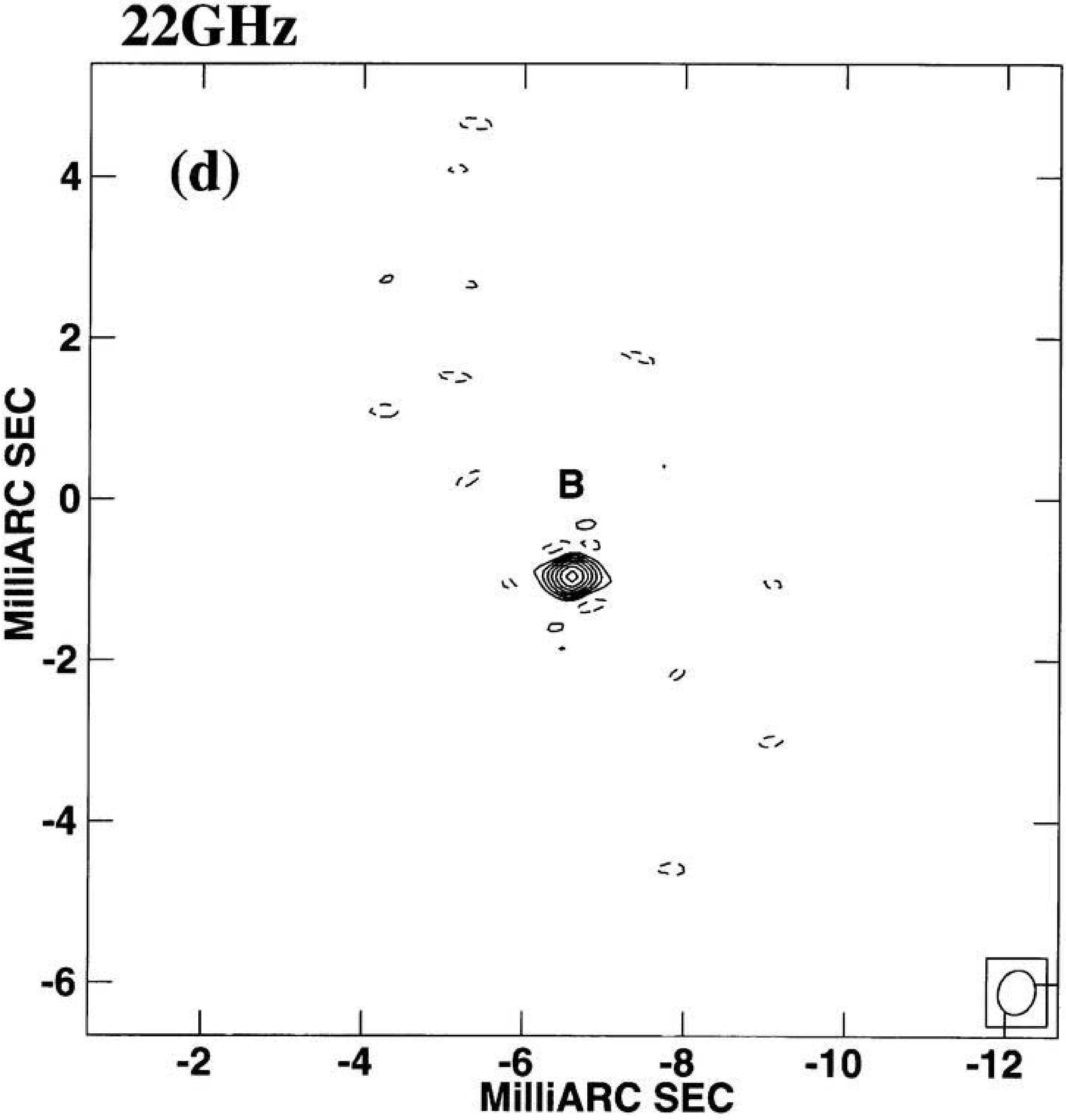
22GHz
(d)
B
MilliARC SEC
MilliARC SEC
4
2
0
-2
-4
-6
-2
-4
-6
-8
-10
-12

Figure 3.2: Spatial separation between continuum components A and B at 8.4 and 22 GHz. The full and open circles indicate the results measured at 8.4 and 22 GHz, respectively. Error bars represent $\pm 1\sigma$ for a Gaussian fitting.

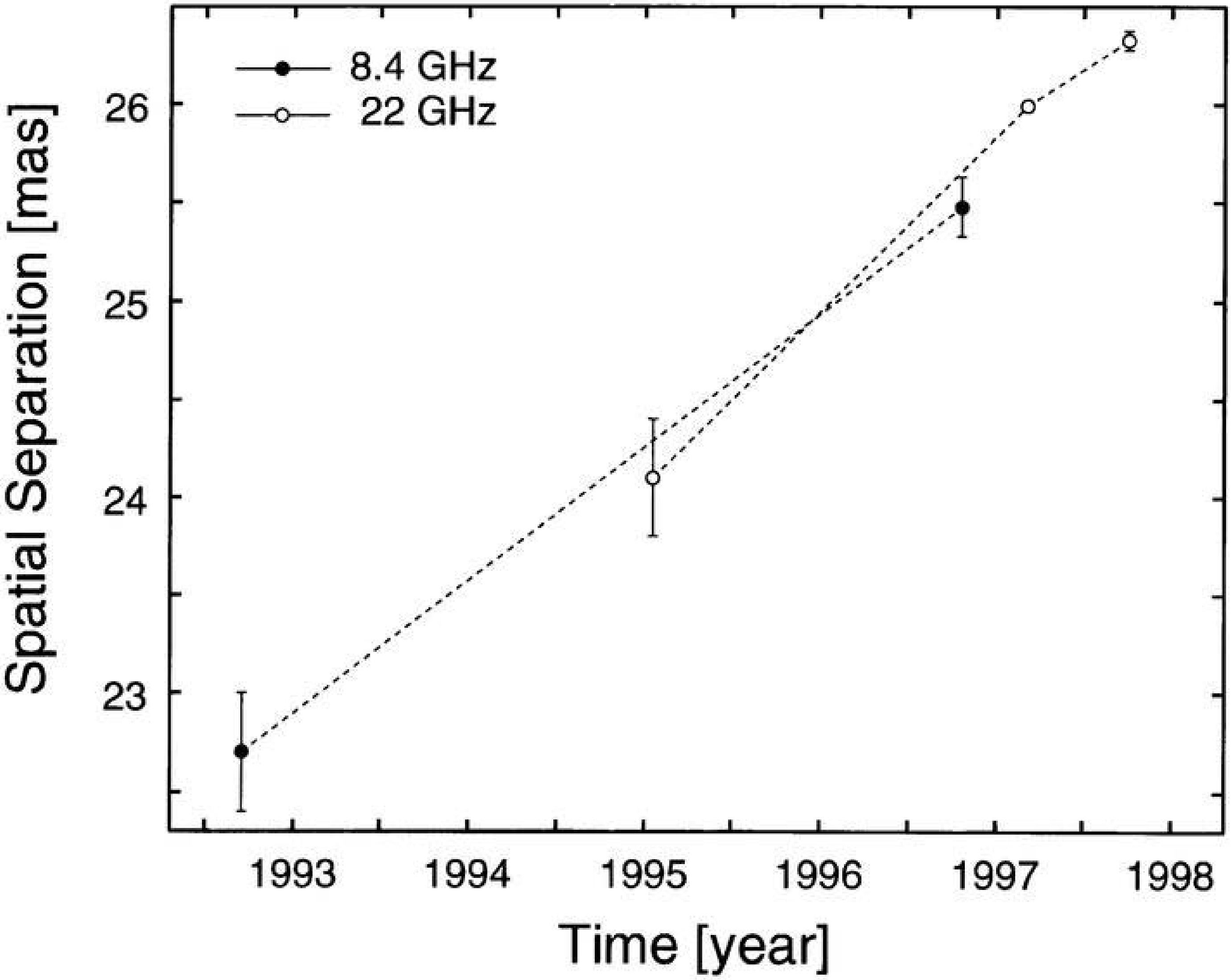
8.4 GHz
22 GHz
Spatial Separation [mas]
23
24
25
26
1993
1994
1995
1996
1997
1998
Time [year]

Figure 3.3: Cleaned, natural weighted 22 GHz continuum maps at the second and third epochs. These were obtained by the phase-referencing technique to the brightest maser feature. (a) Continuum map at 22 GHz made from data taken in March 1997. The size of synthesized beam is 0.56×0.49 mas^2. The contour levels are (4, 7, 10, 15, 20)$\times$0.24 mJy beam^{-1}. The peak intensity is 5.9 mJy beam^{-1}. (b) Continuum map at 22 GHz made from data taken in October 1997. The size of synthesized beam is 0.41×0.30 mas^2. The contour levels are (4, 7, 10, 15, 20, 25)$\times$0.49 mJy beam^{-1}. The peak intensity is 8.4 mJy beam^{-1}.

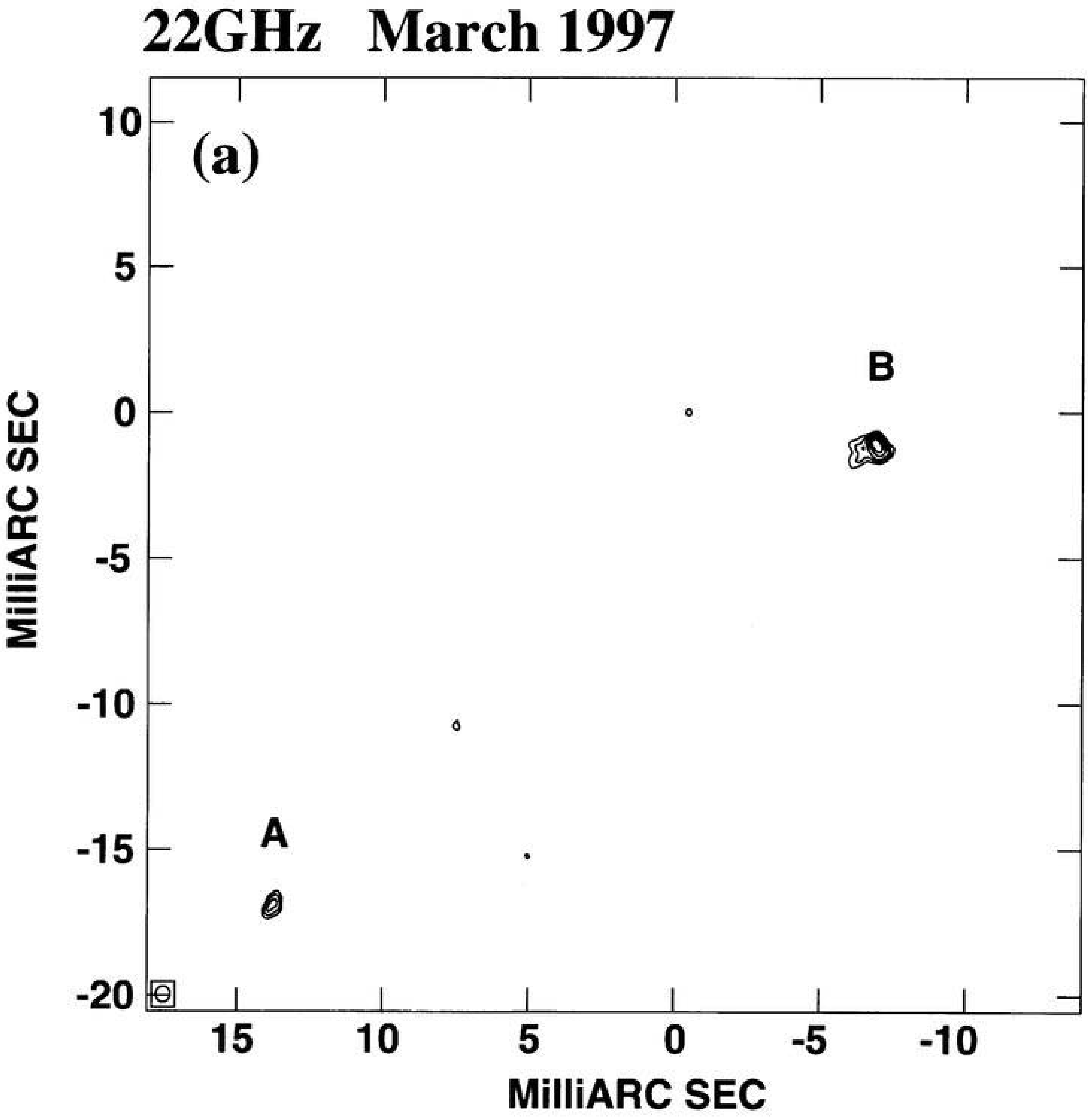
22GHz March 1997
(a)
B
A
10
5
0
-5
-10
-15
-20
15
10
5
0
-5
-10
MilliARC SEC
MilliARC SEC

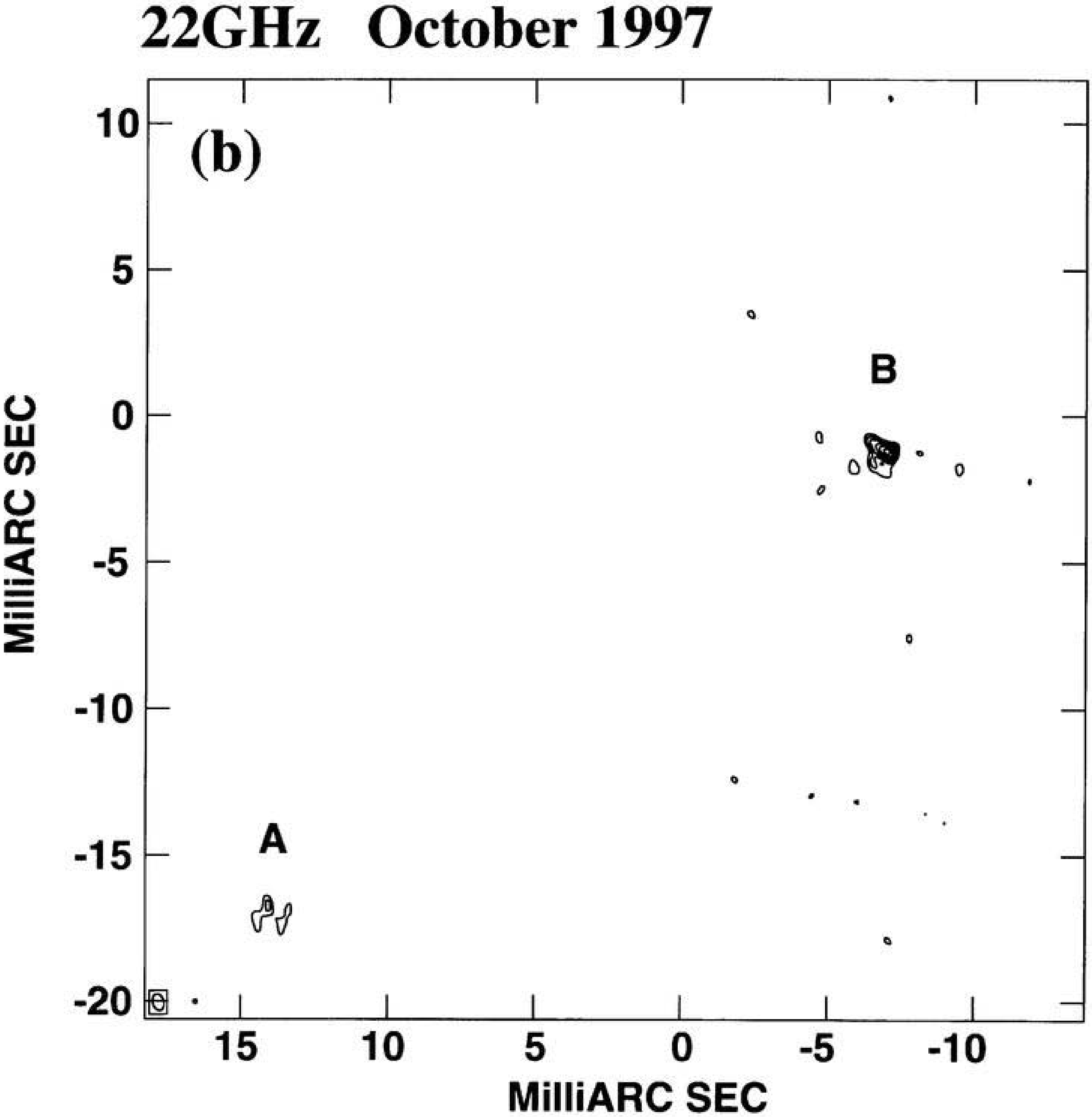
22GHz October 1997

Figure 3.4: Comparison of the continuum spectrum for each component in the nuclear region of NGC 3079. The flux densities of component A+C are obtained by convolution with the beam size of 14.7×12.8 mas as used at 1.4 GHz. Error bars represent ± 1σ. At 1.4 GHz, we could not resolve component C from A. Considering the spectral continuity between 1.4 GHz and 8.4 GHz, the single component seen at 15 GHz and 22 GHz can be identified as the component B seen at 1.4 GHz and 8.4 GHz.

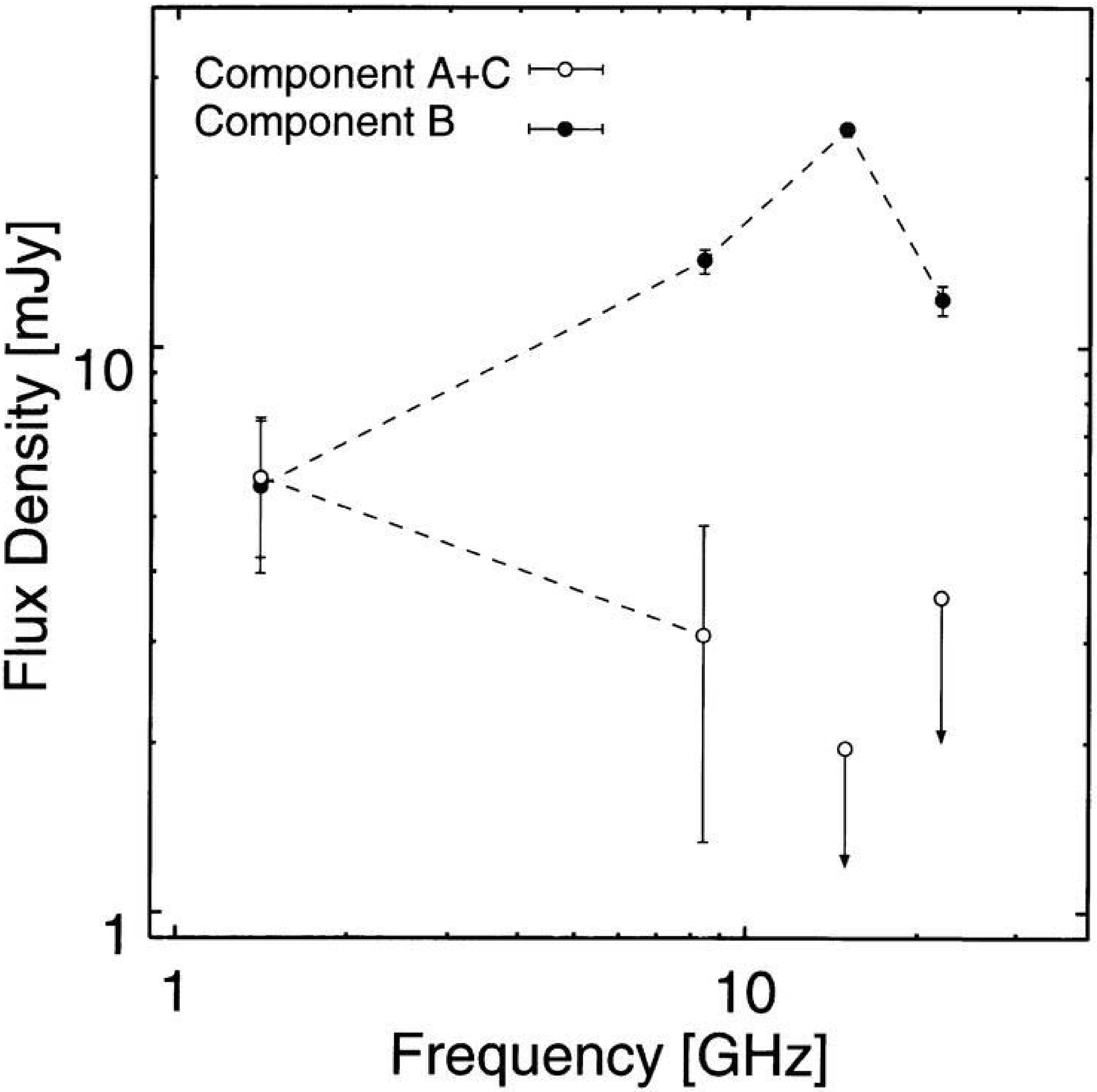

Component A+C
Component B
Flux Density [mJy]
10
1
1
10
Frequency [GHz]

Chapter 4

Maser Distribution

4.1 Spectral Profiles of Maser Emission

Cross-power spectra of the H_2O maser emission are shown in figures 4.1(a)–(c). The velocity resolution is 0.4 km s^{-1}. Features weaker than 5σ are not shown. The color indicates the radial velocity range of the profile. The doppler shift of the maser emission covers from 917 to 1204 km s^{-1} except for the first epoch, where the range was from 917 to 1007 km s^{-1}. In figure 4.2, we show spectral profiles of the three epochs with a velocity range of 940–1020 km s^{-1}. These profiles show no clear velocity shift of the peak, while a significant time-variability of the flux density in one year from October of 1996 to October of 1997 can be seen. The peak flux at the first epoch was about 2 Jy. It increases to 3 Jy in five months, and then decreased to ~2.5 Jy in seven months. This variation is within the range of 1–8 Jy shown by a monitoring program from 1984 to 1994 (Baan and Haschick 1996). The flux densities of the continuum components did not vary as the peak of maser emission did during our observations. A clear relation between the flux densities of maser peak and continuum components is not found from 1996 to 1997. At the first and second epochs, the maser emission had a double-peaked spectrum, while only one clear peak was seen at the third epoch, The strongest maser emission stayed at 956–967 km s^{-1} for all epochs, and this feature was used as the phase reference in these observations.

4.2 Positions of Maser Spots

The relative positions of each H_2O maser spot overlayed on the continuum contour for each epoch are shown in figures 4.3(a)–(c). The color of the full circles reflects the velocity range of the H_2O maser emission in figure 4.1. Maser features were distributed into two groups and one spot. Mainly, maser features with a velocity range of 920–1020 km s^{-1} are distributed in a compact group within radius of 0.05 pc, 6.7 mas east of the component B. This first group, which includes the strongest maser at 956 km s^{-1}, has most blueshifted velocity, and consists of three or four subgroups. There is second group located 7 mas (0.5 pc) north of the first group, with the velocity range of 997–1070 km s^{-1}. The last maser spot at 1202 km s^{-1} redshifted from the V_{sys} is located 15 mas (1.2 pc) south of the first group. All maser features are spread across 20 mas in the north-south direction (P.A. $\sim -10°$), almost parallel to the major axis of the galaxy.

The distribution of prominent peaks of maser emission at velocity from 940 to 990 km s^{-1} is shown in figure 4.4. These maser features belong to the first group. Significant motions between from October 1996 and October 1997 are not found for all maser features: only a positional change of the maser feature at 980 km s^{-1} is seen. The position of this feature at 980 km s^{-1} is shifted about 0.005 pc to south significantly during 7 months from March to October in 1997. We consider that the maser features at 980 km s^{-1} detected in two epochs (March and October in 1997) are different spots. Because if the maser feature at 980 km s^{-1} of October is the same as that of March, the feature should move to the south with an apparent velocity of ~10000 km^{-1}, while no other features have such rapid motion. We do not detect significant motion of the other maser features except "switch-on" and "switch-off" of maser emission are seen like the feature at 980 km s^{-1}. The three epoch distributions from October 1996 to October 1997 are consistent each other, and also agree well with the map of T98 in January 1995. No significant motion of maser groups is seen during the 32 months from January of 1995 (T98) to October of 1997.

4.3 Relative Position to Continuum Components

By the use of phase-referencing, we see the relative positions between the maser and the continuum components A and B at 22 GHz, as seen in figure 4.5. From these, no maser emission is coincident with any detected continuum component for all epochs. The spatial separation between the maser groups and the continuum components agree with that of the previous observation in 1995 by T98.

However, the monitoring observations at 22 GHz show the change of the relative position from the continuum components and the reference maser. The relative positions of the component A and B from the reference maser feature at 956 km s^{-1} are listed in table 4.1, and are plotted in figure 4.5. In giving a single position for Component A and B, we used a single Gaussian fit to an image with a 100 Mλ Gaussian taper applied to (u, v) weights before imaging as done in previous result by T98. The position of A relative to the reference maser feature moved with an apparent subluminal velocity (~0.2c) from January of 1995 to October of 1997, along the SE-NW direction (P.A. ~ 140°). The apparent velocity and the direction of the motion of B relative to the reference maser feature are similar to those of the subluminal motion between A and B. On the other hand, the position of B did not show such a rapid change during the 32 months except the separation between B and the maser moved from October of 1996 to March of 1997. In this period from October in 1996 to March in 1997, the continuum structure of B changed, as described in Chapter 3. In March and October of 1997, the extended structure of B is detected, and the relative change between B and the maser is small (< 0.5 mas) during this 7 months from March to October in 1997.

Thus, all results from the monitoring observations of the H_2O maser emission suggest that all maser features are gravitationally bound to the central mass, which is B, or is located very close to B rather than A.

4.4 Velocity Structure of Maser

T98 suggested that the overall distribution of maser velocities was consistent with a parsec-scale edge-on molecular disk that is rotating in the same sense as the kiloparsec-scale molecular

Table 4.1: Relative position of continuum components from the strongest maser

epoch (1)	Component (2)	RA-Offset [mas] (3)	DEC-Offset [°] (4)
1995 January (T98)	A	12.7±0.3	-15.9±0.3
	B	-6.59±0.03	-1.09±0.04
1996 October	B	-6.60±0.05	-0.96±0.04
1997 March	A	13.4±0.3	-16.7±0.2
	B	-6.79±0.05	-1.26±0.05
1997 October	A	13.8±0.2	-16.9±0.3
	B	-6.73±0.10	-1.26±0.08

Col.(1) epoch of observation ; Col.(2) name of continuum component; Col.(3) RA-Offset relative to the reference maser feature at velocity of 956 km s^{-1}; Col.(4) DEC-Offset relative to the reference maser feature at velocity of 956 km s^{-1}.

clouds. We examined position-velocity diagrams along many directions through the maser features. Two position-velocity (P-V) examinations of the maser features are shown here. The first diagram, figure 4.6, is plotted along the galactic disk (P.A. ~ 165°). The positional origin is the strongest maser at 956 km s^{-1}. The P-V distribution along the galactic disk does not indicate clear rotation curve along the galactic rotation. The magnified P-V plots of each groups are shown in figure 4.7. Some velocity gradients are seen in each group. The second diagram, figure 4.8, is done along the direction of alignment of continuum components (P.A. ~ 127°), and its magnified plots are shown in figure 4.9. In the diagram along the continuum components (figure 4.8), the velocity trend can be seen in the maser features close to the brightest feature at 956 km s^{-1}, while it is not clear in the overall maser distribution. We did not found any clear velocity structure of the whole maser distribution along any direction.

Figure 4.1: Observations of H_2O maser emission were carried out at three epochs, on October 20 of 1996, March 7 and October 2 of 1997. The observed velocity range was, 590–1008 km s^{-1} for the first epoch and 832–1222 km s^{-1} for the second and third epochs, respectively. Cross-power spectra of H_2O maser emission for NGC 3079 measured on 1996 October (a), 1997 March (b) and October (c) are shown. The arrow indicates the systemic velocity of the galaxy.

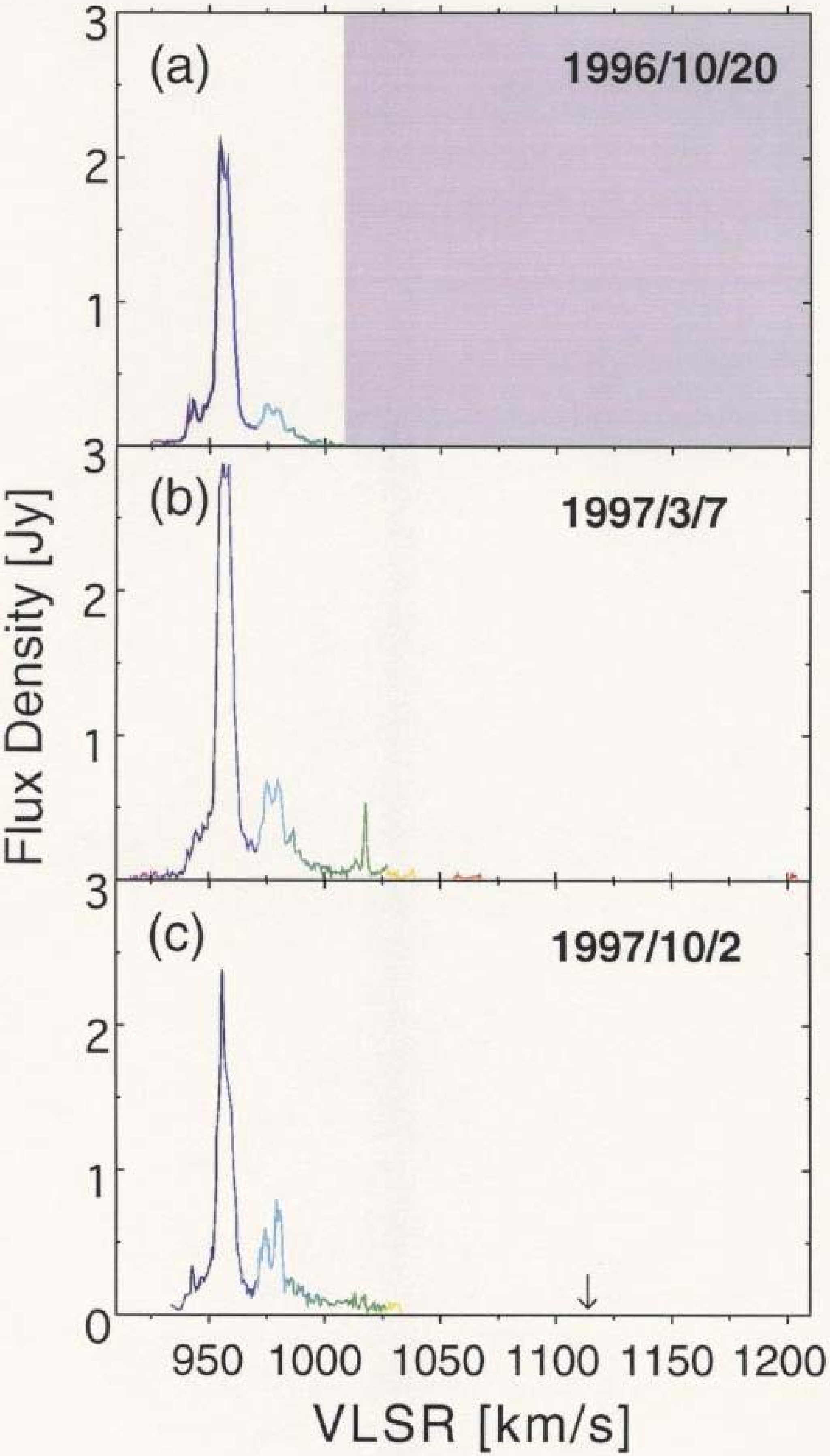
(a)
1996/10/20
(b)
1997/3/7
(c)
1997/10/2
Flux Density [Jy]
3
2
1
0
950
1000
1050
1100
1150
1200
VLSR [km/s]

Figure 4.2: Comparison of the H_2O maser spectra of 1996 October (dashed line), 1997 March (dotted line), and October (solid line). The velocity range shown is from 938 to 1022 km s^{-1}. No significant velocity drift is seen.

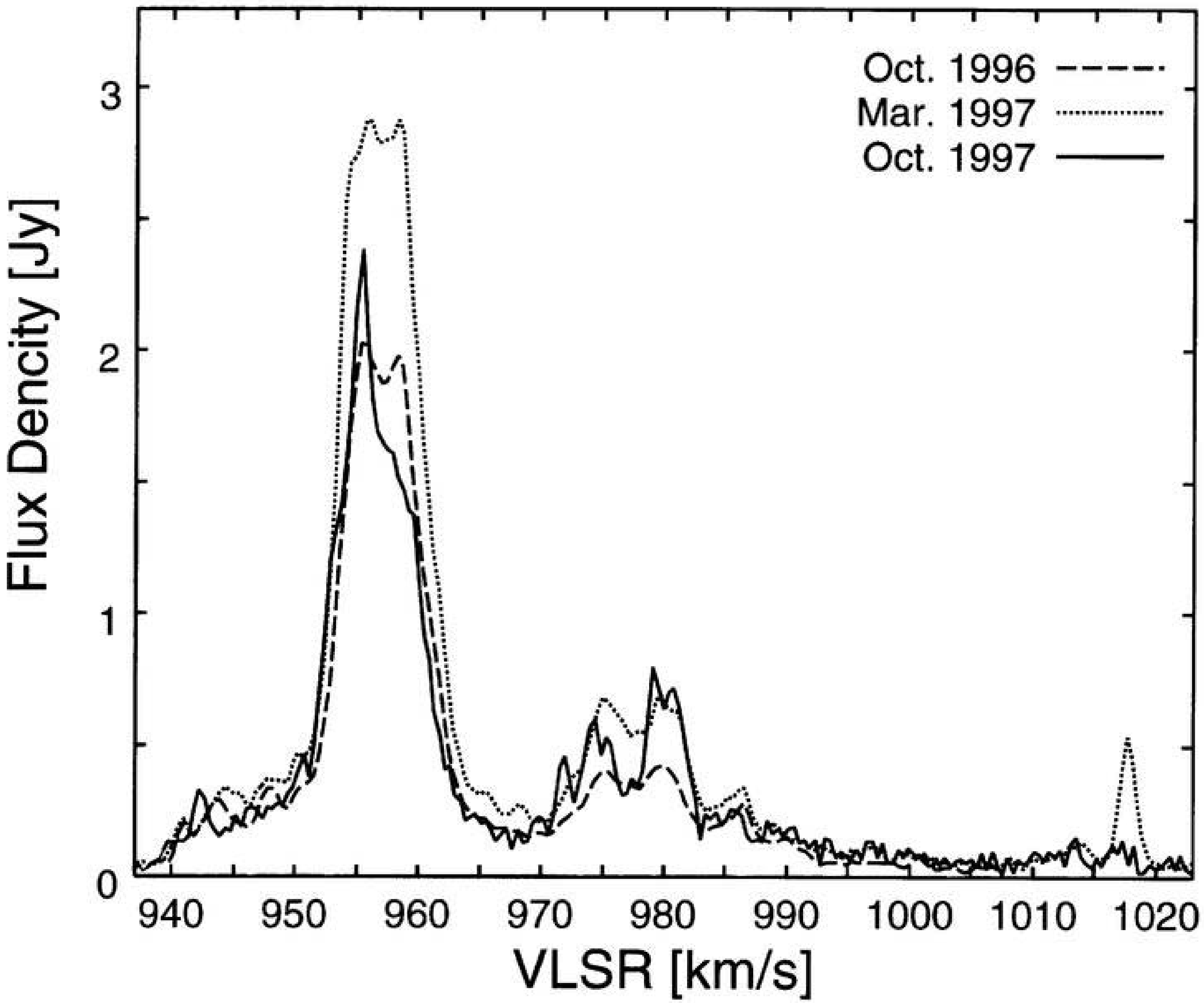
Oct. 1996
Mar. 1997
Oct. 1997
Flux Dencity [Jy]
0
1
2
3
940
950
960
970
980
990
1000
1010
1020
VLSR [km/s]

Figure 4.3: Maps of the distribution of H_2O maser emission overlayed on the continuum contours in the parsec-scale region measured on 1996 October (a), 1997 March (b) and October (c). Color of the circles reflect the velocity shift of the H_2O maser emission in figure 4.3. Maser features detected at the greater than 5 σ level for each spectral channel were plotted.

22GHz October 1996

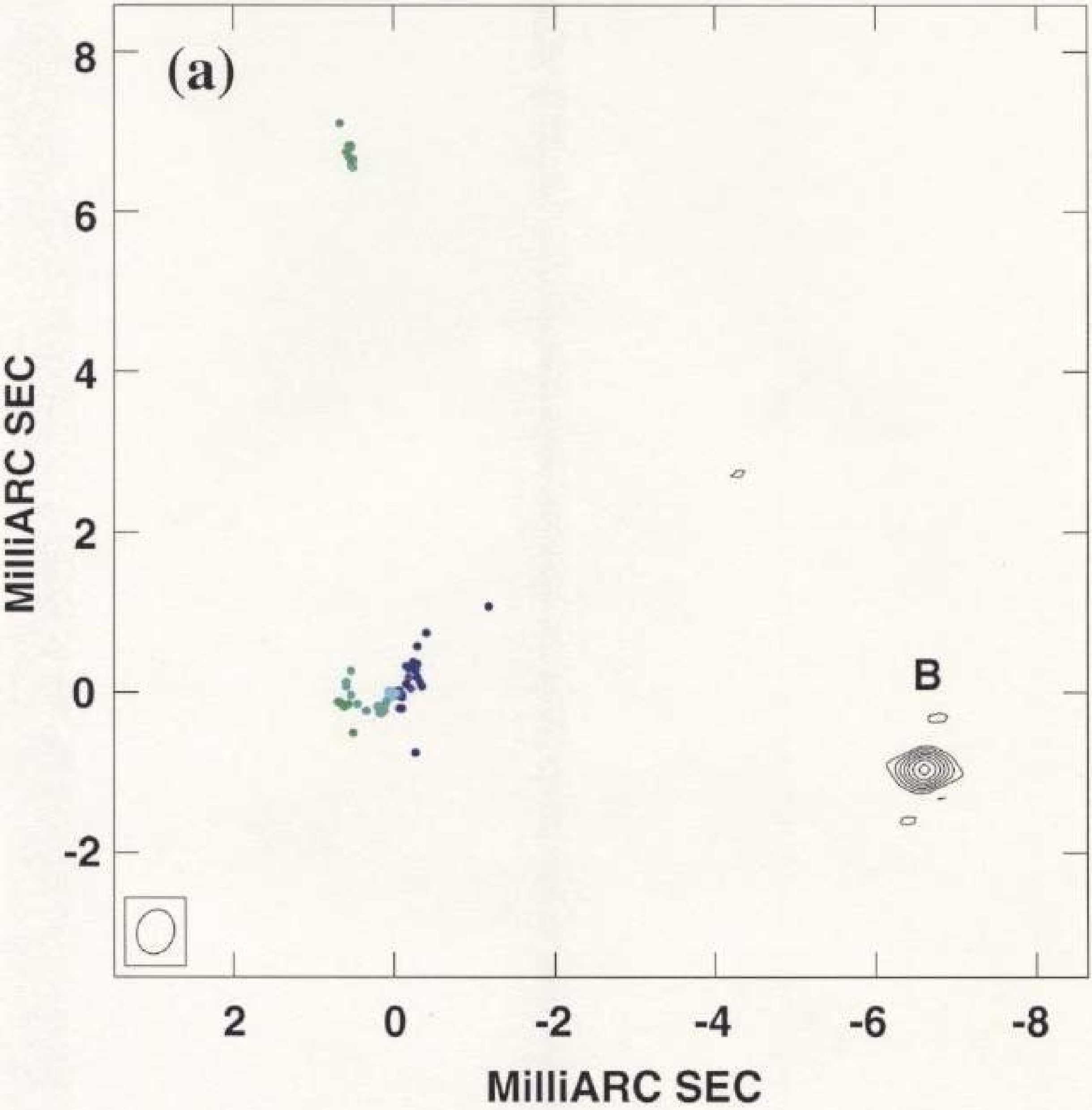

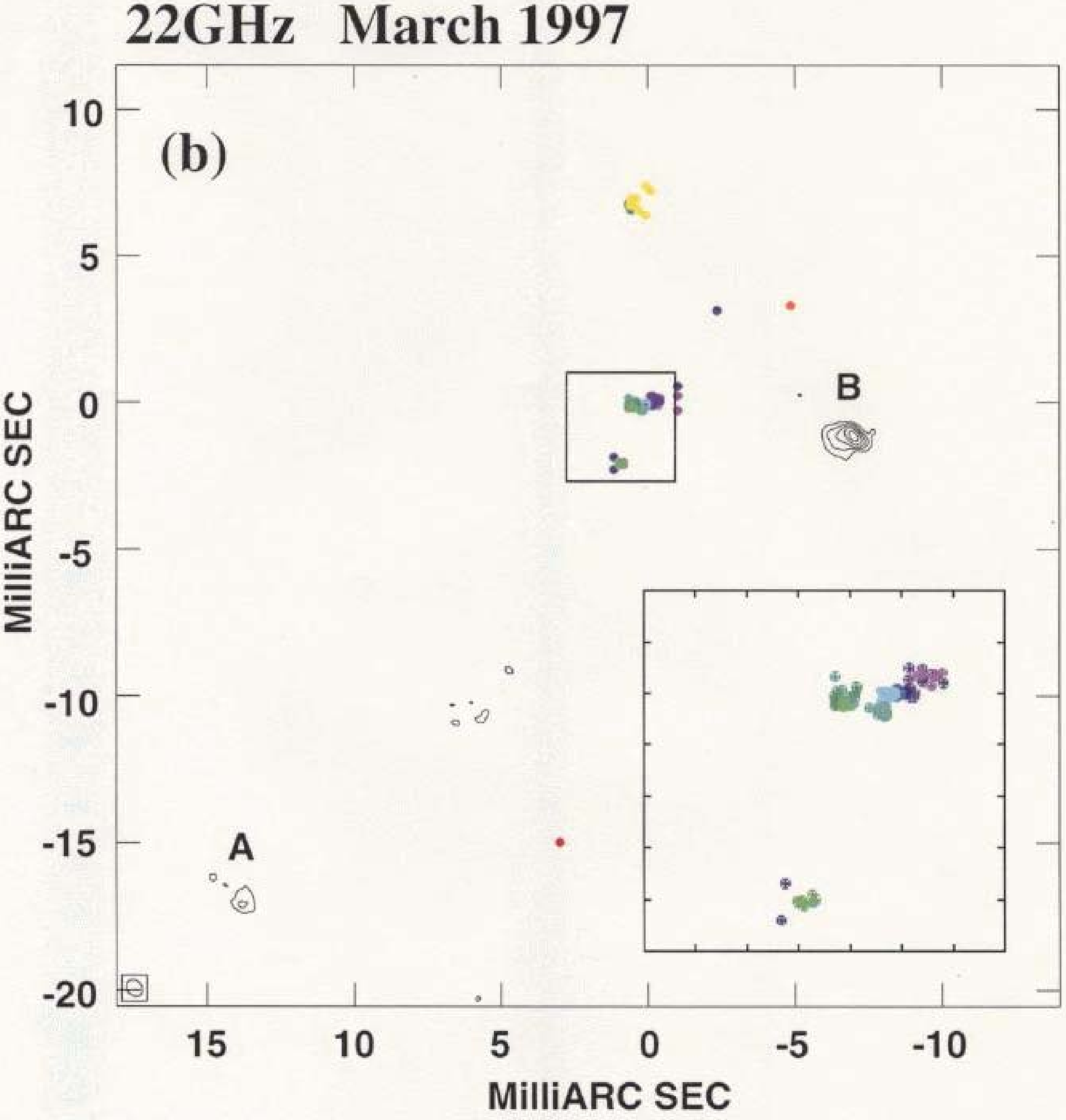
22GHz March 1997
(b)
A
B
MilliARC SEC
MilliARC SEC
10
5
0
-5
-10
-15
-20
15
10
5
0
-5
-10

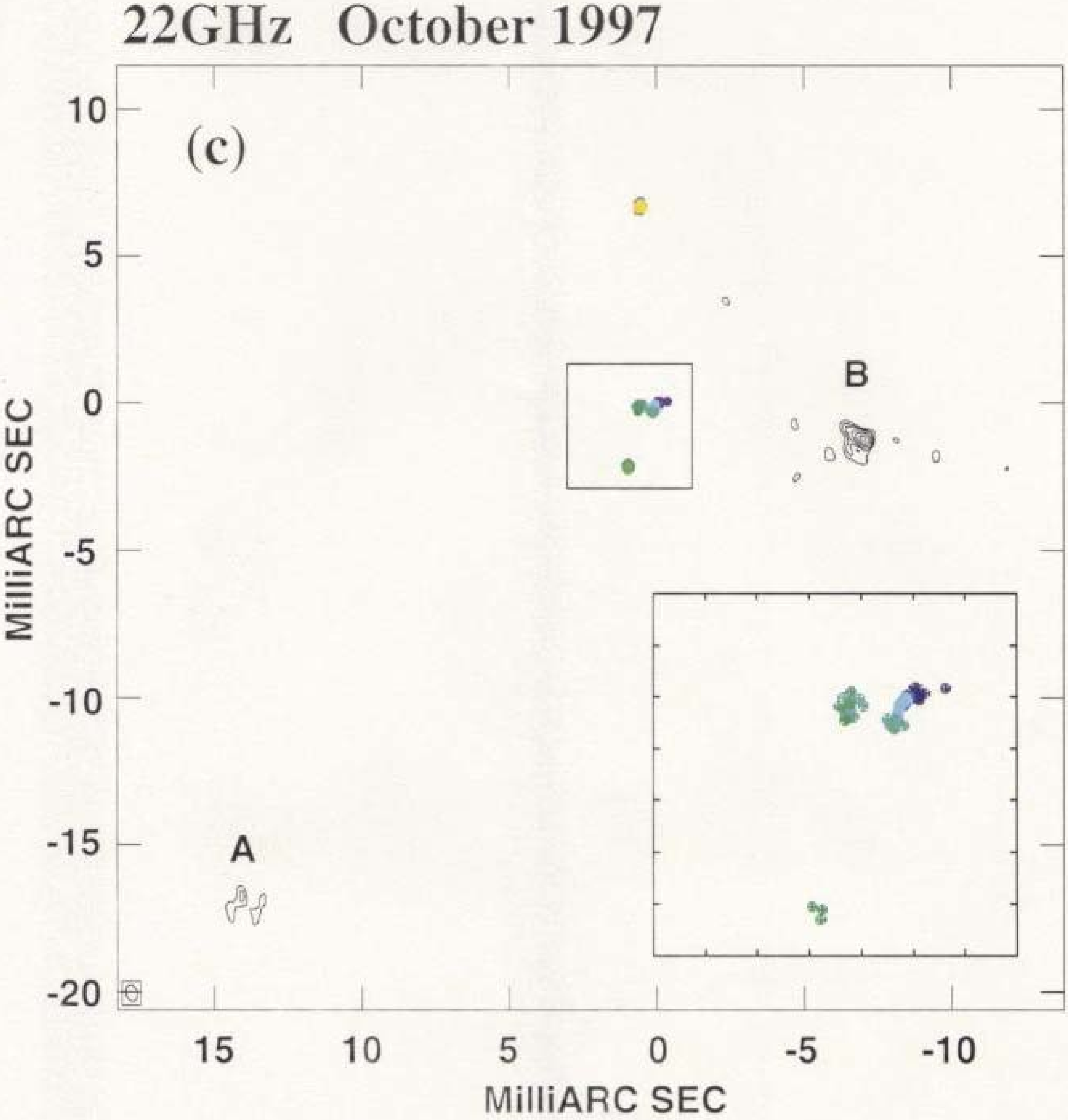

22GHz October 1997

Figure 4.4: Distribution of prominent peaks of maser emission at velocity from 940 to 990 km s^{-1} for three epochs; October 1996 (circle), March 1997 (triangle) and October 1997 (square).

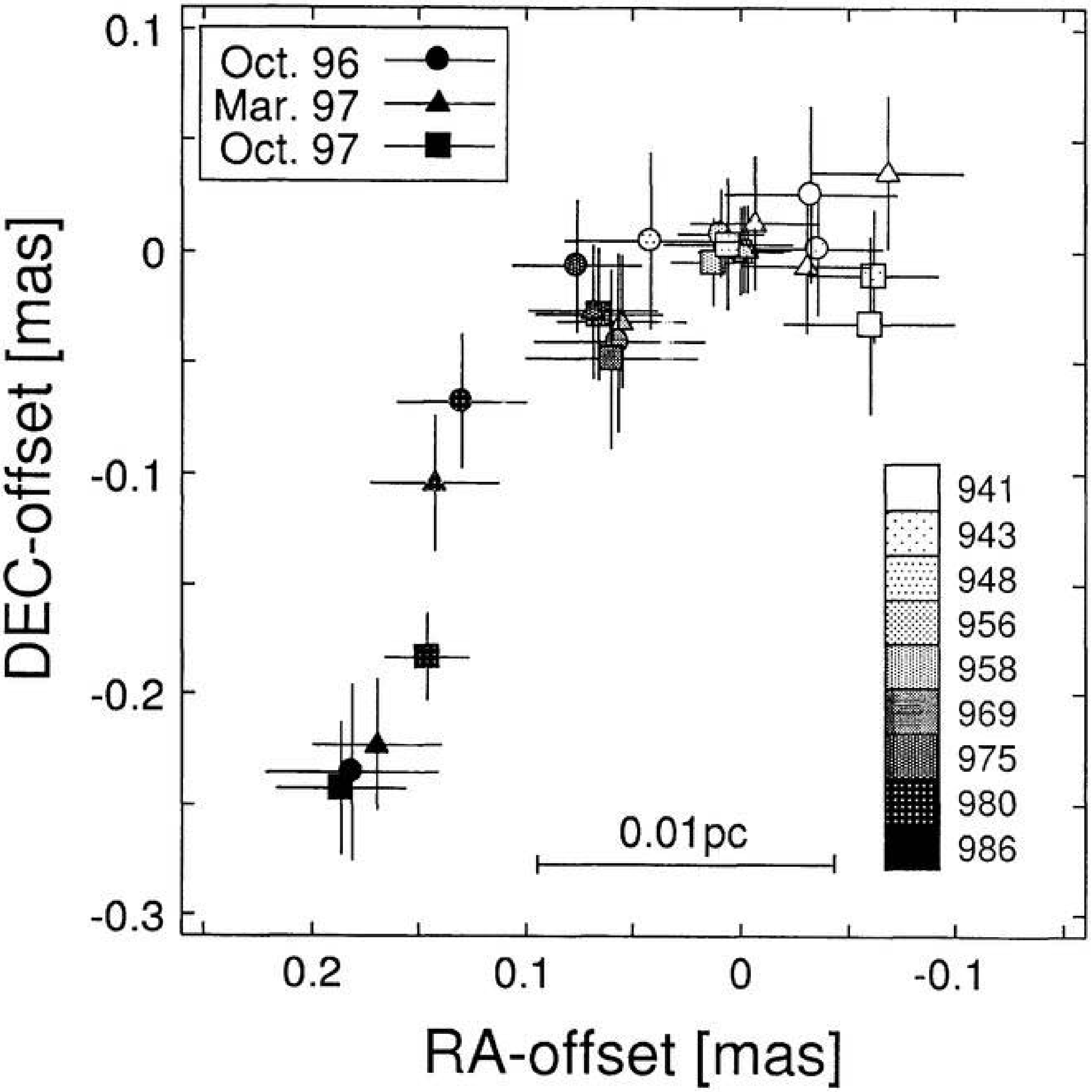
Oct. 96
Mar. 97
Oct. 97
DEC-offset [mas]
RA-offset [mas]
0.1
0
-0.1
-0.2
-0.3
0.2
0.1
0
-0.1
0.01pc
941
943
948
956
958
969
975
980
986

Figure 4.5: Motion of the components A and B from the reference maser feature at 956 km s^{-1}. We obtained the single positions by fitting a single Gaussian model of the images to tapered (100 Mλ) visibilities. The positions for January 1995 were estimated by T98.

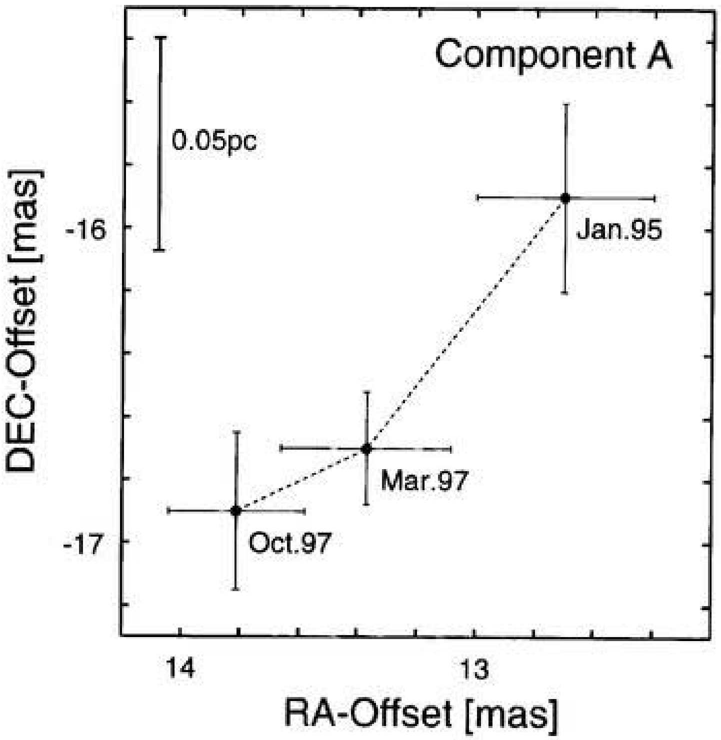
Component A
0.05pc
Jan.95
Mar.97
Oct.97
-16
-17
14
13
DEC-Offset [mas]
RA-Offset [mas]

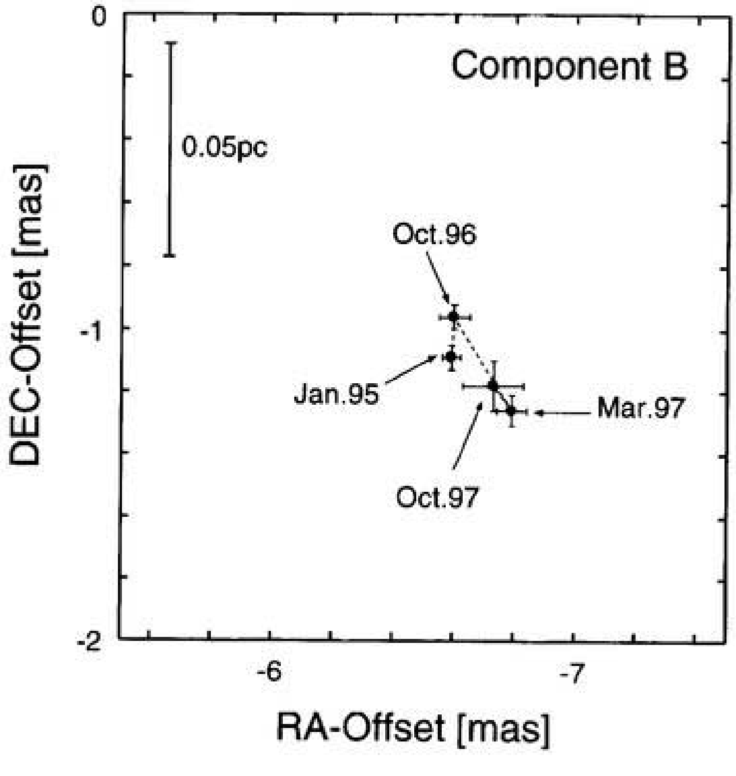
Component B
0.05pc
Oct.96
Jan.95
Mar.97
Oct.97
0
-1
-2
-6
-7
DEC-Offset [mas]
RA-Offset [mas]

Figure 4.6: Position-velocity diagram of the H_2O maser features obtained from the data taken in March 1997 (second epoch). The position direction is along the galactic disk (P.A. $\sim -15^\circ$). The rectangular sections are magnified in figure 4.7.

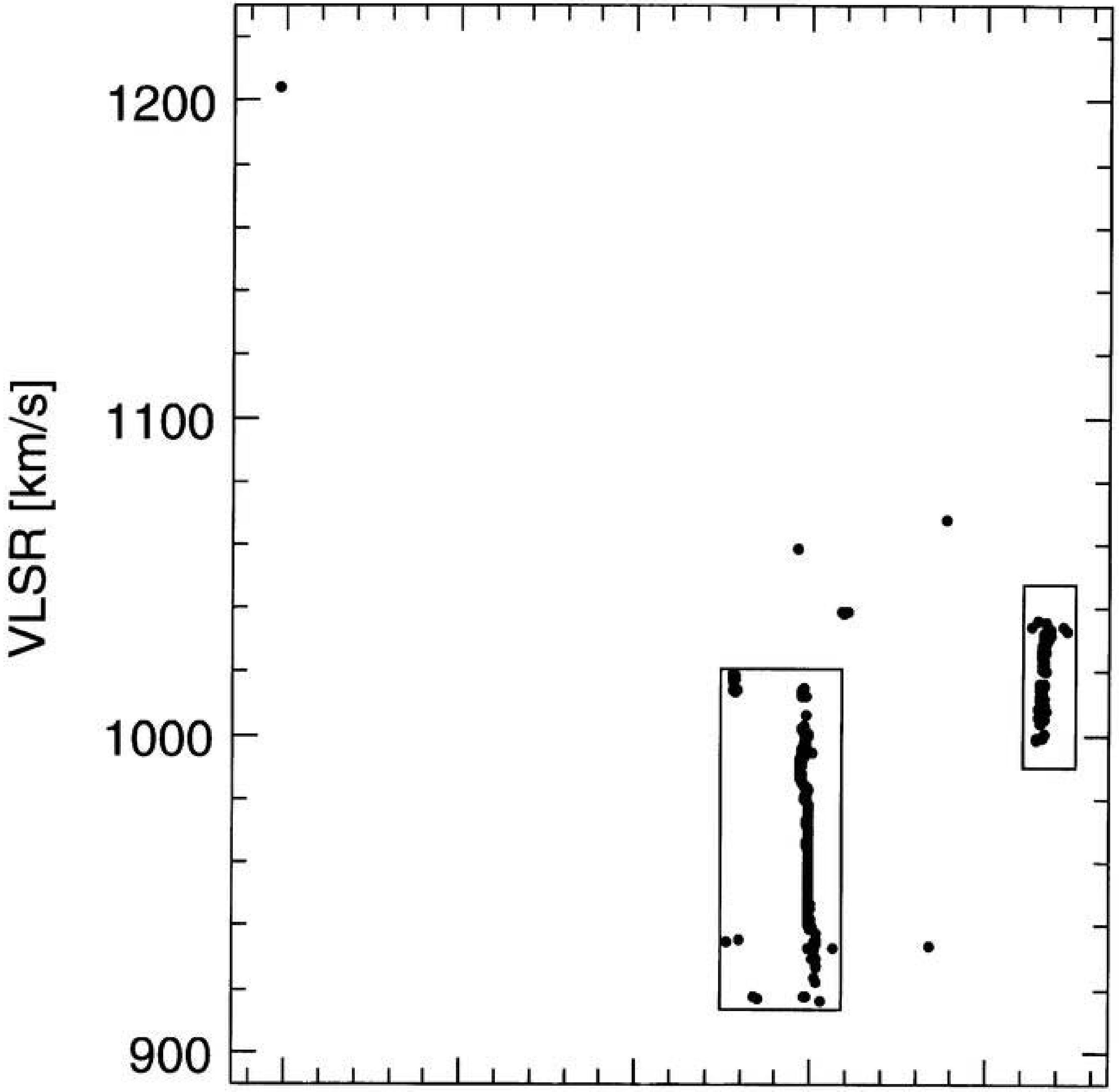
1200
1100
1000
900
VLSR [km/s]
-15
-10
-5
0
5
Position along the disk direction [mas]

Figure 4.7: Magnified position-velocity diagrams. The position direction is along the galactic disk (P.A. ~ −15°) (a) Plot of the first H_2O maser group including the strongest maser feature at 957 km s^{-1}. (b) Plot of the second H_2O maser group.

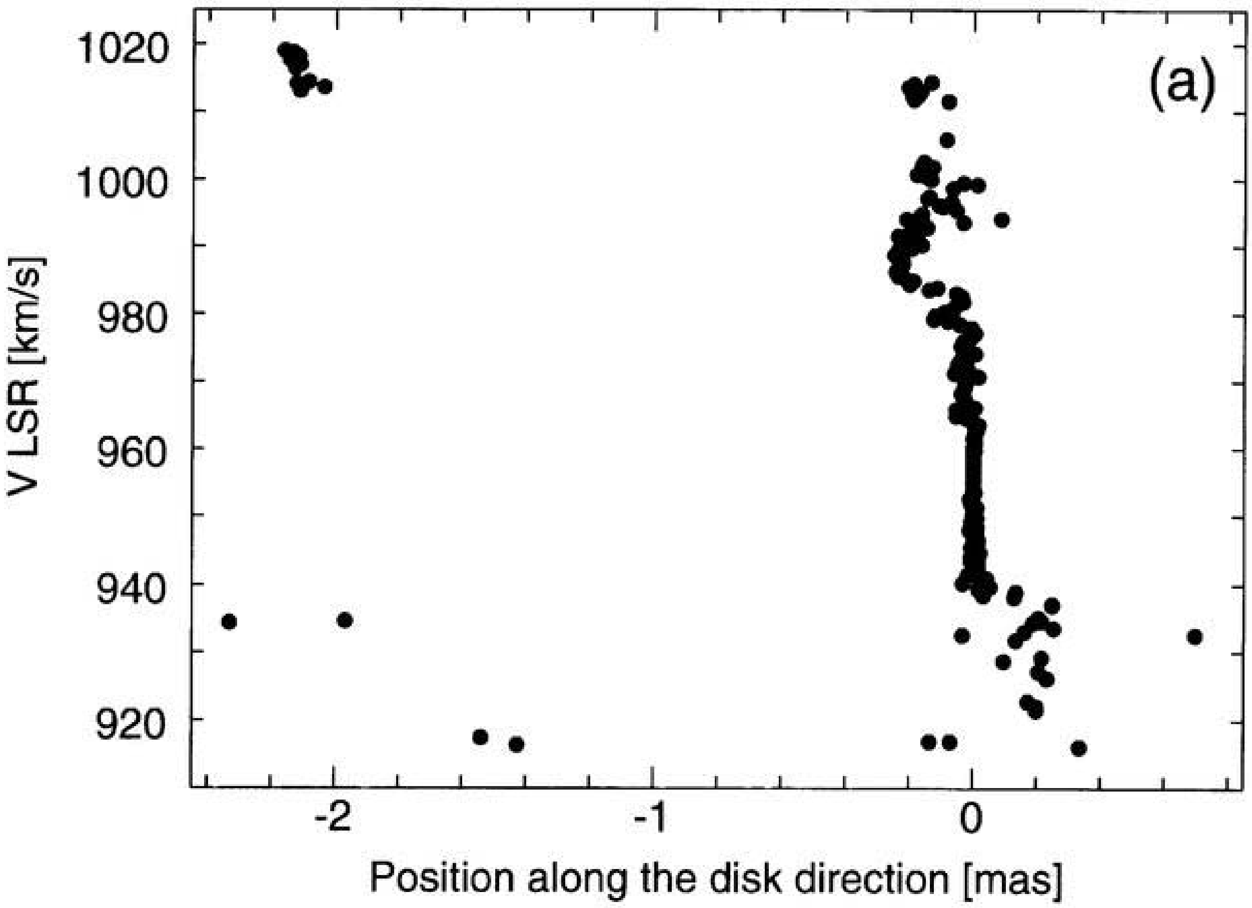
(a)
V LSR [km/s]
1020
1000
980
960
940
920
-2
-1
0
Position along the disk direction [mas]

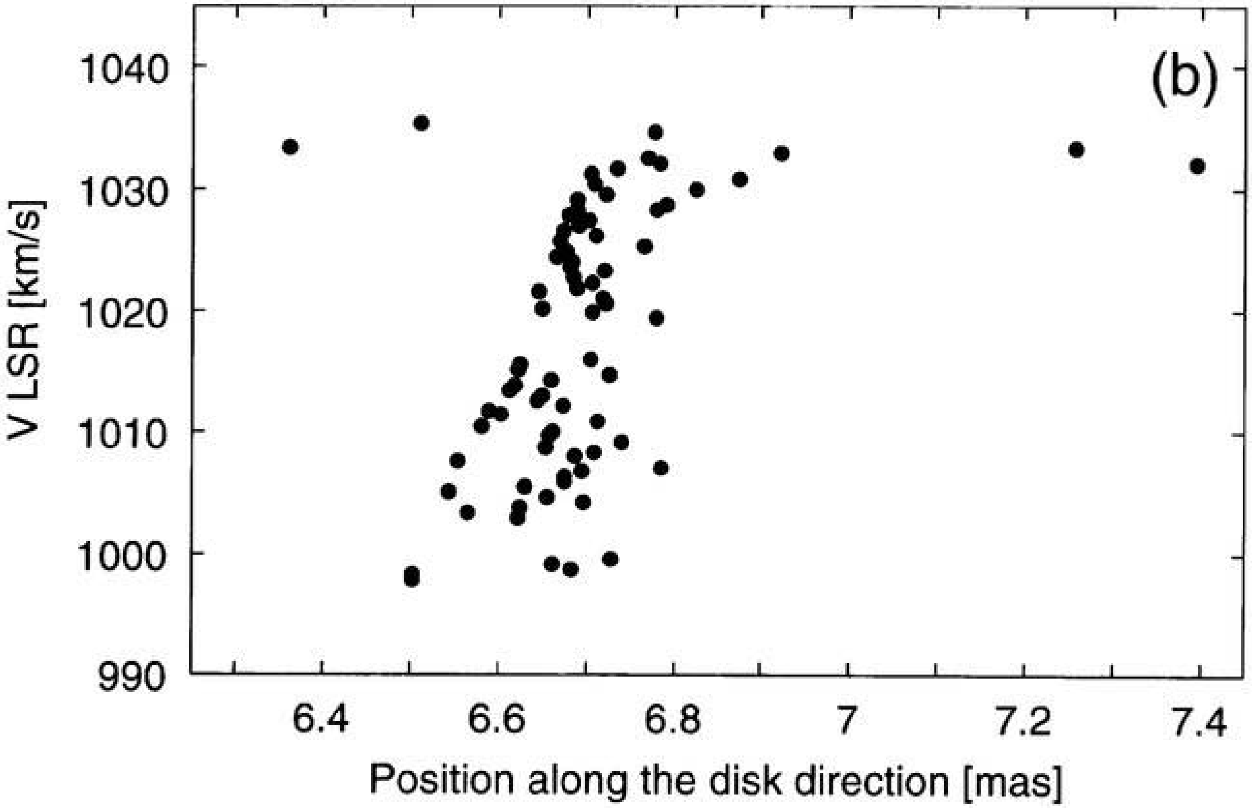
(b)
V LSR [km/s]
1040
1030
1020
1010
1000
990
6.4
6.6
6.8
7
7.2
7.4
Position along the disk direction [mas]

Figure 4.8: Position-velocity diagram of the H_2O maser features obtained from the data taken in March 1997 (second epoch). The position direction is along the alignment of the continuum components (P.A. ~127°)

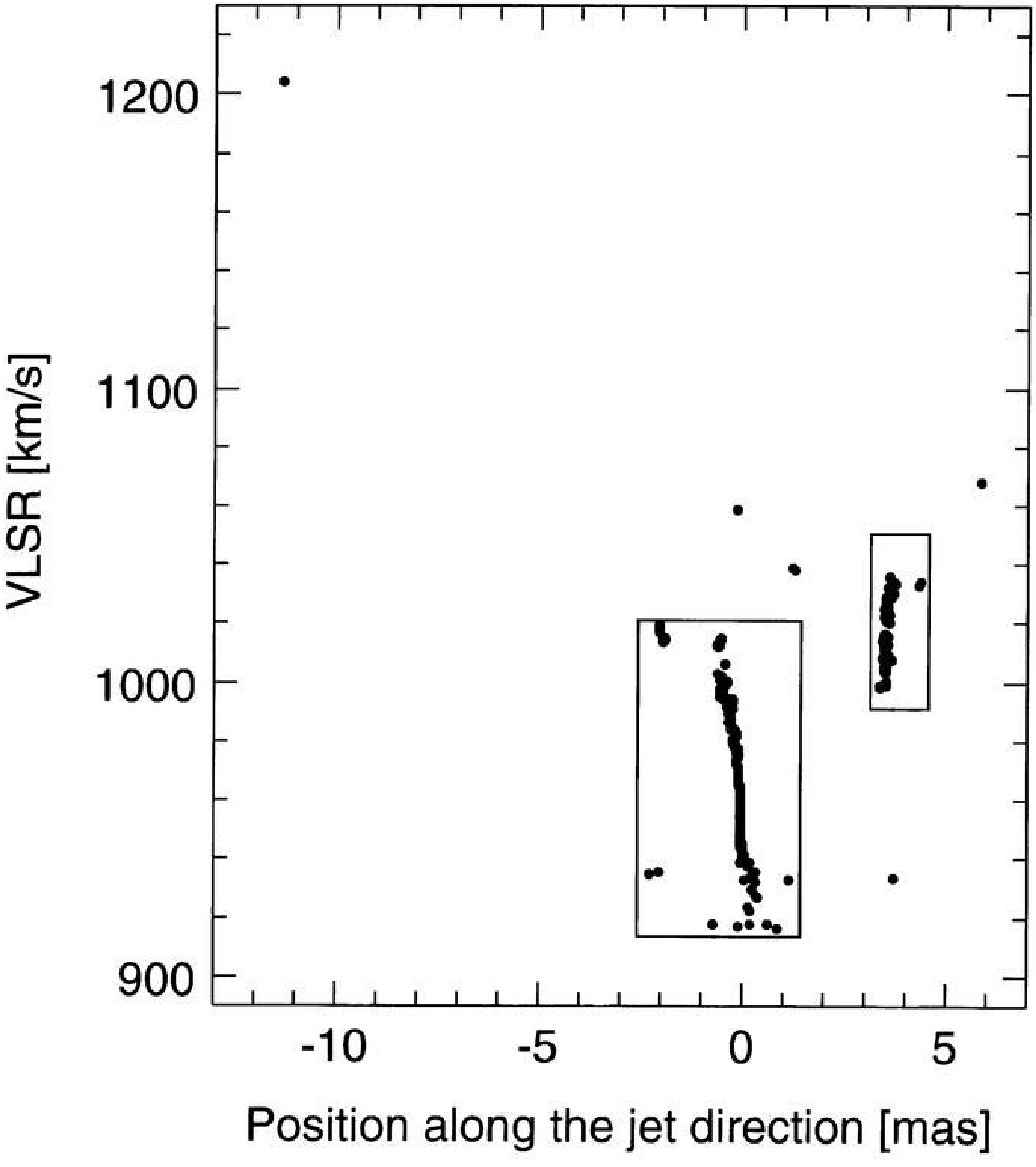

1200
1100
1000
900
VLSR [km/s]
-10
-5
0
5
Position along the jet direction [mas]

Figure 4.9: Magnified position-velocity diagrams. The position direction is along the alignment of continuum components (P.A. ~127°) (a) Plot of the first H_2O maser group including the strongest maser feature at 957 km s^{-1}. (b) Plot of the second H_2O maser group.

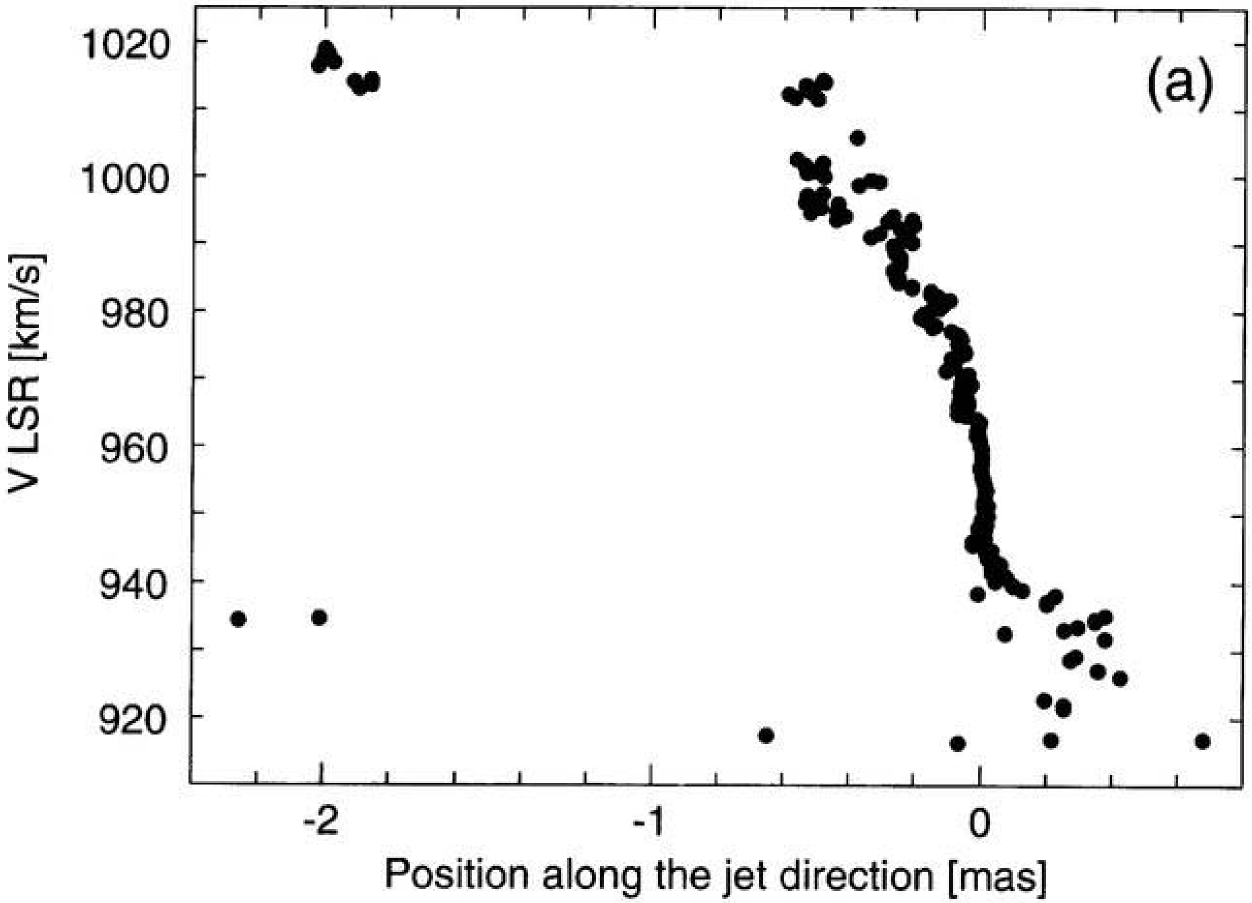
(a)
V LSR [km/s]
1020
1000
980
960
940
920
-2
-1
0
Position along the jet direction [mas]

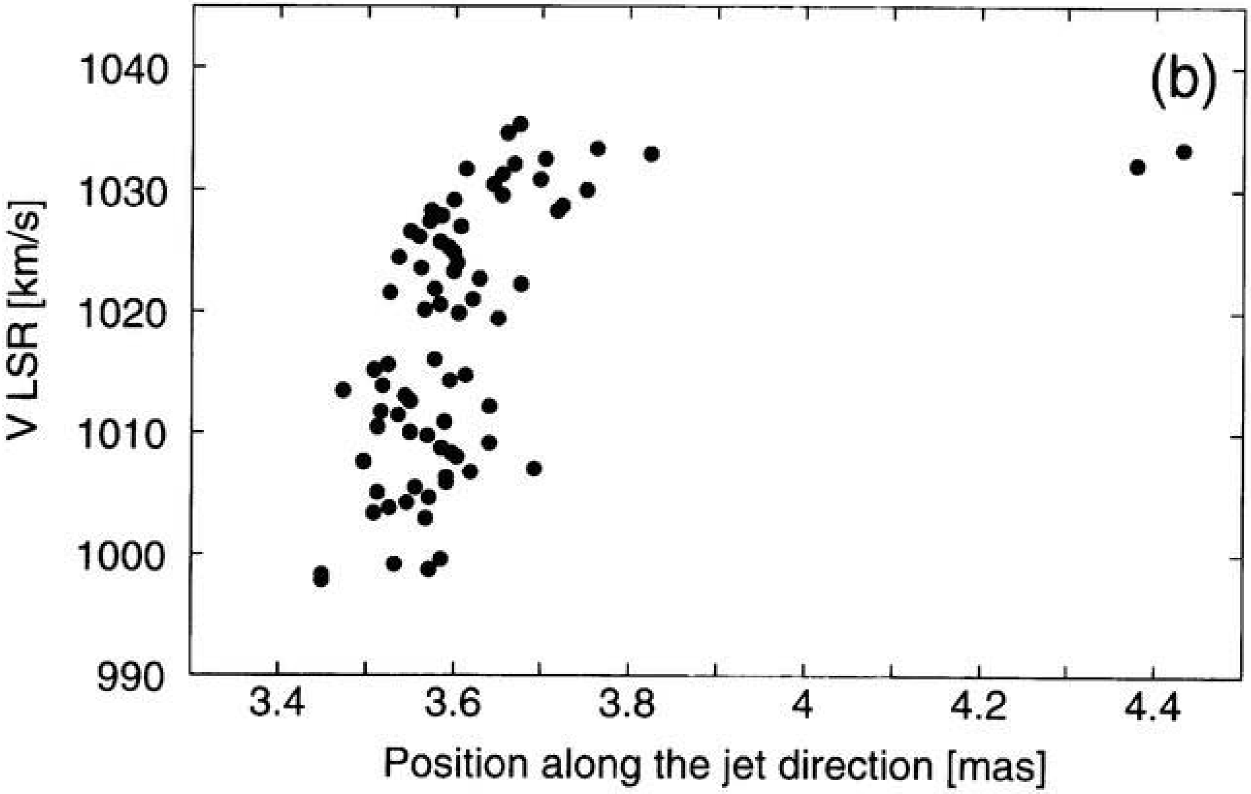
(b)
V LSR [km/s]
1040
1030
1020
1010
1000
990
3.4
3.6
3.8
4
4.2
4.4
Position along the jet direction [mas]

Chapter 5

HI and OH Absorptions

5.1 HI Absorption

The cross-power spectral profile of H I absorption is shown in figure 5.2. The velocity resolution is 6.6 km s^{-1}. The spectrum was obtained from data of the baselines between FD, GB, KP, LA, OV, PT and Y. We performed a four-component Gaussian fitting to the profile to get the minimum χ^2. The velocity centers of the four best-fit Gaussian components are at 1003±4, 1060±11, 1135±3 and 1231±4 km s^{-1}. The absorption feature at 1060 km s^{-1} has a broad profile of FWHM $\sim$ 265±23 km s^{-1}. The three other absorption features show narrower profiles. The parameters of the absorption features are listed in table 5.1, where we give the central velocity of the features, FWHM, the optical depth, and the column density of H I. The column densities of H I, N_{HI}, are given as

$$N_{\mathrm{HI}} = 1.82 \times 10^{18} T_{\mathrm{spin}} \int \tau_{\mathrm{HI}} dv \,\mathrm{cm}^{-1} \tag{5.1}$$

where T_{spin} is the spin temperature in K and τ_{HI} is the HI opacity (e.g. Spitzer 1978). Assuming $T_{\mathrm{spin}} = 100$ K, which is the same value for H I clouds in the Galaxy, the column densities in each component are 10^{21}–10^{22} atoms cm^{-2}. If, however, the clouds are close to the central continuum sources, their spin temperature will be increased by the radiation field. The hard X-ray observation with *ASCA* implies a H I column density of $\sim 10^{22}$ atoms cm^{-2} (Serlemitsos et al. 1997; Dahlem et al. 1998; Terashima 1998). However, if we assume that the observed hard X-ray luminosity is reflection dominated, or the nucleus is hidden like NGC 1068 (e.g.

Koyama et al. 1989), the column density would be $> 10^{24}$ atoms cm^{-2} (Fukazawa, private communication).

Table 5.1: Column density of H I absorption

Velocity [km s^{-1}]	Δv [km s^{-1}]	Optical Depth τ_{HI}	$N_{\mathrm{HI}}/T^{*}_{\mathrm{spin}}$ [10^{19} cm^{-2} K^{-1}]
1003± 4	41±12	0.24±0.06	1.8±0.7
1061±11	265±23	0.61±0.07	29.5±4.1
1135± 3	64±10	0.58±0.09	6.8±1.5
1231± 4	31±11	0.21±0.07	1.2±0.6

$*$ A spin temperature

The conitinuum image without the absorption line is shown in figure 5.2. Figure 5.2 shows the continuum-subtracted maps of the individual channels of the cube. The channel spacing is 52.8 km s^{-1} by smoothing in frequency. The velocity range of the absorption associated with B is 889–1258 km s^{-1}, while the absorption with velocities less than 942 km s^{-1} is not detected toward A. This trend can be seen in figure 5.2 clearly. Figure 5.2 is a position-velocity diagram along the A-B axis (P.A.∼140°). The strongest H I absorption close to V_{sys} can be seen in the whole structure, and two peaks of the absorption are associated with A and B. The second strongest absorption feature near 1000 km s^{-1} is also associated with both A and B. The absorption near 1250 km s^{-1} can be seen associated with A, probably with both A and B, although the absorption near 1250 km s^{-1} is weak and shows no clear absorption peak on B. The absorption feature with a velocity peak around 1050 km s^{-1} has a wide velocity width and occurs mainly on B.

Figure 5.2 shows an isovelocity contour map which shows the velocity field, overlayed on continuum contours. The most remarkable result is a clear velocity gradient of absorption from east to west across B. The direction of the velocity gradient is nearly perpendicular to the galactic plane (P.A.∼164°). This suggests that it is not related to the galactic rotation. On the other hand, such a velocity gradient is not seen toward A.

5.2 OH Absorption

OH absorption profile is shown in figure 5.2 with velocity respected to 1667 MHz. The velocity resolution was 5.6 km s^{-1}. Double absorption peaks are seen in the spectrum. The dominant one is for absorption at 1667 MHz, and the weaker one at 1665 MHz. This profile agrees well with the profile obtained from single-dish observation (Haschick and Baan 1985). One peak appears at velocity of 1013±5 km s^{-1}, close to V_{sys}, and the other 1110±7 km s^{-1}, blueshifted from V_{sys}. However, we did not find either the redshifted feature from V_{sys} nor the broader feature seen in the H I spectrum. The 1665- MHz features in the OH spectrum were also detected, being offset by 352 km s^{-1} from the 1667-MHz features.

Table 5.2: Column density of OH absorption of 1667 MHz.

Velocity [km s^{-1}]	Δv [km s^{-1}]	Optical Depth τ_{OH1667}	$N_{\mathrm{OH}}/T^*_{\mathrm{ex}}$ [10^{16} cm^{-2} K^{-1}]	Line Ratio I_{1667}/I_{1665}	$N_{\mathrm{OH}}/N_{\mathrm{HI}}$
1013±5	53±12	0.73±0.17	9.2±2.9	1.2±0.4	$(5.1\pm2.5)\times10^{-3}$
1110±7	96±17	0.79±0.13	17.8±4.4	2.5±1.0	$(2.6\pm0.9)\times10^{-3}$

* An excitation temperature

Table 5.2 shows the properties of the OH absorption features, where we give the central velocity of the features, FWHM, the optical depth, the column density of OH, the line ratio of the 1667 and 1665 MHz features, and the ratio of OH and H I column densities. The column density of the OH 1667 MHz line, N_{OH} are given as

$$N_{\mathrm{OH}} = 2.35 \times 10^{14} T_{\mathrm{ex}} \int \tau_{\mathrm{OH}} dv \, \mathrm{cm}^{-1} \tag{5.2}$$

where T_{ex} is the OH excitation temperature and τ_{OH} is the OH opacity (Turner 1973). The line ratio I_{1667}/I_{1665} of the feature at 1013 km s^{-1} is 1.2, lying within the range of local thermodynamic equilibrium (LTE) values from 1.0 to 1.8. On the other hands, the feature at 1110 km s^{-1} has an extreme ratio of 2.5, which indicates a non-LTE excitation state. Observations by Dickey et al. (1981) have shown that five extragalactic sources (3C105, 3C111, 4C-02.74, 3C410, BL Lac) have non-LTE values of the line ratio, taking 40% of their sample detected OH absorption . The OH-to-H I ratio of column density was estimated assuming that the H I spin temperature and the OH excitation temperature are equal and that the same volume is being considered for both features.

Figure 5.1: H I 21 cm absorption spectrum toward the parsec-scale continuum source in NGC 3079. The velocity resolution is 6.5 km s^{-1}. The sum of the four Gaussian fits is represented by the dashed line ($\chi^2 = 75.9$, $\phi = 76$). The systemic velocity of the galaxy ($V_{\rm sys}$) is indicated by the arrow.

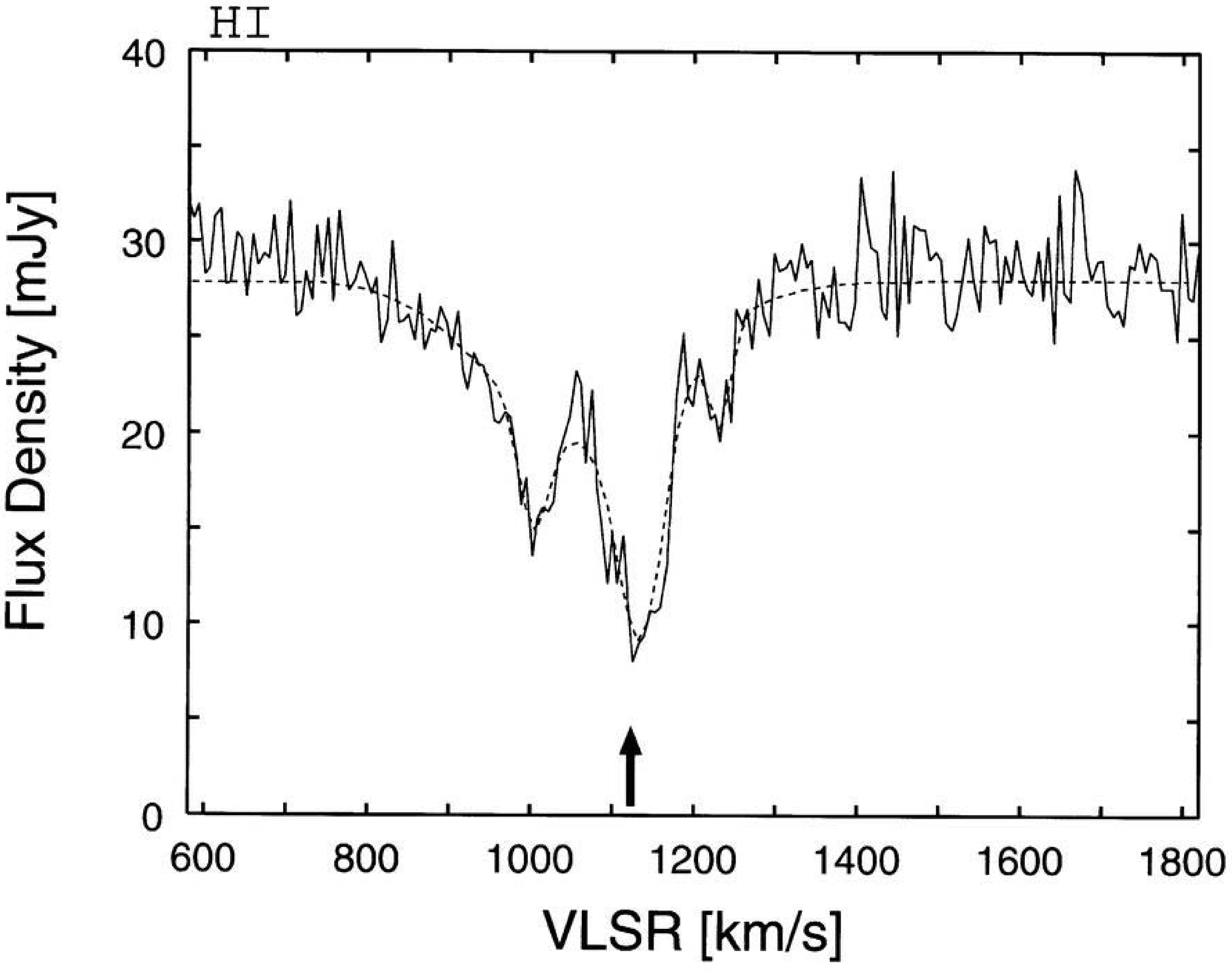
HI
Flux Density [mJy]
0
10
20
30
40
600
800
1000
1200
1400
1600
1800
VLSR [km/s]

Figure 5.2: Continuum image of NGC 3079 at 1.4 GHz with restoring resolution of 15×11 mas^2. The HPBW of the beam is shown lower right. The contour levels are (4, 8, 12, 16, 20, 24)×0.69 mJy beam^{-1}.

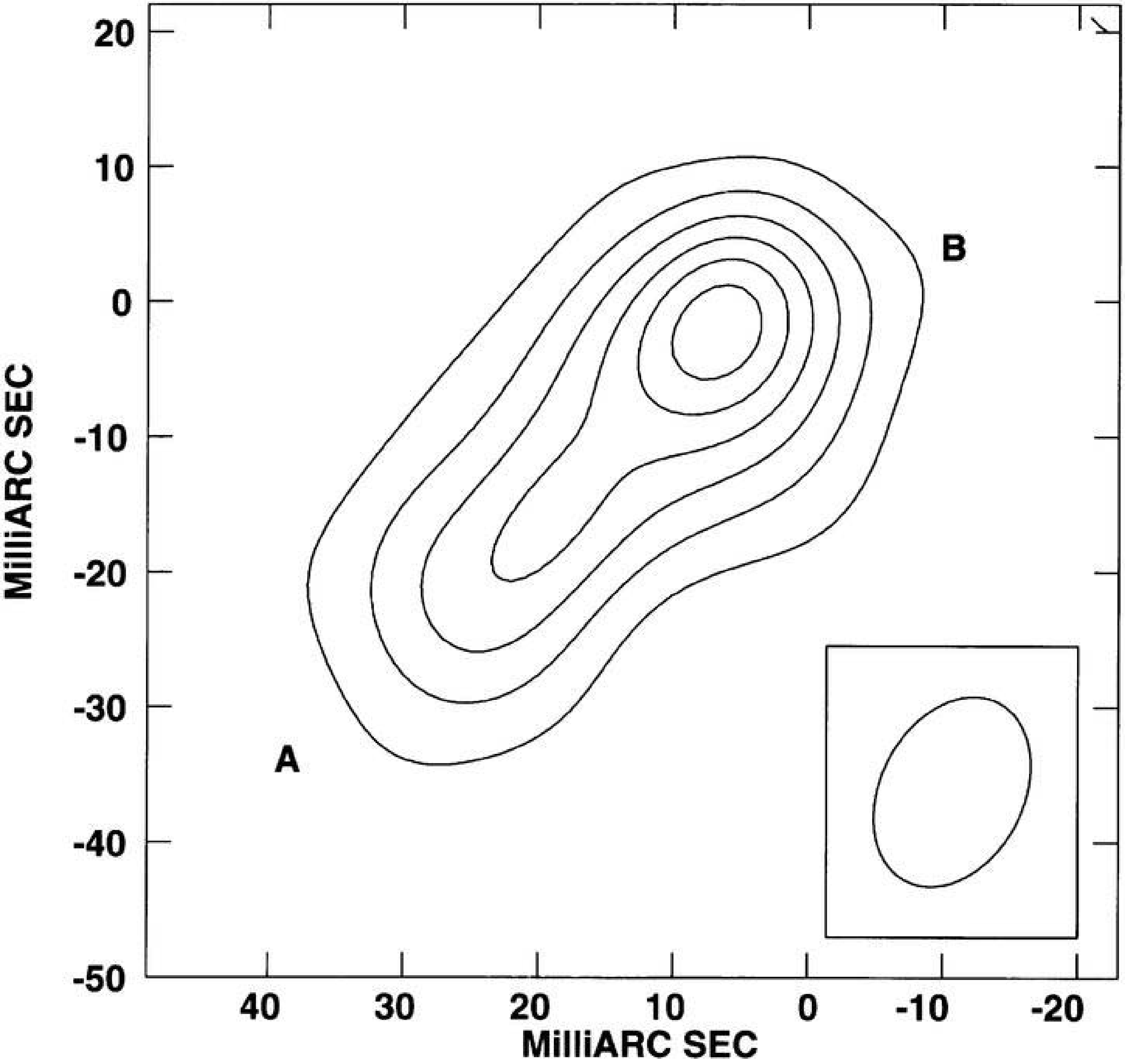

20
10
0
-10
-20
-30
-40
-50
MilliARC SEC
B
A
40
30
20
10
0
-10
-20
MilliARC SEC

Figure 5.3: Continuum-subtracted maps in each velocity channel in the nuclear region of NGC 3079. The cube shown was obtained using natural weighting and CLEANed with a restoring beam of 15×11 mas^2. Contour levels are (3, 5, 7, 9, 11, 13, 15)×1.1 mJy beam^{-1}. The velocity resolution is 52.8 km s^{-1} after smoothing in frequency.

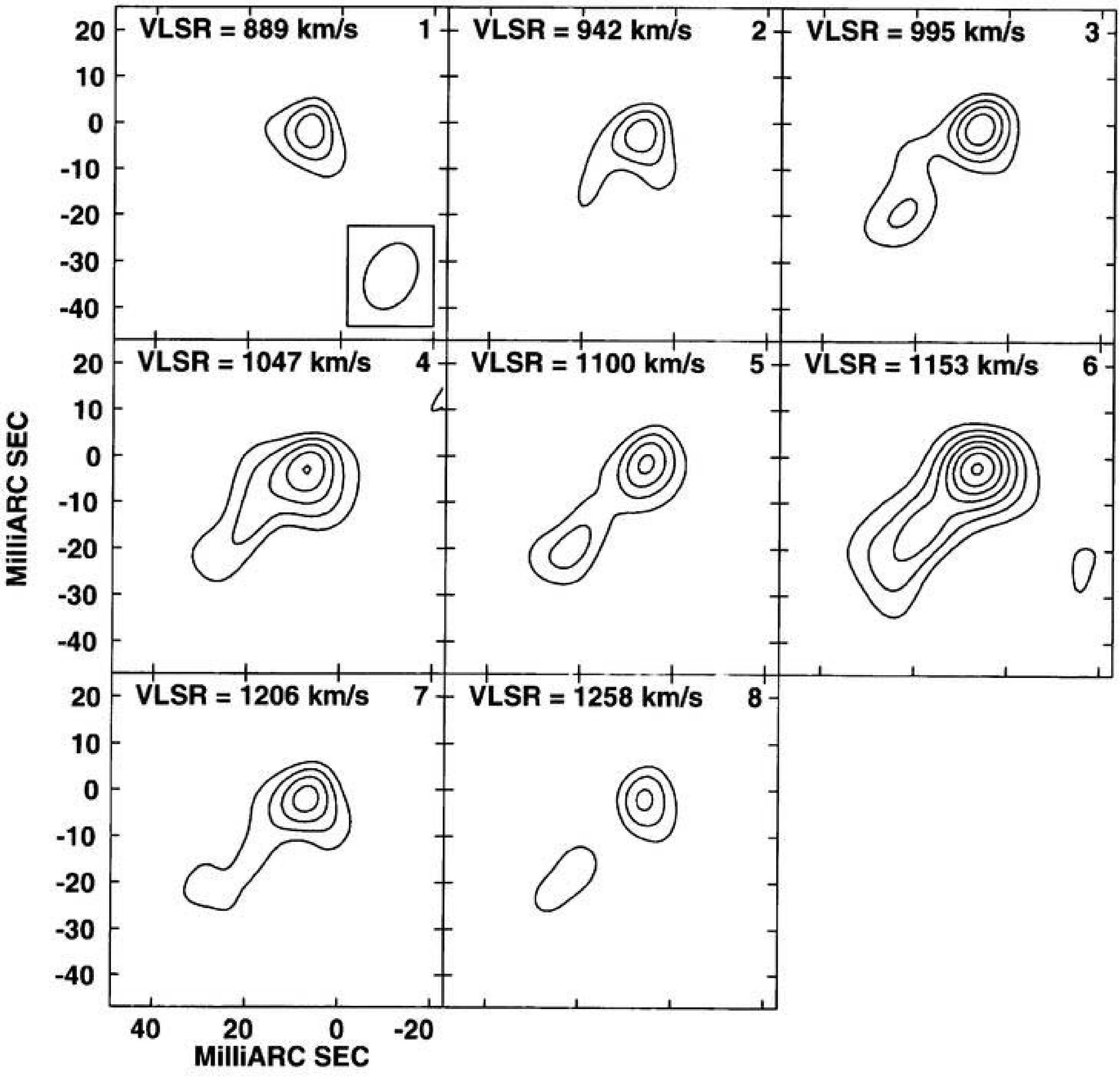
VLSR = 889 km/s
1
VLSR = 942 km/s
2
VLSR = 995 km/s
3
VLSR = 1047 km/s
4
VLSR = 1100 km/s
5
VLSR = 1153 km/s
6
VLSR = 1206 km/s
7
VLSR = 1258 km/s
8
20
10
0
-10
-20
-30
-40
MilliARC SEC
40
20
0
-20
MilliARC SEC

Figure 5.4: Position-velocity diagram of H I absorption along the A-B axis of NGC 3079. Contour levels are (5, 6, 7, 8, 10, 12, 14, 16, 18, 20) ×0.69 mJy beam^{-1}.

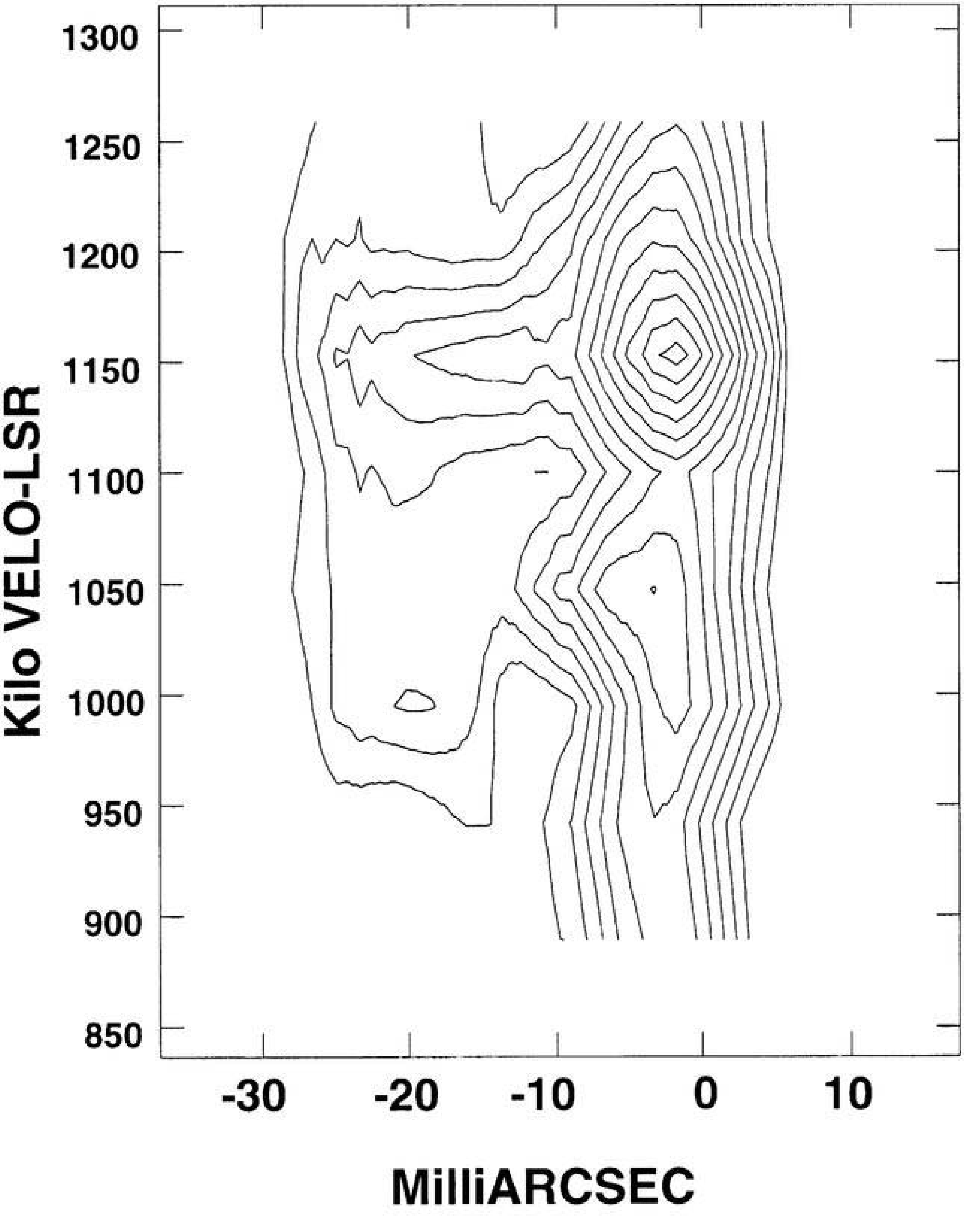
1300
1250
1200
1150
1100
1050
1000
950
900
850
Kilo VELO-LSR
-30
-20
-10
0
10
MilliARCSEC

Figure 5.5: Intensity-weighted isovelocity map of H I absorption in the nuclear region of NGC 3079 overlayed continuum contours. Color indicates the LSR Doppler velocity of the channel. The black contours show line-free continuum image of NGC 3079 at 1.4 GHz with restoring resolution of 15×11 mas^2. The HPBW of the beam is shown lower right. The contour levels are $(4, 8, 12, 16, 20, 24)\times0.69$ mJy beam^{-1}. Cross marks show the distribution of the H_2O maser features.

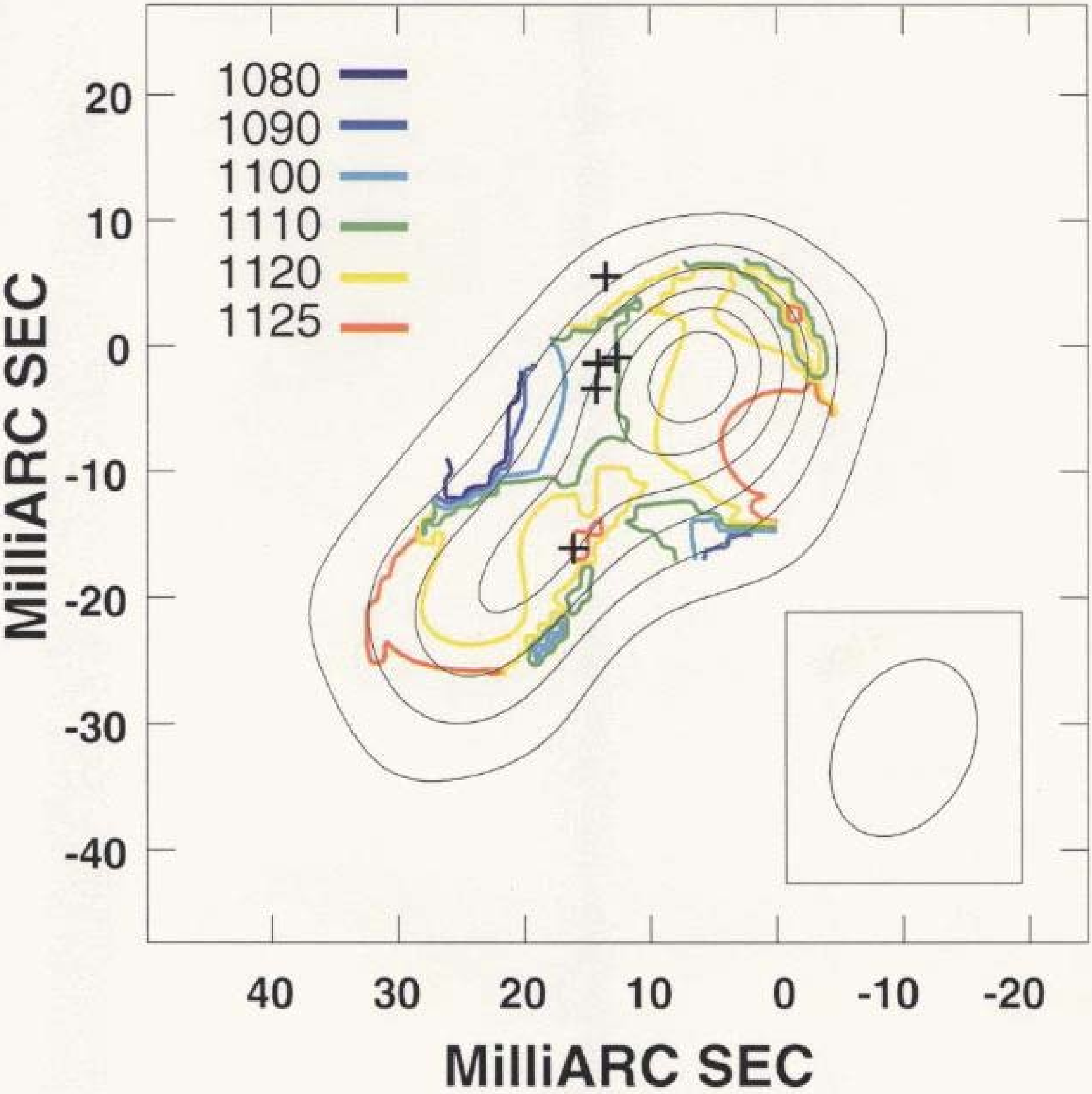
1080
1090
1100
1110
1120
1125
20
10
0
-10
-20
-30
-40
40
30
20
10
0
-10
-20
MilliARC SEC
MilliARC SEC

Figure 5.6: OH 1667 MHz absorption spectrum in the nuclear region of NGC 3079 obtained from the visibilities with spatial resolution of 13×11 mas^2. The 1665 MHz features were also detected being offset by 352 km s^{-1} from the 1667 MHz features. The velocity resolution is 5.6 km s^{-1}. The dashed lines represent the best-fitted two Gaussian components. The arrow indicates the V_{sys}.

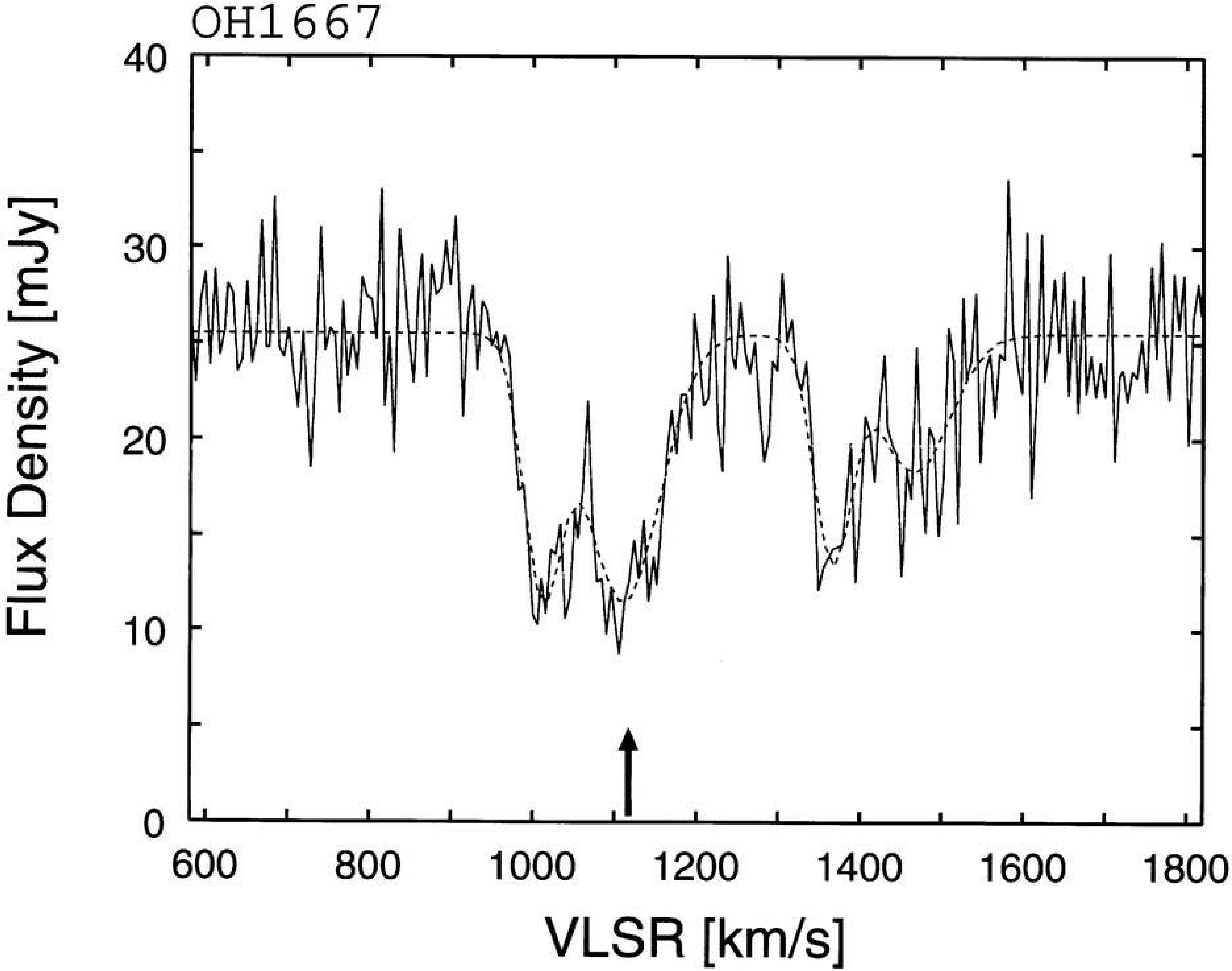
OH1667
Flux Density [mJy]
0
10
20
30
40
600
800
1000
1200
1400
1600
1800
VLSR [km/s]

Chapter 6

The Nuclear Structure

6.1 Identification of the Nucleus

In the case of NGC 4258, the dynamical center is easily defined since the rotating disk is identified by both Keplerian rotation of high-velocity maser features and the velocity shift of the systemic-velocity maser features. In the case of NGC 3079 the location of the center is less obvious, although several features, i.e., continuum radiation, H I and OH absorption, are observed in addition to maser emission.

In the following discussion, we use the term 'high-velocity feature' to refer to the maser located in the tangential part of the disk rotation, and 'systemic-velocity feature' to the maser located on the near side of the disk and on the rotation axis.

We investigate the location of the nucleus by means of the continuum structure. To explain the double continuum component of NGC 3079, three possibilities can be considered; (1) core-jet structure, (2) double lobes and (3) binary nuclei.

First, we consider the explanation of the core-jet morphology. The continuum component B at the first epoch appears to be compact and unresolved (<0.7 mas=0.05 pc) with the synthesized beam size at 22 GHz, while A and C show extended multicomponent structure, even at 8.4 GHz. The compact and extended structures of B and A+C respectively therefore also support their interpretation as a core-jet structure. The component A+C and component B show significant differences in their spectra. A nuclear system which consists of the convex spectrum exhibited by B and the steep-spectrum associated with A+C is similar to the well known core-jet morphology (e.g., Pearson and Readhead 1981, Muxlow and Garrington 1991). The non-detection of A+C at 15 and 22 GHz in first epoch is ascribed to its steep-spectrum seen between 1.4 and 8.4 GHz. In addition, the distribution of H_2O maser features did not move from B as rapidly as from A, except the displacement between the first and the second epoch. This supports the hypothesis that B is associated with the nucleus or the dynamical center of the nuclear region and that the gravity of the nucleus binds the surrounding gas. It is likely that B and A+C are a nucleus and a jet, respectively.

Secondly, we consider the possibility of parsec-scale double lobes. This explanation was presented by T98, from the convex spectra they saw in both components. The discrepancy between our spectra and those of T98 is explained by time variation. It should be noted that their spectrum came from two epoch observations. Our spectra (figure 3.4) were obtained from a simultaneous multi-frequency observation. At 5 GHz, observations in 1986 (IS88) and in 1992 (T98) showed a large decrease in the flux density of A from 12±5 to 6.0±0.5 mJy, while B varied from 12±7 to 16.8±0.4 mJy during the same period. At 8.4 GHz, observations in 1992 (T98) and ours in 1996 showed that both components have weakened over the four years. Notably, the flux density of A decreased by 87% over that period. At 22 GHz, however, such rapid decreases in the flux density of the components are not seen during four observations between 1995 and 1997 (32 months total): the one epoch of T98 and our three epoch. The decrease of the flux density of A could be understood to be due to expansion of a synchrotron radiating cloud or a change of the Doppler boosting factor of the jet, i.e., a decrease of the jet's velocity or the changing of the jet angle from the line of sight due to jet bending. Thus, we rule out the possibility of double lobes.

Finally, we consider the possibility of a binary black hole. Double continuum components in galaxies and QSOs have sometimes been interpreted as indicating the presence of a binary black hole system (e.g. Begelman et al. 1980). Such binaries are formed by galactic mergers, and shows behavior due to the precession of the spin axis of the black holes. Misalignment between the large-scale jet and small-scale jet has sometimes been explained as being due to precessing jets. It is possible to consider the two continuum components in NGC 3079 as a binary black hole, on the grounds that NGC 3079 has also misaligned jets (Hummel et al. 1983; Duric et al. 1983; IS88). However, the interpretation of A and B as a binary black hole system has not been confirmed yet. IS88 showed that the precession period of the binary black hole is 10^{4-5} times longer than the time scale for gas to flow into the outer lobes using the escape velocity and distance to the outer lobes, and precession did not account for any misalignments between parsec- and kiloparsec-scale features. Furthermore, the substructure of the component A and the existence of the component C could not been explained in the binary black hole model. It is not likely that A and B are a binary black hole system.

6.2 Neutral Hydrogen Gas Distribution

The broad velocity range, over 250 km s^{-1}, and high column density, over 10^{22} atoms cm^{-2}, of H I absorption features toward component B are consistent with the idea that the atomic gas resides in rapid orbital motion close to the nucleus. If the velocity gradient of H I absorption along the east-west direction seen across B is real, it is indicative of a rotating torus surrounding the nucleus. The rotation axis suggested by the velocity gradient is nearly parallel to the north-south direction.

The 250 km s^{-1} FWHM velocity of the gas at 1 pc implies a central mass of $\sim 1 \times 10^7$ $M_\odot$. However, a clear velocity gradient is not found toward A, and the velocity structure toward A is more complex. One possible explanation is the limited of thickness of the rotating torus. The torus is viewed possibly almost edge-on and the near side of the torus covers only B but not A. Another possible explanation is that we see the sum of a few velocity structures on A, for example, rotation torus and outflow, while we do not see a clear velocity trend along the direction of A-B axis.

The three narrow absorption features close to V_{sys}, near 1000 km s^{-1} and 1230 km s^{-1} seen on both A and B seem to be due to foreground neutral hydrogen gas outside of the parsec-scale region. Furthermore, their column densities are about $10^{19} \times T_{spin}$ atoms cm^{-2} (table 5.1), one order of magnitude lower than the broad H I absorption with peak velocity of 1060 km s^{-1}. This fact also supports the hypothesis that the narrow absorption features are associated with outside of the parsec-scale region.

Evidence of a circumnuclear torus of atomic gas has been seen in Hydra A, NGC 4151, Mkn 6 and Cygnus A (Taylor 1996; Mundel et al. 1995; Gallimore et al. 1997; Conway and Blanco 1998). Hydra A is classified as a LINER and its H I absorption associated with the core has shown a high column density (1.4×10^{22} atoms cm^{-2}). In Cygnus A, a Seyfert 2 galaxy, H I absorption feature is broad and the FWHM is over 100 km s^{-1}. These atomic gas densities are higher than these of NGC 4151 (4×10^{21} atoms cm^{-2}) and Mkn 6 (3×10^{21} atoms cm^{-2}), assuming T_{spin} =100K. The column density of the neutral hydrogen in NGC 3079 is consistent with the column densities found in Hydra A and Cygnus A.

6.3 Molecular Gas Distribution

6.3.1 Torus Around the Nucleus

The line between the first maser group and B is almost parallel to the direction of the velocity gradient of H I seen across B. If the velocity gradient is due to rotation around B, since the first and second maser groups do not exhibit a velocity drift, it is likely that they are high-velocity features of the rotation and located in the approaching side. The extended distribution of high-velocity features along the north-south axis appear to indicate thickness of the disk, i.e., not a thin disk but a torus.

On the other hand, there are several possible explanations of the maser feature at 1202 km s^{-1}. The first possible explanation is that the drifting maser feature at 1202 km s^{-1} is the systemic-velocity feature of the rotation system. If so, the line between the maser feature at 1202 km s^{-1} and B (P.A.$\sim -30°$) should then be the projected rotation axis of the rotation system. The line is nearly perpendicular to the direction of the velocity gradient of H I on B which can be regarded as the rotation plane (P.A.$\sim$60°), and agrees with the rotation axis suggested by the velocity gradient. The P-V diagram of the H_2O maser features along the direction of P.A. of $\sim 60°$ is plotted in figure 6.6. We fitted a Keplerian rotation curve, $v \propto r^{-1/2}$, rotation axis of P.A.$= -30°$, assuming that the rotation system is exactly edge-on for simplicity. The fitted Keplerian rotation curve provides some estimates about the rotation system. From the rotation curve in figure 6.6, the systemic velocity and the central binding mass is estimated to be 1177±192 km s^{-1} and $(0.4\pm1.2)\times10^7$ $M_\odot$, respectively. The location of the dynamical center of the fitted rotation using the maser features is 5.4 mas shifted from the strongest maser feature at 956 km s^{-1} to southwest along the direction of P.A. of 60°, while the value has a large error of 7.3 mas. The rotation axis is shifted 6.4 mas to the same direction from the strongest feature, and we can say it is located within the area in which the dynamical center should exist. Although the radius and velocity of the orbit of the drifting maser at 1202 km s^{-1} are unknown, we can obtain the value of the radius and the velocity of a maser with centripetal acceleration of 3.7±0.6 km s^{-1} yr^{-1}, using the rotation curve. The orbit radius and velocity of the drifting maser at 1202 km s^{-1} is estimated to be 0.07±0.1 pc and 500±20 km s^{-1}, respectively. The fit, however, does not explain the substructure of the velocity field in each maser group.

The second possible explanation of the drifting maser at 1202 km s^{-1} is that the masers are excited by the radio jet or outflow. If so, the increasing velocity drift can be understand as being due to the reducing speed of the jet or outflow. However, there is no strong evidence supporting the suggestion that the velocity drift of maser at 1202 km s^{-1} is due to the jet or outflow.

6.3.2 Possibility of A Thin Disk

We rule out a possibitily of an edge-on thin disk along the direction with P.A. of $\sim -10°$ proposed by T98 (see Chapter 1). One reason is because the position of the continuum component B is offset from this line. If NGC 3079 has a thin edge-on maser disk similar to those observed in NGC 4258 and NGC 1068, the nucleus should be located on the line of maser alignment. The other reason is because we find no systematic velocity trend along the north-south direction.

Here we discuss an edge-on thin disk along direction of P.A. ~ 60°. The velocity drift of the maser emission at 1202 km s^{-1} (see Chapter 4.1) is presumably due to centripetal acceleration. By analogy with NGC 4258, this maser spot should be located on the near side of the rotation system. Consequently, the systemic-velocity feature should be located close to the rotation axis. The rotation axis then should run through component B and the drifting maser spot at 1202 km s^{-1} (P.A. $\sim -30°$), i.e. the rotation plane should be P.A.~ 60°. The other maser features in the first and second groups without velocity drift should be 'high-velocity features'. However, it should be noted that the maser spot at 1202 km s^{-1} is offset by 1.3 pc from the nucleus, so we rule out a edge-on thin masering disk as seen in NGC 4258.

Here we discuss the inclined (not edge-on) thin disk with the rotation axis of P.A$\sim -30°$ to explain the distribution of both the first and second groups of maser features at velocity of 920–1070 km s^{-1} and the maser spot at 1202 km s^{-1}. Before discussing our results, it is helpful to describe three points of the relations of orbit radii and velocities in systemic-velocity features and high-velocity features: (1) The observed velocity of the systemic-velocity feature, $v_{\tilde{sys}}$, should indicate the radial velocity of the disk, v_{rad}, with any inclination. (2) The real orbit radius of the high-velocity maser, r_{high}, should be the spatial separation between the maser and the nucleus, ΔP_{high}, with any inclination. On the other hand, the real orbit velocity of the high-velocity maser v_{high}, should be a function of inclination and difference between observed velocity of the maser,$v_{\tilde{high}}$ and v_{rad}. (3) The real orbit radius of the systemic-velocity maser, r_{sys} should be a function of inclination, i, and spatial separation between the maser and the nucleus, ΔP_{sys}. The real centripetal acceleration, a_{sys}, should be also a function of inclination, i, and the observed centripetal acceleration of the systemic-velocity maser, $a_{\tilde{sys}}$. The real orbit velocity of the systemic-velocity maser, v_{sys}, can be estimated using the relation $v = \sqrt{a \times r}$, i.e.,

$$\begin{aligned}
v_{rad} &= v_{\tilde{sys}} && (6.1)\\
r_{high} &= \Delta P_{high} && (6.2)\\
v_{high} &= \frac{v_{\tilde{high}} - v_{rad}}{\sin i} && (6.3)\\
r_{sys} &= \frac{\Delta P_{sys}}{\cos i} && (6.4)\\
a_{sys} &= a_{\tilde{sys}} && (6.5)\\
v_{sys} &= \sqrt{a_{sys} \times r_{sys}}. && (6.6)
\end{aligned}$$

If the maser feature at 1202 km s^{-1} is the systemic-velocity feature, the radial velocity of the disk could be 1202 km s^{-1}. Based on this assumption, we can consider the orbit radius and velocity of the high-velocity feature and systemic-velocity feature. If the first and second groups of maser features at velocities of 920–1070 km s^{-1} are the high-velocity masers, we can say that the orbit radius of the strongest maser feature at 956 km s^{-1} is $r_{high} = 0.5$ pc and the real rotation velocity of the strongest maser feature is $v_{high} = 250/\sin i$ km s^{-1}. On the other hand, the spatial separation between the systemic-velocity feature and the nucleus, 1.3 pc, should be the projected orbit radius of the maser itself depending on the inclination of the disk. We can say that the real orbit radius of the maser is $r_{sys} = 1.3/\cos i$ pc, where i is inclination of the disk (0° for face on). The observed velocity drift of the systemic feature is also affected by the inclination of disk. The real centripetal acceleration of the systemic feature would be $a_{sys} = (3.7 \pm 0.6)/\sin i$ km s^{-1} yr^{-1}, so we can estimate it to be v_{sys} $\sim 2100/\sqrt{\sin i \cos i}$ at the orbit radius of $1.3/\cos i$. However, if it is a Keplerian rotating disk as seen in NGC 4258 the value of the rotation velocity is too large and the relation of $v \propto r^{-1/2}$ can not be kept between the systemic-velocity feature and the high-velocity feature. Further, high velocity maser features at greater than 2100 km s^{-1} have not been observed yet. It is unlikely that the maser feature at 1202 km s^{-1} is rotating with an orbit radius of $1.3/\cos i$ around the nucleus. Thus, the thin molecular disk model around B is not likely to be correct.

6.3.3 Emission In and Around the Jet

Although the overall velocity trend is not clearly seen along its jet direction, the maser features close to the brightest feature imply the velocity trend along its jet direction (figure 4.9). This is similar to the maser features of NGC 1052 (Claussen et al. 1998) which have a velocity gradient along the jet direction. The maser features of NGC 3079 are, however, offset from the line between the nucleus and the jet. Therefore, we rule out the H_2O maser emission lying in or around the radio jet.

6.4 Jet Direction

We did not detect a counter-jet in the parsec-scale region, while NGC 3079 has two-sided radio lobes on the kiloparsec scale. One possible explanation of the one-sided jet is that the jet components are moving relativistically oriented away from the plane of the sky. A significant boosting factor makes the approaching jet brighter and the receding jet fainter. This could easily explain the one-sided jet. It is acceptable to consider the component A as an approaching jet, because the lobes in the kiloparsec-scale show asymmetric polarization (Duric et al 1983). If the approaching and receding jets are ejected with a velocity v in a direction θ with respect to the line-of-sight, the ratio of the observed flux densities of the approaching and receding jets at a given frequency is given by

$$\frac{S_{\rm app}}{S_{\rm rec}} = \left(\frac{1+\beta\cos\theta}{1-\beta\cos\theta}\right)^{3-\alpha} \tag{6.7}$$

where $S_{\rm app}$ and $S_{\rm rec}$ are the flux density of the approaching and receding jet, respectively, β is the fraction of the true jet velocity of the speed of light, v/c, and α is the spectral index (e.g., Ryle and Longair 1967; Begelman et al. 1984). At the second epoch in March 1997, the component A was detected with a flux density of 3.3 mJy. If there is a receding jet, its flux density would be less than 1 mJy. Using the spectral index of component A, -0.36, we can obtain a relation of $\beta\cos\theta > 0.18$. The apparent β of the jet can be written as

$$\beta_{\rm app} = \frac{\beta\sin\theta}{1-\beta\cos\theta} \tag{6.8}$$

(e.g., Rees, 1967; Blandford et al. 1977; Kraus, 1986). The apparent velocity of component A is 0.21c, so we can obtain a relation of $\beta = 0.21/(\sin\theta + 0.21\cos\theta)$. The two relations yield limits of $0.24 < \beta < 1$ and $\theta < 44°$.

Some sources display evidence for another interpretation for invisible counter-jet, free-free absorption (FFA). NGC 3079, however, shows no clear evidence of high dense ionized gas surrounding the nucleus, as described in the previous section. FFA seems to be unlikely to be the reason for the lack of detection of a counter-jet for NGC 3079.

We cannot say that two-sided jet is ejected either with same direction or simultaneously. The possibility of intrinsically alternating-side ejection of radio jets cannot be ignored, such as the so-called "flip-flop jet" (e.g., Rudinick and Edgar 1984). However, it is not clear what mechanism causes the flip-flop jets, and so we do not consider this model any further.

To explain the structural and positional change of B between the first and the second epoch, it is possible to consider the hypothesis that a new jet component is being ejected from the nucleus. The changed structure of B is elongated to the east-west and the motion of B is along the direction of P.A ~ 230°, i.e, neither direction is parallel to the A-B. In some radio sources new component are ejected along direction which differ from that of previously ejected components. 3C273 is a good example (Krichbaum et al. 1990). We cannot deny such jet ejection in NGC 3079, however further investigation is required. In order to examine this hypothesis, it is neccesary to continue the monitoring program.

6.5 An Overview of the Nuclear Region

6.5.1 Dynamics of Nuclear Region

In the previous sections we discussed possible explanations of the continuum structure and gas distributions. We can then consider the parsec-scale structure in the nuclear region to explain all results.

The most probable explanation for the velocity gradient of H I across B is an atomic gas torus surrounding the nucleus with the rotation plane along the east-west axis as shown in figure 6.6. The torus should be nearly viewed edge-on and the near side of the torus covers B. The rotation axis of the torus should be nearly parallel to the north-south direction.

It is possible that the H_2O maser features lie in the same rotation system as H I gas. If the velocity drift of the maser feature at 1202 km s^{-1} is due to centripetal acceleration, the drifting feature should be the 'systemic-velocity feature' located in the near side of the torus, and the P.A. of the rotation axis should be $\sim -30°$. The direction of the rotation axis is acceptable for a torus with the rotation plane along the east-west axis. The maser group around 920–1070 km s^{-1} without velocity drift would then be the 'high-velocity maser features'. They are located on the approaching side of the torus. The thickness of the torus should be at least one parsec because the near side of the torus should cover not only B but also the maser at 1202 km s^{-1}.

The radial velocity of the torus is not clear. The velocity can be estimated using two pieces of information. One is the central velocity of the broad H I absorption associated with B, and the other is the velocity of the drifting maser. They are 1060 km s^{-1} and 1202 km s^{-1}, respectively. Possible explanations for the difference are that either the H_2O maser feature is moving toward the nucleus due to inflow, or the H I gas is coming out from the nucleus due to outflow, or a combination of inflow and outflow is occuring. The proper motion of H_2O maser features for the projected velocity of 100 km s^{-1} is 1μas per year.

It is supposed that the rotating disk is perpendicular to the direction of the jet from the nucleus like NGC 4258. However, the position angle of the rotation axis of the torus differs from the position angle of the core-jet structure by $\sim 30°$ in NGC 3079. In this case, the rotation plane of the torus is not perpendicular to the jet. Another smaller disk which is perpendicular to the jet direction may exist inside the torus, closer to the nucleus. It has been recently shown that broad emission-line regions (BLRs) are not always coplanar with respect to accretion disks in Type-1 Seyfert galaxies (Nishiura et al. 1998). Typical radii of BLRs are ~ 0.01 pc (e.g. Peterson 1993), which is a smaller scale than the torus of NGC 3079. Therefore, the rotation plane of a torus of this scale need not be perpendicular to the jet.

6.5.2 Parsec-Scale Dynamics vs. Kiloparsec-Scale Dynamics

The question of why the nuclear torus has a different rotation plane to the galactic scale region of NGC 3079 is an interesting problem. Such a significant angular difference between the rotation axis of the host galaxy and that of the nuclear disk shown with H_2O maser emission has been seen in NGC 4258 and NGC 1068 (e.g., Inoue 1997).

One of the possible reasons is that inner and outer galaxy have had a strong disturbance. Such disturbance might be caused by merging of two galaxies. However, no evidence of a merger in the case of NGC 3079 has been presented. VLA H I observations by Irwin et al. (1987) found that one of NGC 3079's companions, NGC 3073, exhibits an elongated H I tail which is aligned with the nucleus of NGC 3079. In the same way, interaction with NGC 3079's companions may give some kind of dynamical effect to NGC 3079. Or, this might be due to the asymmetrical potential by nuclear bar structure. Thus, detailed studies of the nuclear dynamics can provide a key to investigate the evolution of AGN and the interaction between galaxies.

6.6 Comparison with Other H_2O Megamasers

The structure of the H_2O maser emission region in NGC 3079 does not agree with the edge-on thin disk model provided by NGC 4258 for two reasons. The first is the distribution of the maser features. The H_2O maser emission in NGC 3079 shows clustering into two groups, and the velocity gradients of the maser emission in each group are different to each other. The second is the fact that there is no positional coincidence between the maser features and the continuum components, while the luminosity of the maser emission is more powerful than that of NGC 4258. These results strongly suggest that the emitting mechanism of H_2O maser of NGC 3079 is different from that in NGC 4258, NGC 1068 and NGC 4945. The second described above also differs the H_2O emission of NGC 1052 (see section 6.4.2). Thus, the physical situation of the H_2O maser emission in NGC 3079 seems to be quite different from those of other megamasers. The distribution of maser features in the megamasers are summarized in table 6.1.

Table 6.1: Interpretation of parsec-scale nuclear structure of H_2O megamasers

Source	Thin disk of maser ?	Keplerian rotation ?	Velocity drift ?	Torus of other gas ?
NGC 1052	N	N		
NGC 1068	Y	N	N	Y
NGC 2639			Y	Y
NGC 4258	Y	Y	Y	
NGC 4945	Y	N	N	
NGC 5793				Y[*]
NGC 3079	N	N	Y	Y

[*] Hagiwara 1999.

Figure 6.1: Position-velocity diagram of the H_2O maser features along the direction of P.A. of 60°, the rotation plane of the torus. For simplicity, we assume the torus is exactly edge-on. The solid curve is a best-fitted Keplerian rotation curve for $v \propto r^{-1/2}$. The dashed line indicates an orbit with the centripetal acceleration of 3.7 km s^{-1} yr^{-1}. The top-right full circle is the drifting maser feature at 1202 km s^{-1}.

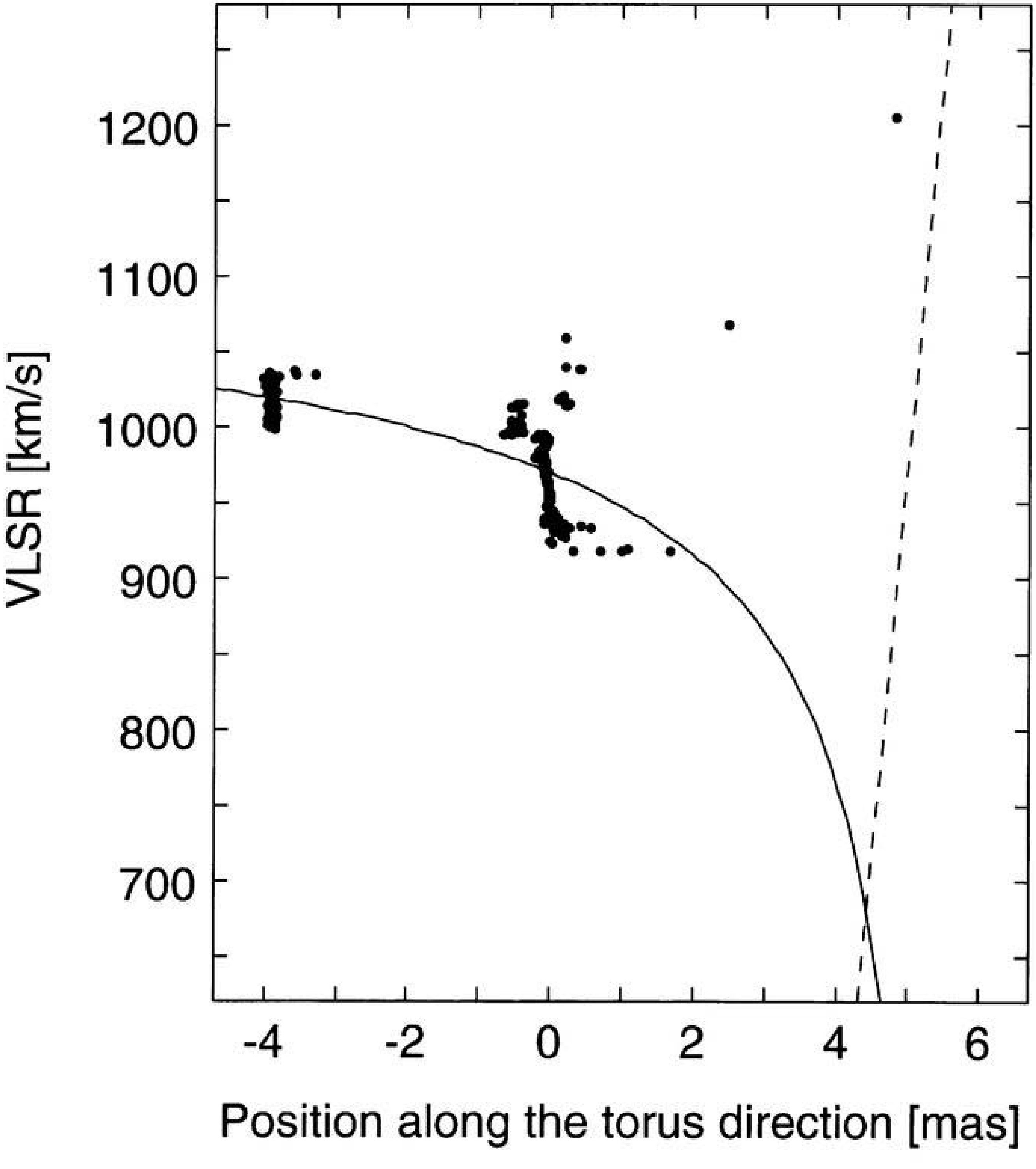
1200
1100
1000
900
800
700
VLSR [km/s]
-4
-2
0
2
4
6
Position along the torus direction [mas]

Figure 6.2: Possible model of the parsec-scale nuclear structure of NGC 3079. Component B is the nucleus and the dynamic center of the rotating disk or torus with H_2O maser and neutral hydrogen. H_2O masers at 920–1070 km s^{-1} are high-velocity features and the maser at 1202 km s^{-1} is located near the midpoint of A and B, nearly on the plane which contains the rotation axis and the observer.

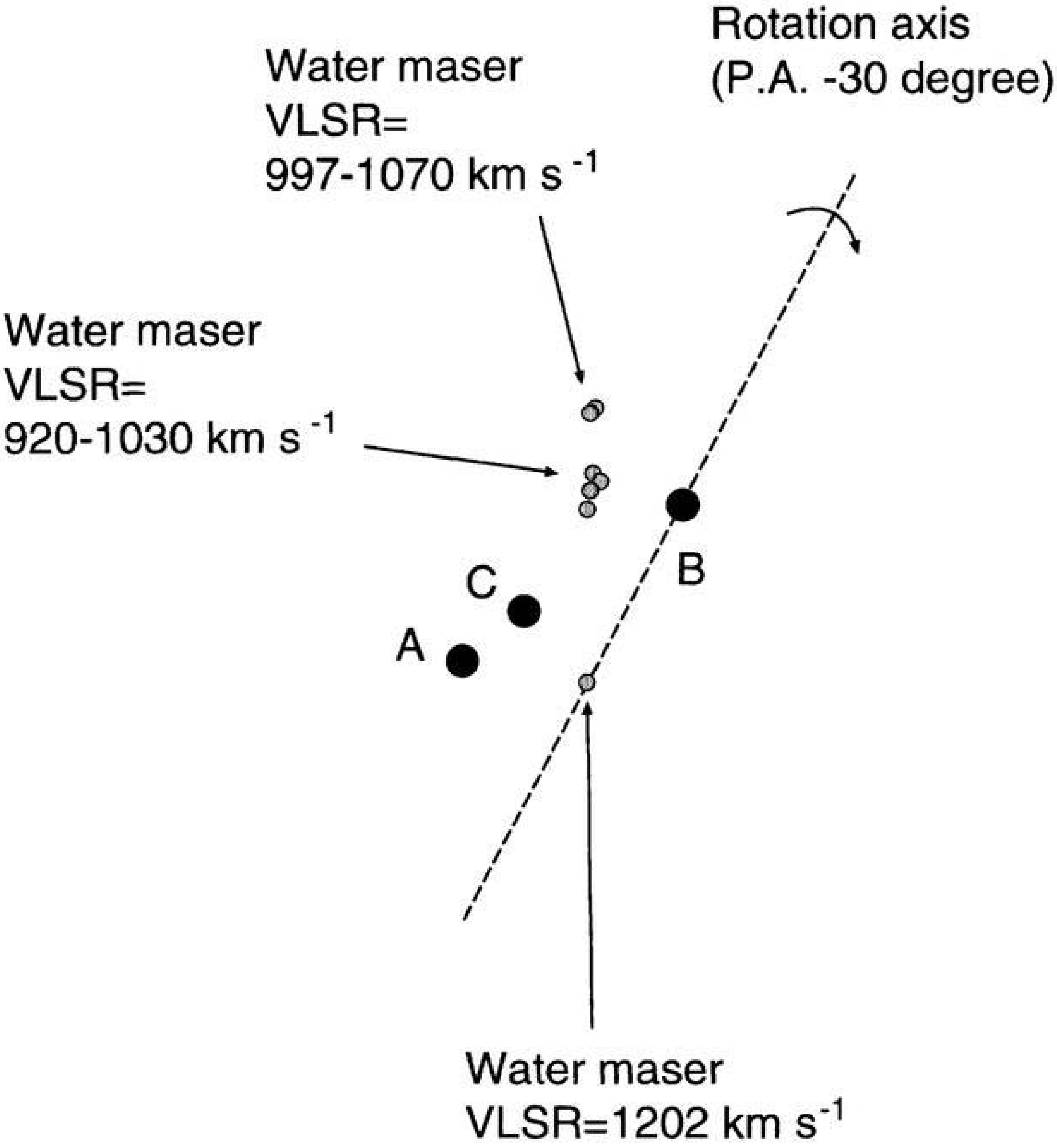
Rotation axis
(P.A. -30 degree)
Water maser
VLSR=
997-1070 km s -1
Water maser
VLSR=
920-1030 km s -1
C
B
A
Water maser
VLSR=1202 km s-1

Chapter 7

Conclusions

7.1 The Nuclear Structure of NGC 3079

We conducted a multi-frequency monitoring program of NGC 3079 with a Global VLBI Network including the VLBA, the VLA, EB and GB. Frequencies of 1.4, 1.6, 8.4, 15 and 22 GHz were used to observe continuum emission, H_2O maser emission and H I and OH absorption in the parsec-scale nuclear region of NGC 3079.

We identify the continuum component B as the nucleus. The keys are (1) its convex continuum spectrum, (2) its compact structure, (3) its less rapid positional change relative to the maser sources. (4) the broad H I absorption seen only on B, and (5) the velocity gradient of H I seen only on B.

The velocity gradient of H I is well explained as rotation around B. The velocity drift of maser feature at 1202 km s^{-1} can be explained as centripetal acceleration, and the drifting maser is located close to the rotation axis. From the velocity gradient and the velocity drift, we define the direction of the rotation axis.

The axis of the rotation around the nucleus differs from those of the kiloparsec-scale galactic structure by 100°. The first and second maser groups without velocity drift would be "high-velocity masers" of the approaching side of the rotation. The extended distribution of these maser groups along the north-south direction seems to indicate a thick torus rather than a thin disk.

The three narrow (FWHM < 100 km s^{-1}) H I absorption features seen on both A and B can be explained as coming from foreground H I gas outside the parsec-scale region. Their column densities are about one order lower than the broad H I absorption.

We propose a different structure for the H_2O maser in NGC 3079 from those seen in other H_2O megamasers. The H_2O maser features come from a torus surrounding the nucleus. The origin and amplification mechanism of the maser emission in NGC 3079 is not clear.

The VLBI results of megamaser sources including this work also suggest that a nuclear system with a different rotation axis from that of whole galactic scale is a general nature of AGN, and may raise some interesting questions regarding the evolution of AGN and galactic dynamics.

7.2 Future Works

This experiment with H_2O maser and continuum emissions, H I and OH absorptions has led us to view the nuclear structure from many angles. However, we cannot say that the nuclear structure NGC 3079 has been completely clarified. NGC 3079 has some time-variability, so we are continuing our program of VLBI observations of NGC 3079 to examine our explanations. The last observations were carried out in November 1998. The detection of a new jet component from the nucleus would allow us to get a lot of knowledge about the nuclear region; for example, the exact location of the nucleus, and the relation between the maser emission and the radio jet. The proper motions of the maser features will allow us to examine whether the maser emission is associated with a rotation system around B, although it would take about 10 years to detect the proper motion with VLBA resolution.

It would be interesting to observe not only H_2O maser emission but H I absorption in other H_2O megamasers to determine the velocity structure of the nuclear region. We are planning a VLBI observation of H I absorption towards NGC 1052, one of H_2O megamasers using the EVN. Furthermore, we are making survey observations of H_2O megamasers, searching for H I absorption lines, with the VLA. This survey is one step of H I observations towards H_2O megamasers. The first survey observations were done on November 11 of 1998. These observations should also help us to compare the nuclear structure of NGC 3079 with those of other H_2O megamasers. We strongly believe that these H_2O megamasers with continuum emission and absorption line features will provide insights into the inner regions of AGN.

Bibliography

[1] Antonucci, R., 1993, *ARAA*, **31**, 473.

[2] Baan, W. A. and Haschick, A., 1996, *ApJ*, **473**, 269.

[3] Baan, W. A. and Irwin, J. A., 1995, *ApJ*, **446**, 602.

[4] Batchelor, R. A., Jauncey, D. A. and Whiteoak, J. B. 1982, *Mon.Not.R.Astron.Soc.*, **200**, 19.

[5] Begelman, M. C., Blandford, R. D. and Rees, M .J. 1980, *Nature*, **287**, 307.

[6] Begelman, M. C., Blandford, R. D. and Rees, M .J. 1984, *Rev. Mod. Phys.*, **56**, 255.

[7] Blandford, R. D., McKee, C. F. and Rees, M. J. 1977, *Nature*, **267**, 19.

[8] Braatz, J. A., Wilson, A. S. and Henkel, C., 1994, *ApJ*, **437**, L99.

[9] Braatz, J. A., Wilson, A. S. and Henkel, C., 1996a, *Vistas in Astronomy*, **40**, 83.

[10] Braatz, J. A., Wilson, A. S. and Henkel, C., 1996b, *ApJS*, **106**, 51.

[11] Braatz, J. A., Wilson, A. S. and Henkel, C., 1997, *ApJS*, **110**, 321.

[12] Braine, J., Guélin, M., Dumke, M, Brouillet, N., Herpin, F. and Wielebinski, R. 1997, *A&Ap*, **326**, 963.

[13] Churchwell, E., Witzel, A., Huchtmeier, W., Pauliny-Toth, I., Roland, J. and Sieber, W. 1977, *A&Ap*, **54**, 969.

[14] Claussen, M. J., Heiligman, G. M. and Lo, K.-Y., 1984, *Nature*, **310**, 298.

[15] Claussen, M. J. and Lo, K.-Y., 1986, *ApJ*, **308**, 592.

[16] Claussen, M. J., Diamond, P. J., Braatz, J. A., Wilson, A. S. and Henkel, C. 1998, *ApJ*, **500**, L129.

[17] Conway, J. E., 1998, in *Radio Emission from Galactic and Extragalactic Compact Sources*, ed. J. A. Zensus, G. B. Taylor, J. M. Wrobel, IAU colloquium 164, Astronomical Society of the Pacific Conference Series vol. 144, p.231.

[18] Dahlem, M., Weaver, K. A. and Heckman, T. M., 1998, *ApJS*, **118**, 401.

[19] de Bruyn, A. G., 1977, *A&Ap*, **96**, 164.

[20] de Vaucouleurs, G., de Vaucouleurs, A., Corwin, H. G., Jr., Buta, R. J., Paturel, G. and Fouqué, P. 1991, Third Reference Catalogue of Bright Galaxies (New York: Springer)

[21] Dickey, J. M., Crovisier, J. and Kazès, I. 1981, *A&Ap*, **98**, 271.

[22] dos Santos, P. M. and Lèpine, J. R. D. 1979, *Nature*, **278**, 34.

[23] Duric, N., Seaquist, E. R., Crane, P. C., Bignell, R. C. and Davies, L. E., 1983, *ApJ*, **273**, L11.

[24] Duric, N. and Seaquist, E. R., 1988, *ApJ*, **326**, 574.

[25] Fabbiano, G., Feighlson, E. and Zamorani, G., 1982, *ApJ*, **256**, 397.

[26] Fabbiano, G., Kim, G.-W. and Trinchieri, G., 1992, *ApJS*, **80**, 531.

[27] Ford, H. C., Dahari O., Jacoby G. H., Crane P. C. and Ciardulo R. 1986, *ApJ*, **311**, L7.

[28] Filippenko, A. V. and Sargent W. L. W. 1985, *ApJS*, **57**, 503.

[29] Filippenko, A. V. Sargent W. L. W. 1992, *AJ*, **103**, 28.

[30] Gallimore, J. F., Baum, S. A., O'Dea, C. P., Brinks, E. and Pedlar, A. 1994, *ApJ*, **422** L13.

[31] Gallimore, J. F., Baum, S. A., O'Dea, C. P., Brinks, E. and Pedlar, A. 1996, *ApJ*,**462** 740.

[32] Gallimore, J. F., Baum, S. A. and O'Dea, C. P. 1997, *Nature*, **388**, 852.

[33] Gallimore, J. F., Holloway, A. J., Pedlar, A. and Mundell, C. G., 1998, *A&Ap*, **333**, 13.

[34] Greenhill, L. J. 1992, in *Astrophysical Masers*, ed. A. W. Clegg and G. E. Nedoluha., Lecture Notes in Physics vol.412, p.87.

[35] Greenhill, L. J., Henkel, C., Becker, R., Wilson, T. L. and Wouterloot J. G. A. 1995, *A&Ap*, **304**, 21.

[36] Greenhill, L. J., Moran, J. M. and Herrnstein, J. R. 1997a, *ApJ*, **481**, L23.

[37] Greenhill, L. J., Herrnstein, J. R., Moran, J. M., Menten, K. M. and Velusamy, T. 1997b, *ApJ*, **486**, L15.

[38] Greenhill, L. J. 1998, in *Radio Emission from Galactic and Extragalactic Compact Sources*, ed. J. A. Zensus, G. B. Taylor, J. M. Wrobel, IAU colloquium 164, Astronomical Society of the Pacific Conference Series vol. 144, p.221.

[39] Hagiwara, Y., Kohno, K., Kawabe, R. and Nakai, N. 1997, *PASJ*, **49**, 171.

[40] Hagiwara, Y. 1999, Ph.D. thesis, The Graduated University for Advanced Studies.

[41] Haschick, A. D. and Baan, W. A. 1985, Nature, **314**, 144.

[42] Haschick, A. D., Baan, W. A., Schneps, M. H., Reid, M. J., Moran J. M. and Güsten, R., 1990, *ApJ*, **356**, 149.

[43] Haschick, A. D., Baan, W. A. and Peng, E. W. 1994, *ApJ*, **437**, L35.

[44] Hawarden, T. G., Israel, F. P., Geballe, T. R. and Wade, R., 1995, *Mon.Not.R.Astron.Soc.*, **276**, 1197.

[45] Henkel, C., Güsten, R., Downes, D., Thum, C., Wilson, T. L. and Biermann, P. 1984, *A&Ap*, **141**, L1.

[46] Heckman, T. M. 1980, *A$Ap*, **87**, 152.

[47] Heckman, T. M., Armus, L. and Miley, G. K. 1990, *ApJS*, **74**, 833.

[48] Herrnstein, J. R., Greenhill, L. J. and Moran, J. M. 1996, *ApJ*, **468**, L17.

[49] Herrnstein, J. R., Moran, J. M., Greenhill, L. J., Diamond, P. J., Miyoshi, M., Nakai, N. and Inoue, M. 1997, *ApJ*, **475**, L23.

[50] Ho, L. C., Filippenko, A. V. and Sargent, W. L. 1993, *ApJ*, **437**, L35.

[51] Humason, M. L., Mayall, N. U. and Sandage, A. R. 1956, *AJ*, **61**, 97.

[52] Hummel, E., van Gorkom, J. H. and Kotanyi, C. G. 1983, *ApJ*, **262**, L5.

[53] Inoue, M. 1997, in proceeding of *The Eighth Marcel Grossmann Meeting* held in Givat Ram Campus of The Hebrew University, Jerusalem. in press.

[54] Irwin, J. A., Seaquist, E. B., Taylor, A. R. and Duric, N. 1987, *ApJ.*, **313**, L91.

[55] Irwin, J. A. and Seaquist, E. B. 1988, *ApJ.*, **335**, 658. (IS88)

[56] Irwin, J. A. and Seaquist, E. B. 1991, *ApJ.*, **371**, 111.

[57] Irwin, J. A. and Sofue, Y. 1992, *ApJ*, **396**, L75.

[58] Iyomoto, N., Makishima, K., Tashiro, M., Inoue, S., Kaneda, H., Matsumoto, Y. and Mizuno, T. 1998, *ApJ*, **503**, 311.

[59] Iwasasa, K., Koyama, K., Awaki, H., Kunieda, H., Makishima, K., Tsuri, T., Ohashi, T. and Nakai, N. 1993, *ApJ*, **409**, 155.

[60] Keel, W. C., 1984, *ApJ*, **282**, 75.

[61] Kellermann, K. I. and Thompson, A. R., 1985, *Science*, **229**, 123.

[62] Koekemoer, A. M., Henkel, C., Greenhill, L. J., Dey, A., Van Breugel, W., Codella, C. and Antonucci, R. 1995, *Nature*, **378**, 697.

[63] Koyama, K., Inoue, H., Tanaka, Y., Awaki, H., Takano, S., Ohashi, T. and Matsuoka, M., 1989, *PASJ*, **41**, 731.

[64] Kraus, J. D., 1986, *'Radio Astronomy'* 2nd edition, Cygnus-Quasar Books, p10-28.

[65] Krichbaum, T. P., Booth, R. S., Kus, A. J., Rönnäng, B. O., Witzel, A., Graham, D. A., Pauliny-Toth, I. I. K., Quirrenbach, A., Hummel, C. A.; Alberdi, A., Zensus J. A., Johnston, K. J., Spencer, J. H., Rogers, A. E. E., Lawrence, C. R., Readhead, A. C. S., Hirabayashi, H., Inoue, M., Morimoto, M., Dhawan, V., Bartel, N., Shapiro, I. I., Burke, B. F. and Marcaide, J. M. 1990, *A&Ap*, **237**, 3.

[66] Makishima, K, Fujimoto, R., Ishisaki, Y., Kii, T., Loewenstein, M., Mushotzky, R., Serlemitsos, P., Sonobe T., Tashiro, T. and Yaqoob, T. 1994, *PASJ*, **46**, L77.

[67] Matt, G. Fiore, F., Perola, G. C., Piro, L., Fink, H. H., Grandi, P., Matsuoka, M., Oliva, E. and Salvati, M. 1996, *MNRAS*, **281**, L69,

[68] Miyoshi, M., Moran, J. M., Herrnstein, J. R., Greenhill, L. J., Nakai, N., Diamond, P. J. and Inoue, M. 1995, *Nature*, **373**, 771.

[69] Moorwood, A. F. and Glass, I. S., 1984, *A&Ap*, **135**, 281.

[70] Mundell, C. G., Pedlar, A., Baum, S. A., O'Dea, C. P., Gallimore, J. F. and Brinks, E., 1995, *Mon.Not.R.Astron.Soc.*, **272**, 355.

[71] Mushotzky, R. F., Done, C. and Pounds, K. A. 1993, *ARAA*, **31**, 717.

[72] Muxlow, T. W. B. and Garrington S. T. 1991, in *Beams and Jets in Astrophysics*, ed. Hughes, P. A., (Cambridge Astrophysics Series vol. 19), p.52.

[73] Nakai, N., Inoue, M. and Miyoshi, M. 1993, *Nature*, **361**, 45.

[74] Nakai, N., Inoue, M., Miyazawa, K., Miyoshi, M. and Hall, P. 1995, *PASJ*, **47**, 771.

[75] Nakai, N. 1996, in *Cosmological Constant and the Evolution of the Universe*, ed. Sato, K., Suginohara, T., Sugiyama, N., (Universal Academy press, Inc, Tokyo), P.113.

[76] Napier, P. J., Bagri, D. S., Clark, B. G., Rogers, A. E. E., Romney, J. D., Thompson, A. R. and Walker, R. C., 1994, *Proc. IEEE*, **82**, 5.

[77] Napier, P. J., Thompson, A. R. and Ekers, R. D., 1983, *Proc. IEEE*, **71**, 1295.

[78] Neufeld, D. A., Maloney, P. R. and Conger, S. 1994, *ApJ*, **436**, L127.

[79] Neufeld, D. A. and Maloney, P. R. 1995, *ApJ*, **447**, L17.

[80] Nishiura, S., Murayama, T. and Taniguchi, Y. 1998, *PASJ*, **50**, 31.

[81] Pearson, T. J. and Readhead, A. C. S. 1981. *ApJ*, **248**, 61.

[82] Peterson B. M. 1993, *PASP*, **105**, 247.

[83] Pedlar, A., Mudell, C. G., Gallimore, J. F., Baum, S. A. and O'Dea, C. P. 1996. *Vistas Astron.*, **40**, 91.

[84] Pietsch, W., Trinchieri, G. and Vogler, A., 1998, *A&Ap*, **340**, 351.

[85] Read, A. M., Ponman, T. J. and Strickland, D. K., 1997, *Mon.Not.R.Astron.Soc.*, **286**, 626.

[86] Rees, M. J. 1967, *MNRAS*, **136**, 123.

[87] Roberts, M. S., 1968, *ApJ*, **151**, 117.

[88] Rudnick L. and Edgar, B. K. 1984, *ApJ*, **279**, 74.

[89] Ryle, M. and Longair, M. S. 1967, *MNRAS*, **136**, 123.

[90] Satoh, S., Inoue, M., Nakai, N., Shibata, K. M., Kameno, S., Migenes, V. and Diamond, P. J., 1998, in *Radio Emission from Galactic and Extragalactic Compact Sources*, ed. J. A. Zensus, G. B. Taylor, J. M. Wrobel, IAU colloquium 164, Astronomical Society of the Pacific Conference Series vol. 144, p.219.

[91] Seaquist, E. R., Davies, L. and Bignell, R. C. 1978, *Astron. Astrophys.*, **63**, 199.

[92] Serlemitsos, P., Ptak, A. and Yaqoob, T., 1996, in *The Physics of LINERs in View of Recent Observations*, ed. M. Eracleous, A. Koratkar, C. Leitherer and L. Ho, Astronomical Society of the Pacific Conference Series vol. 103, p.70.

[93] Smith, D. A. and Done, C. 1996, *MNRAS*, **280**, 355.

[94] Sofue, Y. and Irwin, J. A. 1992, *PASJ*, **44**, 353.

[95] Spitzer, L. 1978, in *Physical Processes in the Interstellar Medium*, Wiley Classics Library Edinton Published.

[96] Stauffer, J. R. 1982, *ApJ*, **262**, 22.

[97] Tacconi, L. J., Blietz, M., Cameron, M., Downes, D., Genzel, R., Krabbe, A., Sternberg, A., Tacconi-Garman, L. E. and Weitzel, L. 1996, *Vistas Astron.*, **40**, 23.

[98] Terashima, Y. 1998, Ph.D. thesis, University of Nagoya.

[99] Taylor, G. B., 1996, *ApJ*, **470**, 394.

[100] Trotter, A. S., Greenhill L. J., Moran, J. M., Reid, M. J., Irwin, J. A. and Lo,K. Y. 1998, *Astrophys.J.*, **495**, 740. (T98)

[101] Turner, B. E., 1973, *ApJ*, **186**, 357.

[102] Turner, T. J. and Pounds, K. A. *MNRAS*, **240**, 833.

[103] Ueno, M. 1995, *Bull. Astron. Soc. India*, **23**, 307.

[104] Veilleux, S., Cecil, G., Bland-Howthorn, J., Tully, R. B., Fillippenko, A. V. and Sargent, W. L. W., 1994, *ApJ*, **433**, 48.

[105] Watson, W. D. and Wallin, B. K. 1994, *ApJ*, **432**, L35.

[106] Whiteoak, J. B. and Gardner, G. F. 1979, *Proc. astr. Soc. Aust.*, **3**, 71.

[107] Wilson, A. S., Braatz, J. A. and Henkel, C. 1995, *ApJ*, **455**, L127.

[108] Wilson, A. S., Roy, A. L., Ulvestad, J. S., Colbert, E. J. M., Weaver, K. A., Braatz, J. A., Henkel, C., Matsuoka, M., Xue, S., Iyomoto, N. and Okada, K. 1998, *ApJ*, **505**, 587.

[109] Young, J. S., Claussen, M. J. and Scovill, N. Z. 1988, *ApJ*, **324**, 115.

[110] Zensus, J. A., Diamond, P. J., Napier, P. J. (eds.) 1995, *Very Long Baseline Interferometry and the VLBA*, Astronomical Society of the Pacific Conference Series vol. 82.